

**BaO_x/ Pt(111) AND BaO_x/ TiO₂/ Pt(111) MODEL CATALYSTS
FOR UNDERSTANDING NO_x STORAGE-REDUCTION (NSR)
CATALYSIS AT THE MOLECULAR LEVEL**

**A THESIS
SUBMITTED TO THE DEPARTMENT OF CHEMISTRY AND
THE GRADUATE SCHOOL OF ENGINEERING AND SCIENCE
OF
BILKENT UNIVERSITY
IN PARTIAL FULFILLMENT OF THE REQUIREMENTS
FOR THE DEGREE
OF
MASTER OF SCIENCE**

by

EMRE EMMEZ

AUGUST 2011

To My Family

And

Didem

I certify that I have read this thesis and in my opinion it is fully adequate, in scope and quality, as a thesis of the degree of Master of Science

Asst. Prof. Emrah ÖZENSOY (Supervisor)

I certify that I have read this thesis and in my opinion it is fully adequate, in scope and quality, as a thesis of the degree of Master of Science

Prof. Dr. Şefik SÜZER

I certify that I have read this thesis and in my opinion it is fully adequate, in scope and quality, as a thesis of the degree of Master of Science

Asst. Prof. Coşkun KOCABAŞ

I certify that I have read this thesis and in my opinion it is fully adequate, in scope and quality, as a thesis of the degree of Master of Science

Asst. Prof. Hande TOFFOLI

I certify that I have read this thesis and in my opinion it is fully adequate, in scope and quality, as a thesis of the degree of Master of Science

Asst. Prof. Daniele TOFFOLI

Approved for the Graduate School of Engineering and Science

Prof. Dr. Levent ONURAL

Director of Graduate School of Engineering and Science

ABSTRACT

BaO_x/ Pt(111) AND BaO_x/ TiO₂/ Pt(111) MODEL CATALYSTS FOR UNDERSTANDING NO_x STORAGE-REDUCTION (NSR) CATALYSIS AT THE MOLECULAR LEVEL

EMRE EMMEZ

M.S. in Chemistry

Supervisor: Assistant Prof. Dr. Emrah ÖZENSOY

August 2011

In this work, formation and decomposition pathways of Ba(NO₃)₂ on BaO-BaO₂/Pt(111) surfaces were investigated at the molecular level for different BaO-BaO₂ coverages starting from small 2D islands of 0.5 MLE (MLE: monolayer equivalent) to thick multilayers of 10 MLE via temperature-programmed desorption (TPD), and X-ray Photoelectron Spectroscopy (XPS) and Low Energy Electron Diffraction (LEED). BaO_x overlayers with a surface coverage of ~ 1 MLE reveal long range ordering with (2×2) and/or (1×2) structures while BaO_x films with a surface coverage of 1.5 MLE yields a BaO(110) termination and thicker films (≥ 5 MLE) were observed to be amorphous. Saturation of thick (10 MLE) BaO_x overlayers with NO₂ leads to the formation of nitrates. Nitrate thermal decomposition was demonstrated to proceed through nitrite intermediates. In TPD experiments two major pathways for nitrate decomposition were observed: 1) nitrate decomposition yielding only NO evolution at ~650 K, and 2) nitrate decomposition with NO + O₂ evolution at ~700 K. This multi-step decomposition behavior was explained by BaO₂ formation during the first stage. The influence of the BaO_x deposition method on the morphology of the BaO_x overlayers were established: when a thick BaO_x layer is prepared using NO₂ for Ba oxidation, BaO_x overlayer efficiently wets the Pt(111)

substrate forming a well-dispersed film. On the other hand, if a thick BaO_x layer is heated in O_2 (to 873 K), BaO_x overlayer agglomerates into 3D clusters, resulting in the formation of exposed (uncovered) Pt sites. BaO_x overlayers with uncovered Pt sites can be “cured” by nitration – thermal decomposition procedures. When the BaO_x layer coverage is below 2.5 MLE, nitrate decomposition temperature is observed at significantly lower temperatures, demonstrating the catalytic influence of the Pt sites facilitating the nitrate decomposition. It is proposed that initially, $\text{Ba}(\text{NO}_3)_2$ decomposes at the boundary/peripheral sites of the Pt/ BaO_x interface, followed by the nitrate decomposition originating from 2D BaO_x islands, and eventually from the 3D BaO_x agglomerates.

Catalytic deactivation of TiO_2 -promoted NO_x -storage reduction (NSR) catalysts due to thermal aging effects was investigated using a $\text{BaO}/\text{TiO}_2/\text{Pt}(111)$ model catalyst system. At room temperature, metallic Ba overlayers on $\text{TiO}_2/\text{Pt}(111)$ was found to be very reactive towards oxide ions on $\text{TiO}_2/\text{Pt}(111)$ resulting in the formation of BaO_x and partial reduction of TiO_2 . Ba films adsorbed on $\text{TiO}_2/\text{Pt}(111)$ that are further oxidized in O_2 at 523 K lead to BaO and BaO_2 surface domains which can efficiently adsorb both NO_2 and CO_2 . Thermal treatment of $\text{BaO}-\text{BaO}_2/\text{TiO}_2/\text{Pt}(111)$ surface at $T \geq 300$ K leads to a monotonic decrease in the surface Ba/Ti atomic ratio indicating the diffusion of BaO- BaO_2 domains into the underlying TiO_2 framework. Solid state reactions between BaO_x and TiO_2 particularly within 473-873K facilitate the formation of $\text{BaTiO}_3/\text{Ba}_2\text{TiO}_4/\text{Ba}_x\text{Ti}_y\text{O}_z$ overlayers. After oxidation at higher temperatures ($T > 873$ K), surface becomes Ba-deficient and the enrichment of the surface with the Ti^{4+} sites results in a TiO_2 -terminated surface. Diffusion of BaO_x into the TiO_2 matrix and the enrichment of the surface with Ti sites drastically suppress the NO_2 and CO_2 adsorption/storage capacity of the model NO_x storage system. These results reveal a direct evidence for the structural changes associated with the thermal deactivation of TiO_2 -promoted NSR catalysts.

Key Words: NSR, model catalyst, BaO thin films, TiO_2 thin films, NO_2 , UHV, $\text{BaO}_x / \text{Pt}(111)$, $\text{BaO}_x / \text{TiO}_2 / \text{Pt}(111)$, XPS, TPD, LEED.

ÖZET

NO_x DEPOLAMA-İNDİRGEME KATALİZ İŞLEMİNİN BaO_x/ Pt(111) ve BaO_x/ TiO₂/ Pt(111) MODEL KATALİZÖRLERİ YARDIMIYLA MÖLEKÜLER DÜZEYDE ANLAŞILMASI

EMRE EMMEZ

Kimya Bölümü Yüksek Lisans Tezi

Tez Yöneticisi: Yard. Doç. Emrah ÖZENSOY

Ağustos 2011

Bu çalışmada, daha önceden kurulumu tamamlanmış olan çok amaçlı yüksek ötesi vakum sistemine, BaO_x/ Pt(111) model NO_x depolama/indirgeme katalizör üretimi amaçlanarak, Pt(111) yüzeyi üzerinde farklı miktarlarda büyütülen BaO_x filmlerinin NO₂(g) türüyle olan etkileşimi *Sıcaklık Programlı Yüzey Salınımı (TPD)* ve *X-Ray Photoelectron Spectroscopy*X-ışını fotoelektron spektroskopisi (XPS) yöntemleriyle incelenmiştir. BaO_x birimlerinin Pt(111) tek-kristal numunesine dozlanmasıyla oluşan düzenli yapılar, *Düşük enerjili electron kırınımı (LEED)* yöntemiyle incelenmiştir. Buna göre Pt tek-kristali üzerinde büyütülen ~1 MLE (MLE: eşdeğer tek katman) yüzey derişimine sahip BaO_x filmlerinde (2x2) ve (1x2) yeniden-yapılanmaları gözlemlenmiştir. Dozlanan BaO_x miktarına bağlı olarak oluşan düzenli yapılar birbirinden farklılık göstermektedir. Örneğin ~1.5 MLE yüzey derişimine sahip BaO_x filmleri, BaO(110) yüzey yapılanması sergilemesine rağmen, 5 MLE'den dahayüksek kalınlığa sahip BaO_x filmlerinde atomic düzeyde düzenli bir yüzey yapısı yerine amorf bir yapı gözlemlenmiştir. Kalın tabaka halinde büyütülen (10 MLE) BaO_x birimlerinin NO₂(g) ile yoğun etkileşimi sonucunda öncelikle nitrat oluşumu gözlemlenmiştir. Yüksek sıcaklıklarda nitratların parçalanmasıyla, nitrit türlerinin oluşumu gözlemlenmiştir.TPD çalışmalarına göre, nitratlar iki adımda

bozunmaktadır 1) ~650 K'de sadece NO yüzey salınımı ile ve 2) ~700 K'de NO + O₂ yüzey salınımı ile. İlk adımdaki NO yüzey salınımı sırasında, BaO₂ oluşumu saptanmıştır. BaO_x filmlerinin farklı hazırlanış yöntemlerine bağlı olarak, yüzey morfolojileri de değişkenlik göstermektedir. Buna göre O₂(g) içerisinde 873 K'de ısıtılan BaO_x/ Pt(111) model katalizörünün oda sıcaklığında NO₂(g) adsorpsiyonu sonucunda yapılan TPD deneyinde, N₂ yüzey salınımına rastlanmıştır. N₂(g) gazının yüzeyden salınımı, BaO birimlerinin Pt yüzeyini yeterince kaplamadığına ve Pt tek kristalinin NO₂(g) gazıyla tepkimeye girip, NO₂(g) gazını, N₂(g) gazına indirgediğine işaret etmektedir. BaO_x filmlerinin NO₂(g) ile etkileşimi sonucu oluşan nitratların kararlılıkları, farklı yüzey kaplama kalınlıklarına bağlı olarak değişiklik göstermektedir. Hazırlanan kalın filmlerde (10 MLE) oluşan nitratlar, ince filmlerde gözlemlenen nitratlara göre (~1 MLE) ısı olarak daha karardır. NO_x-indirgeme depolama malzemelerine TiO₂ ilavesinin, bu malzemelerin ısılaşmalarına olan etkisini incelemek için, BaO/ TiO₂/Pt(111) model katalizör sistemi hazırlanmıştır. Oda sıcaklığında, metalik Ba birimlerinin TiO₂/Pt(111) yüzeyi üzerine dozlanması sonucu, TiO₂ filmlerinin kısmen indirgendiği gözlemlenmiştir. TiO₂/ Pt(111) yüzeyi üzerinde büyütülen Ba birimlerinin O₂(g) içerisinde 523 K'de oksitlenmesi, NO₂(g) ve CO₂(g) türleriyle etkili bir şekilde reaksiyona giren BaO ve BaO₂ türlerinin oluşmasını sağlamıştır. BaO-BaO₂/TiO₂/Pt(111) model katalizörünün 300 K'den daha yüksek bir sıcaklıkta ısıtılması, BaO-BaO₂ oksitlerinin TiO₂ alttaş örgüsünün içine nüfuz etmesine neden olmaktadır. 473K- 873K sıcaklıkları arasında ise, BaO_x birimlerinin TiO₂ ile tepkimeye girmesiyle, BaTiO₃/ Ba₂TiO₄/ Ba_xTi_yO_z perovskit-türü yapıları oluşturdukları gözlemlenmiştir. T>873 K'de, Ba birimlerinin artan yüzey-altı difüzyonu nedeniyle, yüzeydeki TiO₂ oranının zenginleştiği görülmektedir. TiO₂ ile zenginleştirilmiş/örtülmüş BaO_x/TiO₂/Pt(111) model katalizör yüzeyinin, NO₂ ve CO₂ gaz türleriyle olan etkileşim kuvveti ciddi şekilde azalmaktadır.

Anahtar Kelimeler: NSR, model katalizör, BaO ince filmleri, TiO₂ ince filmleri, NO₂, UHV, BaO_x/ Pt(111), BaO_x/ TiO₂/ Pt(111), XPS, TPD, LEED.

ACKNOWLEDGEMENT

I would like to thank to;

... Assistant Prof. Dr. Emrah Özensoy for his outstanding guidance, encouragement and supervision throughout my studies...

... Dr.Evgeny Vovk for his contribution to my scientific background...

...Prof. Mehmet Erbudak from ETH Zurich, for his generous help during the construction of our UHV Surface Analysis Chamber...

... past and present members of Chemistry Department; where I learned a lot and made great friends during the last 7 years...

... the Scientific and Technical Research Council of Turkey (TUBITAK)...

...my parents; Erdener and Temaşa, my sister Merve and my brother Emirhan for their continuous support, prayers and help...

...Finally, I am deeply thankful to Didem, her optimism, energy and unconditional love brought the greatest joy to my life...

TABLE OF CONTENTS

1	INTRODUCTION	1
1.1	Model Catalysts for Heterogeneous Catalysis under UHV (Ultra High Vacuum) Environment	7
1.1.1	Metal Oxide Ultrathin Films on Metal Substrates as Model Catalysts ..	8
1.2	Remediation Studies of NO _x on Model Oxide Surfaces	12
2	EXPERIMENTAL	18
2.1	Ultra-High Vacuum Experimental Set-up.....	18
2.2	UHV Compartments	21
2.2.1	Sputtering Ion Gun (LK Technologies NGI3000 Sputtering Gun).....	21
2.2.2	Precision XY-Z Manipulator Platforms (McAllister MC1500/2000)..	23
2.2.3	Thin Film Doser Compartment	25
2.2.4	Temperature Controller (Heat Wave Labs Model 101303-46A).....	27
2.3	Surface Analytical Techniques.....	28
2.3.1	XPS (X-Ray Photoelectron Spectroscopy)	28
2.3.2	Low Energy Electron Diffraction (LEED) Technique.....	35
2.3.3	Temperature-Programmed Desorption (TPD)	42
2.4	Sample Preparation.....	44
2.4.1	Sputtering of the Sample	44
2.4.2	Preparation of BaO _x Overlayers on Pt (111) and also on TiO ₂ /Pt (111) Surfaces	45
3	RESULTS and DISCUSSION	48
3.1	BaO Films Grown on Pt (111) Substrate.....	48
3.1.1	Structure of BaO Layers on Pt (111).....	48
3.1.2	NO ₂ Adsorption and Storage on Thick (10 MLE) BaO _x Overlayers	53

3.1.3	Effect of the BaO _x Preparation Protocol on the Surface Morphology and Chemistry	58
3.1.4	NO ₂ Adsorption on Thin BaO _x Layers	62
3.2	TiO _x Films Grown on Pt (111)	68
3.3	BaO Films on TiO ₂ /Pt (111) Model System	71
3.3.1	XPS Analysis of BaO/ TiO ₂ / Pt (111) Model Catalysts.....	71
3.3.2	LEED Analysis of the Structural Changes of the BaO _x / TiO ₂ / Pt(111) Model Catalyst.....	75
3.3.3	Chemical Reactivity of BaO _x /Ba _x Ti _y O _z Overlayers to NO ₂ and CO ₂ on TiO ₂ /Pt(111) Model Catalyst.....	77
4	CONCLUSIONS	84
5	APPENDIX	86
5.1	Pumping Units	86
5.1.1	Rotary Pumps	86
5.1.2	Turbo molecular Pump.....	88
5.1.3	Titanium Sublimation Getter Pumps.....	89
5.2	UHV Pressure Gauges	90
5.2.1	Ionization Gauge	90
5.2.3	Thermal Conductivity Gauge (Thermocouple Gauge)	92
5.2.4	Capacitance Manometer.....	92
5.3	XPS Figures.....	94
6	REFERENCES	95

LIST OF TABLES

Table 1. Typical exhaust gas composition of a gasoline powered spark ignition internal combustion engine.[1].....	1
Table 2. European Union emission standards for gasoline and diesel powered (within bracket) passenger cars (g km ⁻¹)[4].....	3
Table 3. Pressure Ranges for Vacuum Technologies.....	19
Table 4. The relationship between quantum numbers, spectroscopists' notation and X-ray notation.[67].....	29
Table 5. X-ray satellite energies and intensities. [69]	34

LIST OF FIGURES

Figure 1. NO _x Storage and Reduction, (a) representation of mechanism and (b) representation of lean and rich cycles [5]	5
Figure 2. Development of supported model catalysts and comparison of the preparation techniques (adapted from ref.[27])	9
Figure 3. Structural parameters and kinetic effects on supported metal catalysts (adapted from ref.[27]).....	10
Figure 4. Thermal desorption spectra of NO on NiO (100) cleaved in vacuum (upper left) and NO on a thin NiO (100) film grown by oxidation of NiO (100) (lower left). Thermal desorption spectra of CO on NiO (100) cleaved in vacuum (upper right) and CO on a thin NiO (100) film grown by oxidation of Ni (100) (lower right) [36].....	11
Figure 5. Molecular orbital diagrams of NO and NO ₂ [37]	12
Figure 6. The visual representations of multi-technique UHV surface analysis chamber.....	21
Figure 7. LK technologies sputtering ion gun with a high-precision leak valve.	22
Figure 8. The MC1500/2000 series XY translator with manual micrometer controllers.....	23
Figure 9. (a) The ZA-series Z-axis translator (b) currently used complete XYZ-θ manipulator including a DC motor used (c) the visual representation of the manipulator probe.	24
Figure 10. Differentially-pumped-rotary-platform (rotary seal) used in manipulator part.....	25
Figure 11. Thin film doser compartment and types/locations of particular dosers...	26
Figure 12. Sample temperature controller unit used in UHV chamber.....	27
Figure 13. Schematic diagram of the XPS process that demonstrates the photoionization of an atom by ejection of a 1s electron. (adapted from ref. [67]). ...	30
Figure 14. Schematic diagram of the cylindrical mirror analyzer (CMA). (adapted from ref. [67]).....	31
Figure 15. Ba3d and Pt4f XPS spectrum were taken during growth of 10 MLE BaO _x phases on Pt(111) substrate.....	33

Figure 16. Bragg's diffraction condition (adapted from ref. [72]).	35
Figure 17. Schematic representation of Low Energy Electron Diffraction Technique.	36
Figure 18. Diffraction patterns of five plane lattices. [73].	38
Figure 19. Experimental set-up for Temperature Programmed Desorption (TPD) technique in ultra-high vacuum. (adapted from ref.[68]).	42
Figure 20. Sample preparation method P1 for the BaO _x films grown on Pt (111) substrate (Protocol 1).	45
Figure 21. Sample preparation method P2 for the BaO _x films grown on Pt (111) substrate (Protocol 2).	46
Figure 22. Sample preparation method for the BaO _x films grown on TiO ₂ /Pt (111) model system.	47
Figure 23. LEED pictures obtained during various stages of the ordered BaO _x overlayer formation on Pt(111) (see text for details). Electron beam voltage for the LEED patterns given in (a-f) is 70-85 eV, respectively. XPS spectrum corresponds to the LEED pattern given in Figure 23b.	48
Figure 24. Schematic representations of the LEED patterns given in Figure 23. Large (black) diffraction spots correspond to the Pt(111) substrate while small (red and black) diffraction spots originate from the overlayer (a) (2x2)R30° superstructure (b) (1x2)R30° superstructure (c) (2x2) superstructure (d) (1x2) superstructure. Tentative real space representations of the (e) (2x2) and (f) (1x2) superstructures...	50
Figure 25. (a) LEED patterns for a BaO _x (1.5 MLE)/Pt(111) surface and (b) the schematic representation of the corresponding diffraction spots. Big black spots correspond to the Pt(111) substrate while the small black spots correspond to three different rotated domains with real-space unitcell dimensions of 3.9×5.5 Å	52
Figure 26. XPS core level spectra, N1s and O1s for a thick BaO _x (10 MLE) /Pt(111) exposed to 3600 L NO ₂ at 323 K and subsequently annealed to the indicated temperatures in vacuum.	54
Figure 27. TPD spectra for NO (m/z= 30), O ₂ (m/z=32), and N ₂ /CO (m/z=28) channels obtained after exposure of BaO _x (10 MLE)/ Pt(111) surface to 900 L NO ₂ at 323 K.	57
Figure 28. (a) TPD spectra for the NO (m/z=30), O ₂ (m/z=32), and N ₂ / CO (m/z= 28) desorption channels obtained after the exposure of a BaO _x (10 MLE)/ Pt(111)	

surface to 900 L NO ₂ at 323 K; where the BaO _x film was prepared using protocol 2	
(b) A similar TPD experiment performed on a BaO _x (10 MLE)/ Pt(111) surface which was initially exposed to subsequent multiple cycles of NO ₂ adsorption/saturation and annealing at 1073 K.	60
Figure 29. O1s XPS core level spectra for BaO _x (~2.5 MLE) /Pt(111) surface exposed to 360 L NO ₂ at 323 K and subsequent annealing to the indicated temperatures.	63
Figure 30. The graphs of O1s peaks intensity ratios O _{perox} (530.8 eV) to O _{ox} (528.6 eV) for 10 ML (grey squares) and 2.5 ML (black circles) BaO _x films measured after nitration and subsequent heating.	64
Figure 31. TPD spectra for NO (30 amu), O ₂ (32 amu), and N ₂ /CO (28 amu) obtained after exposure of BaO _x (~2.5 MLE) /Pt(111) to 900 L NO ₂ at 323 K.	65
Figure 32. TPD spectra for NO (30 amu), O ₂ (32 amu), obtained after exposure of BaO _x (~2.5 MLE) /Pt(111) to 900 L NO ₂ (P _{NO₂} = 5x10 ⁻⁷ Torr x 30 min) at 323 K then preheated to 623 K before TPD.	66
Figure 33. TPD spectra for NO (30 amu) desorption obtained after exposure of BaO _x / Pt(111) surfaces with varying BaO _x coverages (0.5 MLE < θ _{BaO_x} <10 MLE) to 900 L NO ₂ (P _{NO₂} = 5x10 ⁻⁷ Torr x 30 min) at 323 K.	67
Figure 34. XPS spectra of TiO _x phases depending on the oxidation conditions in the Ti2p and O1s core level region (see text for details).	69
Figure 35. LEED patterns for ordered TiO _x / Pt(111) surfaces with varying θ _{TiO_x} (see text for details)	70
Figure 36. XPS data corresponding to the (a) Ti 2p, (b) O 1s and (c) Ba 3d _{5/2} regions obtained for (i) TiO _x (1.4 MLE)/ Pt(111), (ii) TiO ₂ (26MLE)/ Pt(111), (iii) as deposited Ba(3 MLE)/ TiO ₂ (26 MLE)/ Pt(111) surface prior to oxidation, (iv) BaO _x (6 MLE)/ TiO ₂ (26 MLE)/ Pt(111) surface obtained after oxidizing sample (iii) in O ₂ (P _{O₂} = 5x10 ⁻⁷ Torr) at 523 K followed by a second Ba deposition at RT and oxidation at 523 K, (v) a surface prepared by the oxidation of sample (iv) in O ₂ (P _{O₂} = 5x10 ⁻⁷ Torr) at 973 K. (for Pt4f region see Appendix).....	72
Figure 37. Ba/Ti surface atomic ratio values obtained from the XPS data for a BaO _x (0.7 MLE)/TiO ₂ (26 MLE)/Pt(111) surface after oxidation and thermal aging steps at various temperatures (see text for details).....	74

Figure 38. (a) LEED image corresponding to the (2x2) reconstruction of TiO₂ (26 MLE) overlayers on Pt(111), (b) BaO_x(0.7 MLE)/TiO₂(26 MLE)/Pt(111), (c) a surface obtained by the oxidation of the sample given in (b) in O₂ (P_{O₂}= 5x10⁻⁷ Torr) at 1073 K. Electron energy values used for the acquisition of the LEED patterns in (a-c) were 85 eV, 85 eV and 105 eV, respectively. 76

Figure 39. TPD spectra for NO (m/z= 30), N₂/CO (m/z= 28) and N₂O/CO₂ (m/z= 44) desorption channels obtained (a) after exposure of BaO(<1 MLE)/TiO₂ (26MLE)/ Pt(111) to 180 L NO₂ at RT (b) exposure of BaO(1 MLE< x <2 MLE)/TiO₂ (26 MLE)/ Pt(111) to 180 L NO₂ at RT (c) exposure of BaO(>2 MLE)/TiO₂ (26 MLE)/Pt(111) to 180 L NO₂ at RT 78

Figure 40. (a) m/z=30 desorption channels in the TPD profiles for NO₂ adsorption (P_{NO₂}=1x10⁻⁷, 30 min at RT) on: fresh BaO_x(6 MLE)/ TiO₂(26 MLE)/ Pt(111) surface (spectrum *i*), BaO_x(6 MLE)/ TiO₂(26 MLE)/ Pt(111) surface pretreated at 973 K (spectrum *ii*), fresh TiO₂(26 MLE)/ Pt(111) surface (spectrum *iii*). (b) m/z=44 desorption channels for the same TPD experiments given in part (a). (c) m/z=44 desorption channels in the TPD profiles for CO₂ adsorption (P_{CO₂}=5x10⁻⁷ for 5 min at RT) on: fresh BaO_x(6 MLE)/ TiO₂(26 MLE)/ Pt(111) surface (spectrum *i*), BaO_x(6 MLE)/ TiO₂(26 MLE)/ Pt(111) surface pretreated at 973 K (spectrum *ii*). 80

Figure 41. Schematic representation elucidating the surface segregation and sub-surface diffusion in BaO_x/ TiO₂/ Pt(111) model catalyst systems. 83

Figure 42.Sectional view of the Pfeiffer DUO-35, 35 m³/h double stage, rotary vane pump: (1) intake (2) filter (3) rotor (4) spring (5) vane (6) gas ballast valve (7) filter (8) discharge valve (9) exhaust (10) sealing surface.[63] 86

Figure 43.Schematic representation of the cross section of a dual-stage RVP (left)[63] RVP units in the UHV set-up (right). 87

Figure 44.Varian TV 551 Navigator-Model 9698923 TMP. 88

Figure 45.Titanium sublimation pump unit..... 89

Figure 46. (a) Ionization gauge mechanism (adapted from ref. [49]) (b) Schematic representation of an Bayard-Alpert type ionization gauge (adapted from ref. [63]) (c) Ionization gauge utilized in the UHV set-up..... 91

Figure 47.Thermocouple gauges in the UHV experimental set-up..... 92

Figure 48.(a) Basic diagram of capacitance diaphragm gauges (adapted from ref. [63]) (b) Baratron capacitance manometer in the UHV chamber. 93

Figure 49. XPS core level spectra, Ba3d and Pt4f for a thick BaO_x(10 MLE) /Pt(111) exposed to 3600 L NO₂ at 323 K and subsequently annealed to the indicated temperatures in vacuum. 94

Figure 50. XPS core level spectra corresponding to Pt4f during the growth of TiO₂ (26 MLE) overlayers on Pt(111) substrate..... 94

1 INTRODUCTION

The industrial development in the world leads to an increase in the consumption of fossil fuels such as natural gas, coal and oil. The partial combustion of these compounds results in the emission of nitrogen oxides (NO_x), carbon monoxide (CO), sulfur oxides (SO_x), NH_3 and also unburned hydrocarbons (HC) to the atmosphere and cause environmental pollution. These gaseous species also undergo transformations in the atmosphere by oxidation reactions of ozone and also hydroxyl free radicals. Exhaust gas from the combustion of fossil fuels such as petroleum or diesel also contains many pollutants such as NO_x , CO, unburned hydrocarbon and trace amounts of H_2 , N_2O , NH_3 , CO_2 and SO_x . However, amount of NO_x produced from diesel engine is less than the gasoline engine since it has a cooler combustion environment.[1]For a gasoline powered spark ignition internal combustion engine, a typical exhaust gas composition is presented in Table 1.

Table 1. Typical exhaust gas composition of a gasoline powered spark ignition internal combustion engine.[1]

Gases	Vol. (%)
N_2	71.0
CO_2	18.0
H_2O	9.2
O_2 and noble gases	0.7
Pollutants	
(a) CO	0.85
(b) NO_x	0.08
(c) Unburned HCs	0.05
(d) Particulate matters	0.005
Others	0.115
Total	100

Exhaust gas pollutant concentration is closely related to the air to fuel (A/F) ratios:

$$A/F = \text{mass of air consumed by the engine} / \text{mass of fuel consumed by the engine}$$

The exhaust gas composition is also defined in terms of λ :

$$\lambda = \text{actual engine A/F} / \text{stoichiometric engine A/F}$$

For gasoline engines, there is a stoichiometric value for A/F that equals to 14.7.[2] This is the point where the amount of oxidants is equal to that of reducing agents. Fuel-rich condition occurs if the A/F ratio is below this value and in this case, exhaust gas is rich with reducing agents like CO and HC. On the other hand, if A/F ratio is above this value, then it is called the fuel-lean condition and this time the exhaust gas consists of more oxidizing agents like NO and O₂.

Hazardous gases emitted from exhausts have devastating effects on earth's atmosphere, environment and human health. For instance, NO_x is the principal pollutant for the formation of ground level ozone which is a health hazard and harmful to plants, ozone layer depletion and also acid rains.

It is found that ground level ozone is produced through the photochemical decomposition of NO₂ with the following mechanism:[3]

First, the peroxy radicals begin to form with the reaction of CO or hydrocarbons with the hydroxyl radical present in the troposphere:



Peroxy radicals then react with NO to give NO₂ and NO₂ undergoes a further photochemical reaction yielding atomic oxygen which reacts with O₂ to give ozone, O₃:



NO_x also catalyzes ozone layer depletion in the stratospheric region via reactions given below:[3]



Finally, NO_x form nitric acid when dissolved in moisture of atmosphere:[3]



Due to the ecological and health hazards of the NO_x and several other emission gases, regulations have been proposed and enforced to limit NO_x emissions. The type and the level of regulations vary among countries. For instance, European Union emission standards are categorized as Euro 1, Euro 2, Euro 3, Euro 4 and Euro 5 fuels for light vehicles. Descriptions of European Union emission standards are given Table 2.

Table 2. European Union emission standards for gasoline and diesel powered (within bracket) passenger cars (g km⁻¹)[4]

Tier	Timeframe	CO	THC	NMHC	NO _x	HC + NO _x	PM
Euro 1	July 1992	2.72 (2.72)	– (–)	– (–)	– (–)	0.97 (0.97)	– (0.14)
Euro 2	January 1996	2.2 (1.0)	– (–)	– (–)	– (–)	0.5 (0.7)	– (0.08)
Euro 3	January 2000	2.3 (0.64)	0.20 (–)	– (–)	0.15 (0.50)	– (0.56)	– (0.05)
Euro 4	January 2005	1.0 (0.50)	0.10 (–)	– (–)	0.08 (0.25)	– (0.30)	– (0.025)
Euro 5	September 2009	1.000 (0.500)	0.100 (–)	0.068 (–)	0.060 (0.180)	– (0.230)	0.005 (0.005)
Euro 6	September 2014	1.000 (0.500)	0.100 (–)	0.068 (–)	0.060 (0.080)	– (0.170)	0.005 (0.005)

The criteria for the compulsive emission limits enforce automotive manufacturers and catalysis researchers to develop more efficient engines and more effective deNO_x strategies. The traditional three-way catalysts (TWC) are ineffective for NO_x treatment under lean operating conditions since TWC technology has been designed for the stoichiometric regime (i.e. λ=1).[2] Removal of NO_x from lean-burn exhaust can be performed in three ways: (i) direct thermal decomposition of NO; (ii) selective catalytic reduction (SCR); and (iii) NO_x storage and reduction (NSR) catalysis. In the first approach, NO can be decomposed directly without any reducing

agent. ($2\text{NO} \rightarrow \text{N}_2 + \text{O}_2$) This is also a thermodynamically favorable process ($\Delta H_{298}^\circ = -86.6 \text{ kJ/mol}$). [5] However, very high activation energy is required for the reaction to proceed. In the second approach, NO can be selectively reduced with various reducing agents such as H_2 , hydrocarbons (HC) and NH_3 /urea in a rich-oxygen environment. In the case of ammonia SCR, the stoichiometry of the simplified overall reaction is: [6]



An alternative way for the abatement of NO_x species is the NO_x storage-reduction catalysts. NSR catalyst can work under both fuel lean and fuel rich environments. This concept was first introduced by Toyota motor company in the mid-1990s. [7] Under lean conditions of engines (i.e. under excess oxygen) NO_x is adsorbed on the catalyst, while under rich conditions NO_x reduction takes place. Therefore, in an NSR catalyst, there must be sites for both NO_x sorption (alkali metal or alkaline earth metal compounds) and sites for NO_x oxidation/reduction (noble metals). [8] One of the most commonly used NSR catalyst formulation is Pt-Ba/ Al_2O_3 . [9]

There are five steps for the NSR mechanism as shown in Figure 1:

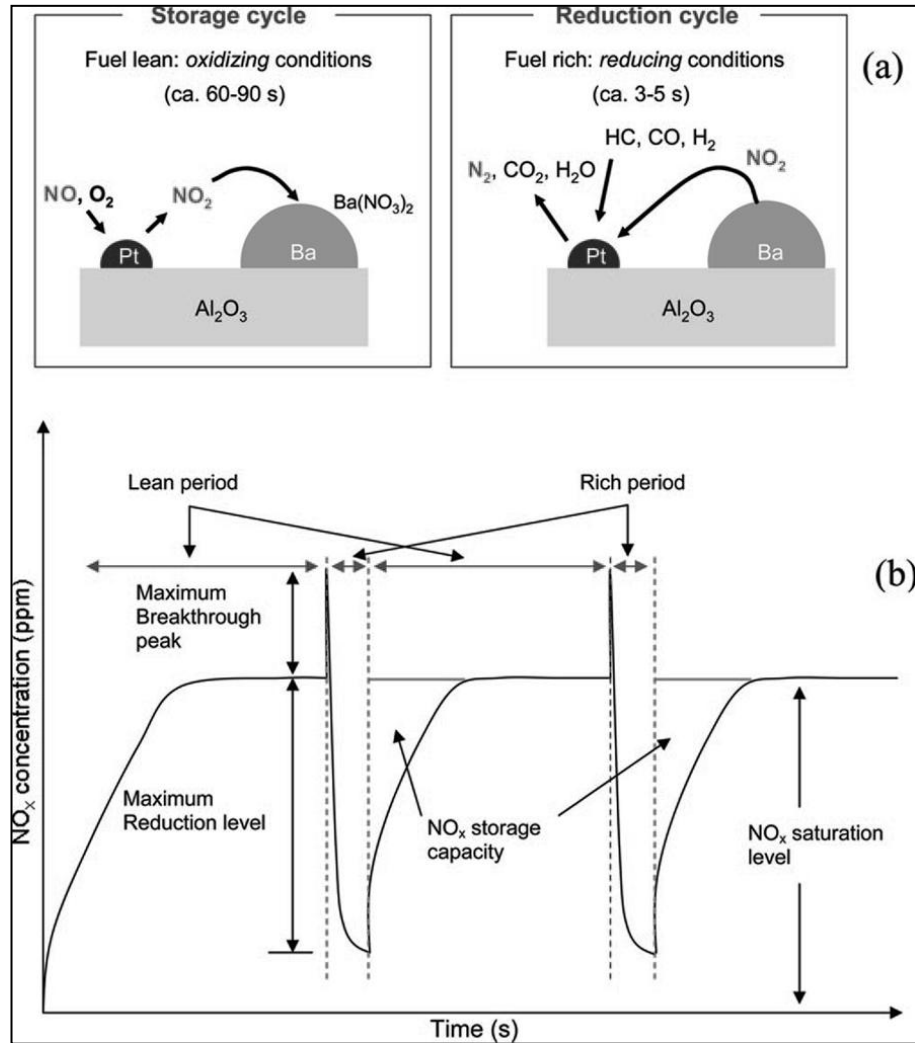


Figure 1. NO_x Storage and Reduction, (a) representation of mechanism and (b) representation of lean and rich cycles [5]

- 1- Oxidation of NO to NO₂ ($\lambda > 1$, fuel lean)
- 2- NO_x adsorption on the basic adsorption sites ($\lambda > 1$, fuel lean)
- 3- Release of reducing agents (such as hydrocarbons, CO, or H₂) ($\lambda < 1$, fuel rich)
- 4- NO_x release from the surface ($\lambda < 1$, fuel rich)
- 5- Reduction of NO_x to N₂ ($\lambda < 1$, fuel rich)

It is found that NO₂ adsorbs more effectively than NO to the NSR trapping material.[10] Therefore, the formation of NO₂ is a crucial step for the adsorption, and the oxidation of NO to NO₂ takes place over precious metals. There are two different suggestions about the mechanism of oxidation; first, the Langmuir-Hinshelwood

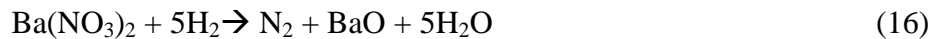
model is suggested for the NO oxidation over Pt-BaO/Al₂O₃, [11] second, the Eley-Rideal type of mechanism is involved for the NO oxidation over Pt. [12]

In literature, there is an ongoing debate associated with the NO_x storage mechanism. In various recent studies, [9,13] it was suggested that NO_x storage is accomplished via different routes (i) the “nitrate route” which involves NO oxidation to NO₂ on Pt sites and NO₂ spillover to BaO domains yielding the formation of Ba(NO₃)₂ and NO(g); (ii) the “nitrite route”, where NO is first oxidized to nitrite species in the presence of oxygen, followed by oxidation of nitrite to nitrates; (iii) in an alternatively proposed storage mechanism, [14] it is suggested that, NO₂ is first loosely adsorbed on BaO, then these adsorbed species decompose into BaO₂ and NO, and finally BaO₂ reacts with NO₂(g) to give Ba(NO₃)₂ as given below;



However, there exists sound evidence in the literature that different barium sites can exist, which differ in reactivity. [15,16] The interface between Ba sites and Pt sites are considered to be more reactive than barium sites located further away from Pt. [17] Depending on the reaction conditions, BaO, Ba(OH)₂, or Ba(CO)₃ can be formed on the surface. It is also worth mentioning that NO_x storage occurs on BaO more efficiently than Ba(OH)₂ and Ba(CO)₃. [18]

Under rich conditions, stored NO_x is reduced by the reductants such as CO, H₂ in the following manner. [5, 9]



An additional mechanistic aspect of NSR systems is the SO_x poisoning. Sulfur oxides (SO_x) present in exhaust gas can react with the catalyst in a similar way to the NO_x species. [19] Sulfur poisoning can deteriorate catalytic functionality of both the support material as well as the storage domains. SO₂ can form aluminum sulfate on alumina while on BaO, it may form BaSO₄. [7] Since the stability of

sulfates are much higher than that of nitrates, once sulfates are formed on the catalyst surface, the activity of the catalyst towards NO_x species significantly decreases.

1.1 Model Catalysts for Heterogeneous Catalysis under UHV (Ultra High Vacuum) Environment

In order to promote new catalysts with enhanced performance, it is important to be able to control fundamental surface properties of catalytic materials such as particle size, morphology, chemical composition, dispersion at the atomic level.[20, 21]

From a microscopic point of view, the relation between real world catalysis kinetics and the elementary reaction mechanisms is generally ambiguous. Thus, fundamental catalyst studies focus on the well-defined micro kinetic model, in which the reaction mechanisms are properly elucidated[21] in an attempt to relate microscopic properties such as atomic composition, electronic and geometric structure to macroscopic properties such as catalytic activity and selectivity.[22] Real world catalysts are complex materials; most of them are comprised of mixtures of oxides or sophisticated metal/oxide systems. On the other hand the well-defined surface science model catalysts are much more simplistic in terms of their structures creating a so called “*materials gap*” between surface science and industrial catalysis. [23] In addition, technical catalysts are typically operated at elevated pressures (>760 Torr) which is far from the UHV conditions used in surface science studies. This is known as the “*pressure gap*” between applied catalysis and surface science.[22]

The main advantage of model catalyst systems is that complex morphological and chemical features of a catalyst surface can be introduced in a well-controlled manner using a surface science approach. In addition, utilization of metallic single crystal support materials provide electrical and thermal conductivity which enables the effective use of electron-based spectroscopic (XPS, Auger electron Spectroscopy-AES, Ultraviolet photoemission spectroscopy-UPS, High Resolution electron energy loss spectroscopy-HREELS), diffraction (LEED) and imaging (Scanning Tunneling Spectroscopy-STM) techniques.[24] In these model

catalyst studies, a proper selection of metal/oxide interface and the film thickness can be utilized as a design parameter to create novel catalytic materials.[25]

1.1.1 Metal Oxide Ultrathin Films on Metal Substrates as Model Catalysts

Model catalysts were originally introduced in the late 1960s with the development of UHV technology. Over the years, the complexity for the investigated experimental systems has continuously increased. Studies on metal single crystal surfaces were the initial starting point providing important reference data for the reactivity of ideal/atomically ordered surfaces and reaction mechanisms.[26] Furthermore, studies on stepped or defect-rich metallic single crystals provided important fundamental knowledge about the catalytic active sites. However, these initially studied simple surfaces did not often show catalytic properties that are compatible with realistic catalysts. For this reason, more recent studies in surface science focused on more complex model catalysts including oxide surfaces. Here, the surface defect properties of the oxide surface turned out to be particularly important due to their direct influence on the reactivity and the growth morphology of the metal deposits (i.e. active sites).[27] Today, a large number of ordered oxide thin films such as Al_2O_3 , SiO_2 , MgO , NiO , Cr_2O_3 , FeO , or Fe_3O_4 can be readily prepared via a large number of precursors.[28] The metal-oxide film growth can be performed by (a) the direct oxidation of a mono-metallic single crystal, (b) the oxidation of a single crystal alloy, (c) the deposition and oxidation of a metal on an inert single crystal substrate.[27] After growth of the metal-oxide thin film as the catalytic support material, model catalyst can be modified by deposition of active particles in the form of metal or oxide aggregates in the nanometer size range. Figure 2 represents the general features of the typical model catalysts described above and compares the preparation techniques.

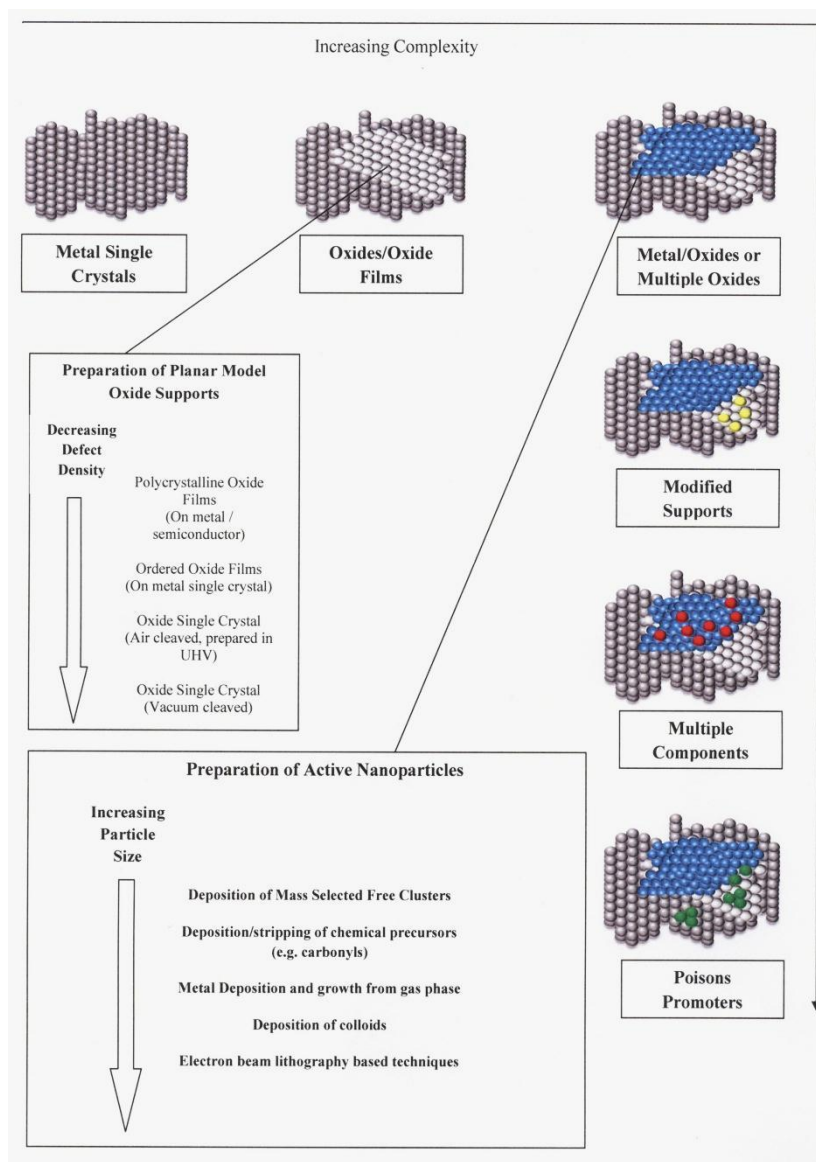


Figure 2.Development of supported model catalysts and comparison of the preparation techniques(adapted from ref.[27])

The earlier work in the literature revealed that the function of the support is not only limited to the dispersion of the catalytically active sites, but also includes a direct modification of the electronic and structural properties of the active sites.[28] Therefore, the catalytic activity of the model catalyst surfaces is mostly determined by the specific interplay between the exposed sites. There are several concepts which can relate the surface structural aspects to the catalytic reactivity.[25]

- (i) **Support Effects:**Surface diffusion(such as spillover or reverse-spillover phenomena) and the adsorption strength of adsorbates on the support material has a strong influence on the catalytic elementary steps.[28,29]
- (ii) **Size and Electronic Effects:**The electronic structure of a supported metal or metal oxide nanoparticle particle can be different from its planar (single crystal) counterpart. For instance, “size effects” can lead to “electron confinement”. Furthermore, reduced dimensions can cause lattice distortions which can change the electronic environment of the support. [21]It is clear that these kinds of effects are strong mostly for relatively small particles (<5 nm).[30]
- (iii) **Geometric Effects:**A metal particle can exhibit different specific sites, such as particle edges or corners and these specific sites result in different catalytic activities with respect to a given reaction.[21]

Some of these structural parameters related with the kinetic effects are summarized in Figure 3.

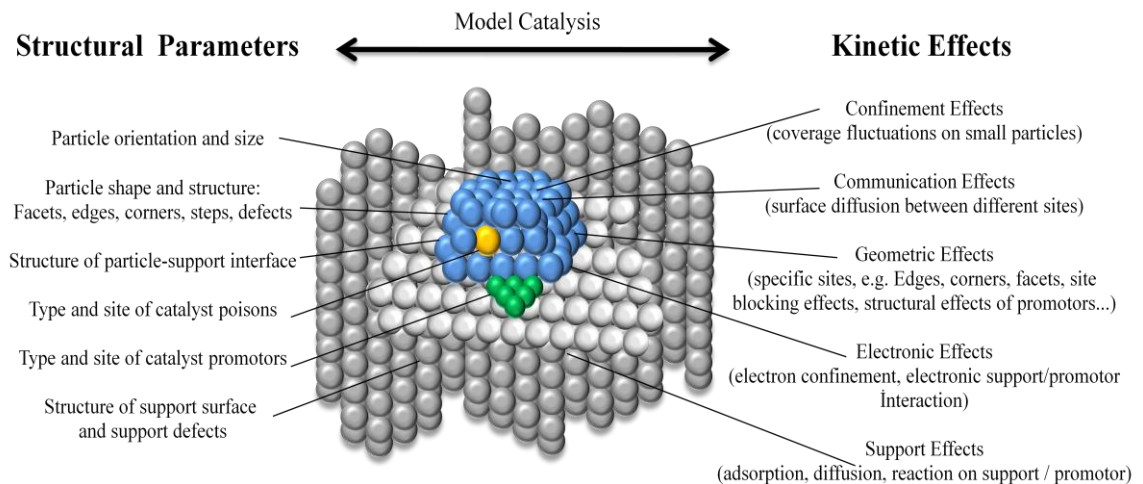


Figure 3.Structural parameters and kinetic effects on supported metal catalysts(adapted from ref.[27])

The properties of thick films of 5-10 layers are close to bulk materials, however, the properties of ultrathin films with a thickness of 1-5 layers on metallic

supports are not always representative of bulk materials, and can expose properties different from the bulk.[31] MgO well-ordered oxide films on Mo (100) [34] and also NiO on Ni (100) [35] were grown in order to study oxide film properties with respect to molecular adsorption. In these two specific examples, there is an important misfit between the oxide overlayer and the support, since, mostly defect sites, such as steps and corners interact with adsorbates from the gas phase. If those defect sites were blocked by water adsorption, the properties of the thin film resemble the bulk material.[31] As can be seen from Figure 4, which shows the CO and NO thermal desorption spectra from Ni (100) film and bulk material, the correlation between the data indicates that these thin films may be used to model the surface of the bulk material.[36]

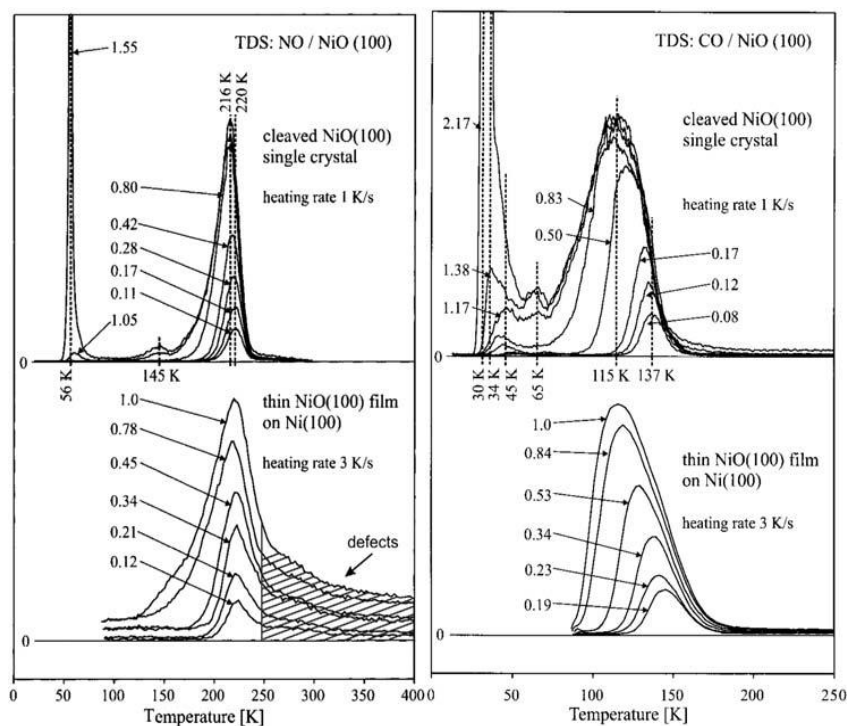


Figure 4. Thermal desorption spectra of NO on NiO (100) cleaved in vacuum (upper left) and NO on a thin NiO (100) film grown by oxidation of NiO (100) (lower left). Thermal desorption spectra of CO on NiO (100) cleaved in vacuum (upper right) and CO on a thin NiO (100) film grown by oxidation of Ni (100) (lower right) [36]

1.2 Remediation Studies of NO_x on Model Oxide Surfaces

The electronic and coordination properties of NO_x (x=1, 2) are known and well-understood. Figure 5 represents the molecular orbital diagrams of NO and NO₂. [37]

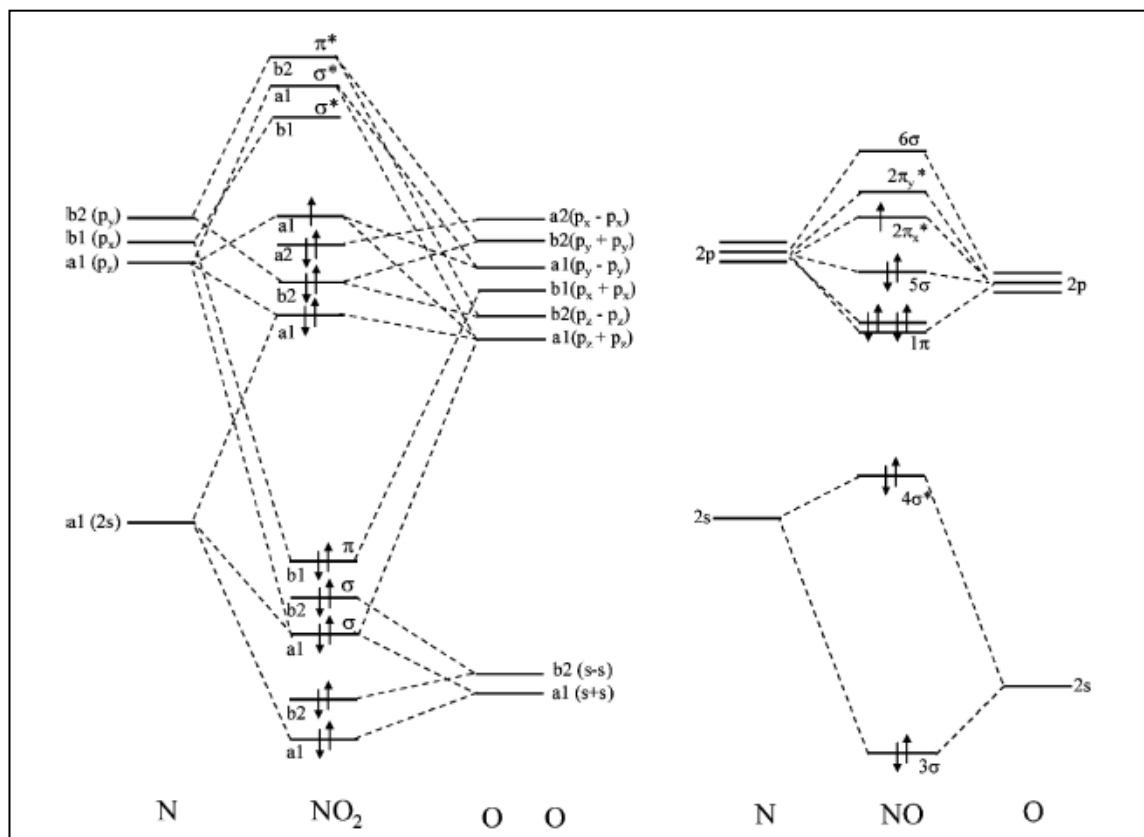


Figure 5. Molecular orbital diagrams of NO and NO₂ [37]

The bond order in NO is 2.5. It decomposes into its elements only at elevated temperatures in the absence of a catalyst (1100-1200 °C with an activation energy of 335 kJ/mol). NO has an electron in the 2π* orbital and this antibonding electron lowers the dissociation energy of gas phase NO relative to N₂. In the case of NO₂, the unpaired electron is more localized on the N atom. The main purpose is to design a catalyst that will decompose NO_x into N₂ and O₂ efficiently without causing the production of other nitrogen oxides such as N₂O. [37] Therefore, surface science studies are focused on the clarification of the mechanism of NO_x decomposition on

single-crystals, metal oxide single-crystal surfaces and oxide supported metal particles. In the literature, the mechanism of N-O bond breaking on model catalysts has been comprehensively reviewed by Garin.[38]

According to Garin's review, surface defects with uncoordinated and reactive surface atoms promote the dissociation of the N-O bond on oxide-supported catalysts. During the catalytic reactions of NO decomposition, surface reconstruction phenomena are commonly observed. In addition, adsorption of NO_x on metal oxide surfaces results in several intermediates such as NO₂⁻ and NO₃⁻ which in turn, can also alter the oxidation state of metallic sites on the surface.[38]

The mechanism of NO₂ storage in magnesium oxide supported barium oxide (BaO/MgO) has also been investigated by using in-situ Raman spectroscopy and X-ray diffraction in the absence and presence of molecular oxygen.[39] According to these results, up to $T < 400$ °C, the NO₂ storage behavior in BaO/MgO occurs through the formation of barium-nitro species which turn into nitrite ions concomitant to the formation of nitrates. At 400 °C, the formation of nitrates is mostly accomplished by BaO₂ species. Improvement in the rate of nitrate formation was observed at low BaO loadings with the presence of oxygen. Stored NO₂ can be reduced by CO and this leads to the formation of CO₂ which limits the NO₂ storage capacity due to the formation of BaCO₃. However, it is also reported that these carbonate species can be replaced by nitrates in the presence of NO₂ at 400 °C.

In recent studies, Bowker et al investigated BaO thin films by using Pt (111) as a substrate in order to investigate the NO_x storage phenomenon. Their STM images showed that at relatively low coverages of BaO on the surface, BaO layers are reconstructed in a (2x2) fashion.[40,41] They have also demonstrated that these BaO particles irreversibly transform into BaO, whereas the BaO thin film partially converts into metastable BaO₂ which is lost when the oxygen is removed.[40] BaO particles do not react with NO at 573 K, however, dosing a mixture of NO and O₂ allows the NO_x to be stored in the form of nitrate. Moreover, Bowker et al. also investigated BaO films on a Cu (111) substrate in terms of structure and reactivity. According to their findings, BaO films grown on Cu (111) exhibit a (100) surface orientation and these films can not be readily converted into BaO₂ under UHV conditions.[42] There was no evidence for a reaction between NO and BaO at low NO pressures of within 300 K-573 K, however, NO₂ reacted readily with pure BaO

at ambient pressures to form nitrite, $\text{Ba}(\text{NO}_2)_2$, then, the slow formation of nitrate was observed.

Schmitz and Baird et al. studied NO and NO_2 adsorption on BaO in which aluminum oxide surface is used as a substrate. The presented data showed that NO adsorbs predominantly as a nitrite and NO_2 adsorbs predominantly as a nitrate on barium oxide during high exposures at room temperature. They proposed that high coverage nitrate forms through the combination of two surface nitrites and a molecularly adsorbed NO_2 to form a trimer, in which all nitrogen centers become nitrate-like.[43] They have also reported the occurrence of peroxide-like adspecies. They offered an alternative mechanism to the conventional adsorption/reaction of NO_2 on BaO. According to this mechanism, the molecular adsorption of NO to form nitrite-like adspecies dominate the initial trapping mechanism. As NO_2 is formed over the noble metal sites, it can either spill over onto the oxide or dissociatively adsorb to form more nitrites. Furthermore, if the surface coverage of nitrite is high enough, it can also form nitrate-like species.

Libuda et al. prepared BaO nanoparticles by Ba deposition and subsequent oxidation on an $\text{Al}_2\text{O}_3/\text{NiAl}$ (110) support surface and investigated its interaction with as a function of BaO particle size.[44,45] They have found that immediate intermixing of Ba^{2+} and Al^{3+} ions along with the formation of a mixed oxide $\text{BaAl}_{2x}\text{O}_{1+3x}$ occurs for large film thickness. Moreover, annealing in oxygen enhances the mixed oxide formation and further growth of the oxide film. Introduction of NO_2 on the mixed oxide $\text{BaAl}_{2x}\text{O}_{1+3x}$ particles on $\text{Al}_2\text{O}_3/\text{NiAl}$ (110), yields nitrite formation, and nitrite formation completely saturates at an NO_2 exposure of c.a. 1000 L (1L: Langmuir = 1×10^{-6} Torr/sec). Beyond this exposure, surface nitrates are generated by the transformation of nitrites into nitrates. By the help of vibrational spectroscopy, they concluded that the surface nitrites and nitrates are primarily coordinated to Ba sites.[45]

Szanyi et al. studied extensively the Ba deposition on a $\theta\text{-Al}_2\text{O}_3/\text{NiAl}$ (100) substrate under ultrahigh vacuum conditions and studied the surface species during NO_2 exposures to BaO/ $\text{Al}_2\text{O}_3/\text{NiAl}$ (100) at different temperatures.[46-50] They have reported that the preparation of an oxidized Ba deposit by oxidation in O_2 at 800 K results in the growth of 2 D and 3 D Ba-containing surface domains, rather than a layer-by-layer growth mode.[46] However, in their previous results, [47] Ba

deposition on θ -Al₂O₃/ NiAl (100) substrate at 300 K in UHV promoted the layer-by-layer growth of Ba for the first two layers. Therefore, they concluded that the growth morphology and the oxidation state of the Ba species on the θ -Al₂O₃/ NiAl (100) substrate can be fine-tuned by controlling the preparation conditions such as surface temperature and oxidative environment. NO₂ adsorption mechanism on a clean, thick BaO film supported on Al₂O₃/ NiAl (110) substrate was also examined.[48] Accordingly, exposure of BaO to NO₂ at 90 K resulted in the formation of nitrite-nitrate pairs. During the heating of the nitrite-nitrate pair covered BaO, nitrites decompose first and leaves one oxygen atom behind which takes a role in the formation of BaO₂. The formed BaO₂ is present even after all the nitrates are decomposed. The effect of BaO film thickness on the NO_x uptake properties was also studied, and it was found that the interaction of NO₂ with model systems at low BaO coverages is significantly different from that of a thick BaO film.[49] For instance, nitrite species form at low exposures of NO₂, and then nitrates form at high NO₂ exposures ($>1 \times 10^{-5}$ Torr). However, for a bulklike, thick (>30 ML) BaO film, NO₂ adsorption results in the initial formation of nitrite-nitrate ion pairs at low NO₂ exposures. The effect of temperature on the nature of NO_x species formed was also identified by the reaction of NO₂ with a pure BaO film.[50] The results suggested that NO₂ adsorption on the clean, thick BaO film at 300 K sample temperature leads to the formation of nitrite-nitrate ion pairs as in the case of 90 K adsorption of NO₂.

TiO₂ is commonly utilized as a support material in many catalytic process or as an active catalyst in photocatalytic systems. In the NSR catalysts concept, TiO₂ has a noticeable ability to suppress the sulfur deposition.[51] Although, numerous efforts have been done for the sol-gel application of TiO₂ in the powdered samples, there is little known about the chemistry of TiO₂ towards NO_x species in surface science applications. Rodriguez et al. investigated the NO₂ interaction with TiO₂ (110) rutile surface both experimentally and theoretically.[52] According to these results, the main product of the adsorption of NO₂ on TiO₂(110) is surface nitrate with a small amount of chemisorbed NO₂. Photoemission data and density functional theory (DFT) calculations indicated that the surface nitrate forms through the disproportionation of NO₂ on Ti sites rather than direct adsorption of NO₂ on O centers of titania. Moreover, the adsorbed NO₂ affects the thermochemical stability of O vacancies, promoting their migration from bulk to the surface of titania.

Peden et al. examined the interaction of N_2O with TiO_2 (110) in order to understand better the conversion of NO_x species to N_2 over TiO_2 -based catalysts. [53] It was shown that the reactivity of N_2O with TiO_2 (110) is directed by the reactions at oxygen vacancy sites. At these vacancies, N_2O decomposes through two paths, one that oxidizes vacancies and another that deposits oxygen atoms on the surface. However, both paths resulted in N_2 desorption. It was also proposed that the conversion of N_2O to N_2 over clean TiO_2 (110) requires both the presence of oxygen vacancy sites and a sufficiently long residence time of N_2O at these vacancies.

Granozzi and Sedona et al. prepared ultrathin ordered titanium oxide films on Pt (111) substrate to investigate the effect of coverage, annealing temperature and oxygen pressure on the structure of TiO_x overlayers. [54] The optimum experimental conditions which determine the formation of ordered ultrathin, and ordered titanium oxide films in the range of one monolayer has been determined. Moreover, transformations between the different phases have also been investigated.

Previously, it was demonstrated that TiO_2 and BaO can form complex Ti-Ba mixed structures depending on the experimental conditions. [55] Single crystal surfaces have been studied by LEED, XPS, and STM for the $BaTiO_3$ (100) surface [56] and the $BaTiO_3$ (111) surface. [57,58] Widdra et al studied the structure and thermal stability of epitaxial $BaTiO_3$ films on Pt (111). [59] According to their results, for coverages up to 1 ML, a hexagonal $BaTiO_3$ (111) structure was observed upon annealing at 1050 K which is rotated by 30° with respect to the Pt(111) substrate. Thicker films of 4 ML demonstrate a $BaTiO_3$ (111)-(1x1) structure in LEED which coincides with a Pt(111)-(2x2) unit cell. Furthermore, the re-oxidised $BaTiO_3$ exhibited a $(\sqrt{3}x\sqrt{3}) R30^\circ$ structure which is well-known for the $BaTiO_3$ (111) single crystal surface.

Although, much more effort has been spent on particular alkaline-earth oxide surfaces such as MgO surfaces, relatively fewer studies exist on BaO surfaces. Grönbeck et al. performed DFT calculations for NO_2 adsorption on BaO (100) films supported on Pt surface. [60] Additionally, the polar BaO(111) facets are studied less often than the (100) facets due to their inherent relative instability of the (111) surface. [41]

Thus the main aim of the current study is to elucidate the fundamental aspects and the surface chemistry of BaO overlayers grown on Pt(111) substrate towards NO_x species, as an “reverse model catalyst”. [61] In order to achieve this, surface sensitive techniques were exploited such as XPS, TPD and LEED under UHV conditions. BaO layers were then grown on the $\text{TiO}_2/\text{Pt}(111)$ model system and the interaction between BaO films and TiO_2 films was studied at different annealing temperatures. In addition, the surface reactivity of this model catalyst system was also investigated by the reaction of $\text{NO}_2(\text{g})$ and $\text{CO}_2(\text{g})$ with a $\text{BaO}/\text{TiO}_2/\text{Pt}(111)$ model catalyst.

2 EXPERIMENTAL

2.1 Ultra-High Vacuum Experimental Set-up

It is clear that the composition of the topmost surface must remain essentially constant during an atomically well-defined surface science experiment. This means that the rate of arrival of reactive species from the surrounding gas phase must be kept at a low value. Validity of this requirement can be readily evaluated from the simple kinetic theory of gases. The rate of arrival of atoms or molecules “ r ” from a gas number of density n per unit volume and with an average velocity c_a is given by: [62]

$$r = 3.51 \times 10^{22} P / (TM)^{1/2} \quad (17)$$

where P is the pressure was expressed in terms of *Torr*, T is the Kelvin temperature and M is the molecular weight in atomic mass units and “ r ” is given in molecules $\text{cm}^{-2}\text{s}^{-1}$. For instance, N_2 molecules ($M=28$) at room temperature ($T=298$ K) at 1 Torr have an arrival rate of 3.88×10^{20} molecules $\text{cm}^{-2}\text{s}^{-1}$.

With a properly reduced chamber pressure, *the mean free path* (i.e. the average distance between successive collisions) can be extended beyond the vacuum chamber dimensions which results in the collision of molecules only with the chamber walls, minimizing the intermolecular collisions.[63] In this way, metals evaporated from a pure source can reach the target surface intact (i.e. without reacting with background contaminants), ions can be accelerated to high energies, electrons and ions can be scattered from a source and then collected via proper detectors with minimum signal loss. The vacuum level in a given experimental system is conventionally categorized as described in Table 3.

Table 3. Pressure Ranges for Vacuum Technologies.

<u><i>Degree of Vacuum</i></u>	<u><i>Pressure Range</i></u>
Low	1000-1 mbar
Medium	1-10 ⁻³ mbar
High	10 ⁻³ -10 ⁻⁷ mbar
Ultra-High	10 ⁻⁷ -10 ⁻¹⁴ mbar

In the current work, all of the experiments were performed in a multi-technique UHV surface analysis chamber with a base pressure of 2.0×10^{-10} Torr. In order to maintain the base pressure, three dual-stage rotary vane pumps (RVP), one turbo pump (TMP) and one titanium sublimation pump (TSP) were utilized. The pressure in the UHV chamber was measured by a Bayard-Alpert type ionization (ion) gauge and a thermocouple (TC) gauge, while the pressure of the gas manifold was measured by a capacitance manometer and a TC gauge. The UHV chamber is equipped with an Al/Mg K α dual anode X-ray source and a double-pass cylindrical mirror analyzer (CMA) for XPS, LEED optics, and a quadrupole mass spectrometer (QMS) for TPD and residual gas analysis (RGA). Atomically polished double-sided Pt (111) single crystal (10 mm diameter, 2 mm thickness from MaTeck) was used as a substrate. The single crystal was mounted on a tantalum sample holder and assembled to a high-precision manipulator. The sample temperature was monitored by a K-Type thermocouple which was spot-welded on the peripheral edge of the crystal. The clean Pt(111) was obtained by multiple cycles of Ar⁺ sputtering at 1.5 kV at room temperature (RT) and subsequent heating to 1073 K in vacuum. Schematic representation of the UHV surface analysis chamber is shown Figure 6.

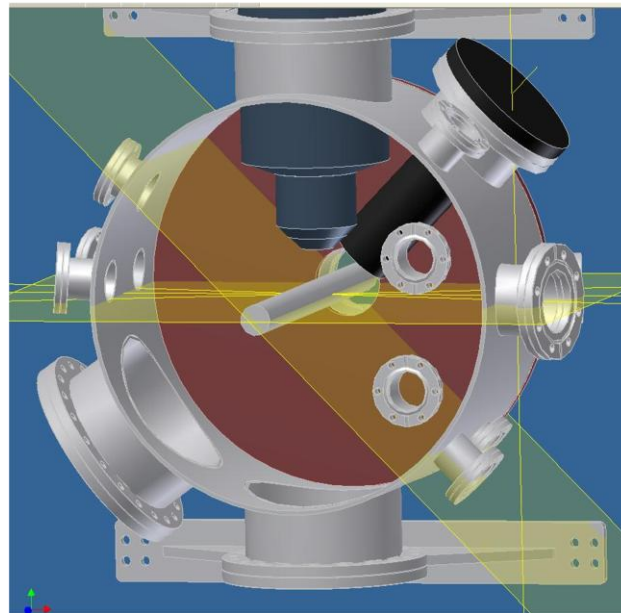
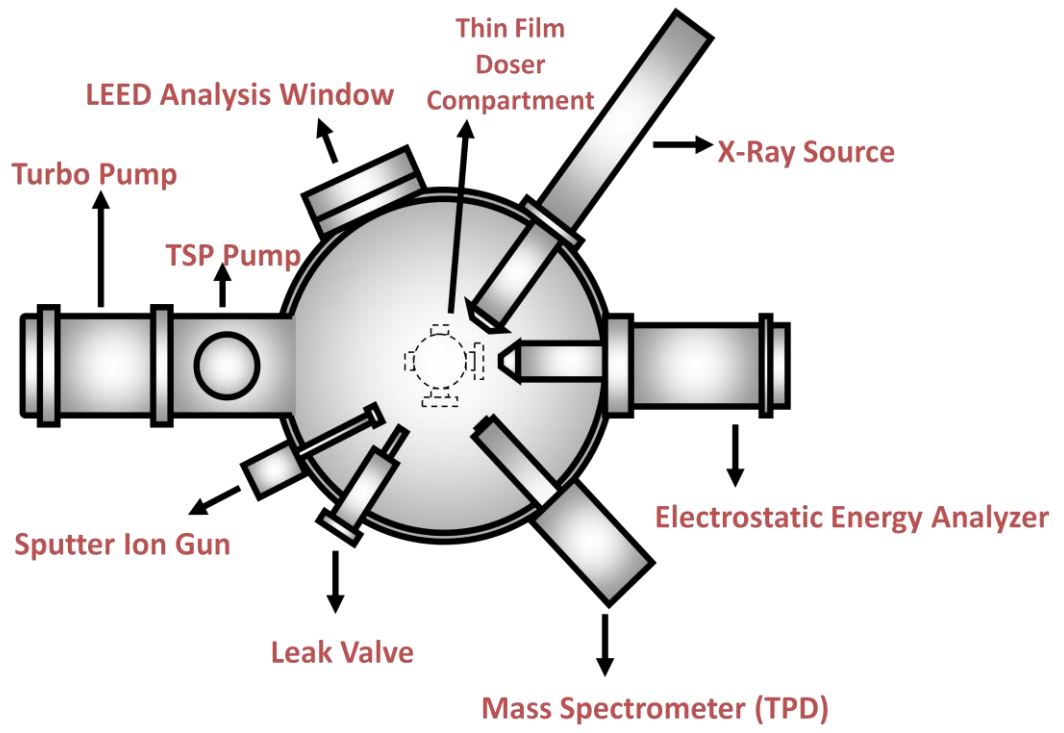




Figure 6. The visual representations of multi-technique UHV surface analysis chamber.

2.2 UHV Compartments

2.2.1 Sputtering Ion Gun (LK Technologies NGI3000 Sputtering Gun)

Sputtering is the removal of surface atoms with energetic particle bombardment. It is caused by the collisions between the incoming particles (i.e. ions) and the atoms in the near surface layers of a solid.[66] Generally, an incoming

particle collides with the atoms of the solid, transferring energy to the atomic nuclei. A surface atom becomes sputtered if the energy transferred to it has a component normal to the surface which is larger than the surface binding energy. This is usually approximated by the heat of sublimation which is mostly smaller than the displacement energy necessary to create a stable dislocation. The LK Technologies Model NGI3000 Ion Gun with control electronics is designed for the cleaning of surfaces by noble gas ion sputtering with beam energies up to 3 keV and ion currents up to 25 μA . In the current UHV system, argon gas is used for sputtering. The gun employs a novel gas injection system which allows sputtering to take place at a typical Ar (g) pressure of 1×10^{-6} Torr. In this system the gas to be ionized by electron impact ionization is injected directly into an enclosed ionization region which houses a filament and a grid structure. The ion beam is then accelerated out of the ionization chamber to the target. The gun is usually provided with an integral leak valve to supply a source of noble gas (i.e. Ar).

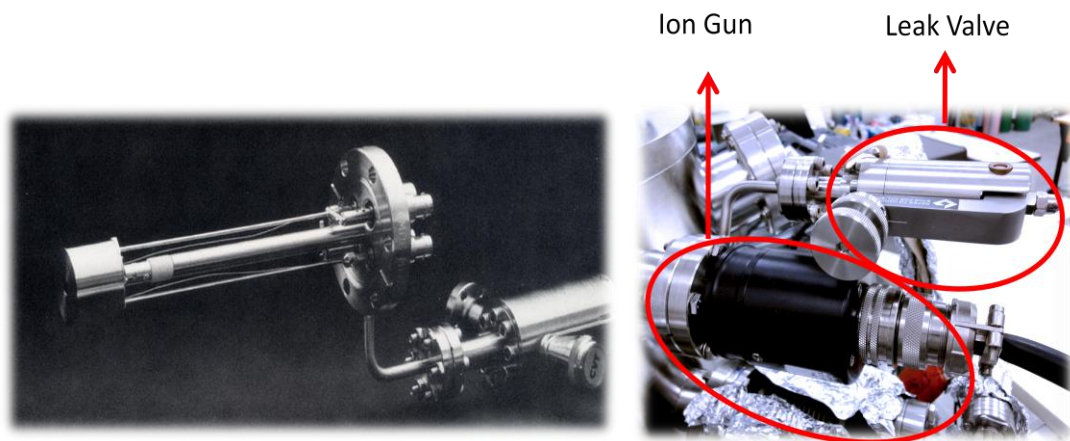


Figure 7. LK technologies sputtering ion gun with a high-precision leak valve.

The NGI3000 has variable beam voltage between 0.2 to 3 kV values. The thoriated iridium filament is used as the electron bombardment source. The beam diameter depends on the length between the ion gun and target. Typical distances from the gun end to the target are 5-15 cm. The beam has a gaussian shape and 3 cm diameter at 14 cm gun to target length. The gun doesn't need a differential pumping stage and the nominal source pressure is typically 5×10^{-5} Torr when the nominal chamber pressure is 1×10^{-6} Torr. For initial operation or after exposure to

atmosphere, the ion gun should be degassed by operating the gun under high vacuum at 20 mA for a period of 30 minutes.

2.2.2 Precision XY-Z Manipulator Platforms (McAllister MC1500/2000)

The MC1500/2000 series of XY translators are utilized to travel in XY-direction. They are available in both ± 25 mm and ± 12.5 mm traveling circular pattern.



Figure 8.The MC1500/2000 series XY translator with manual micrometer controllers.

The micrometers and XY slides are lubricated with high temperature grease (e.g. MoS₂-paste). It must be relubricated after every third or fourth bake out. It is not suggested to use hydrocarbon grease since hydrocarbon greases will dry out during baking. After several bake out, it also may be necessary to re-lubricate the bearings. The stainless steel bellows is made from thin material and is fragile. Therefore, one must be careful about the other objects that can hit the bellows. Bake out temperature shouldn't exceed 100 °C with the micrometers attached during bake out. Higher temperatures can damage the precision components. Lateral alignment of the X-Y slides is maintained by special crossed roller bearings made of hardened carbon steel and these bearings can corrode. For this reason, moisture or condense on or in the bearings should be avoided. Exposure and overcooling of the bearings with liquid nitrogen should be also prevented.

Z-axis translator in combination with the MC2000 XY platform produce a long travel XYZ manipulator. The lower fixed flange is fitted with support guides for long sample probes and this significantly reduces the vibrations. In addition to this, it has a slim LN₂dewar which allows efficient cooling.

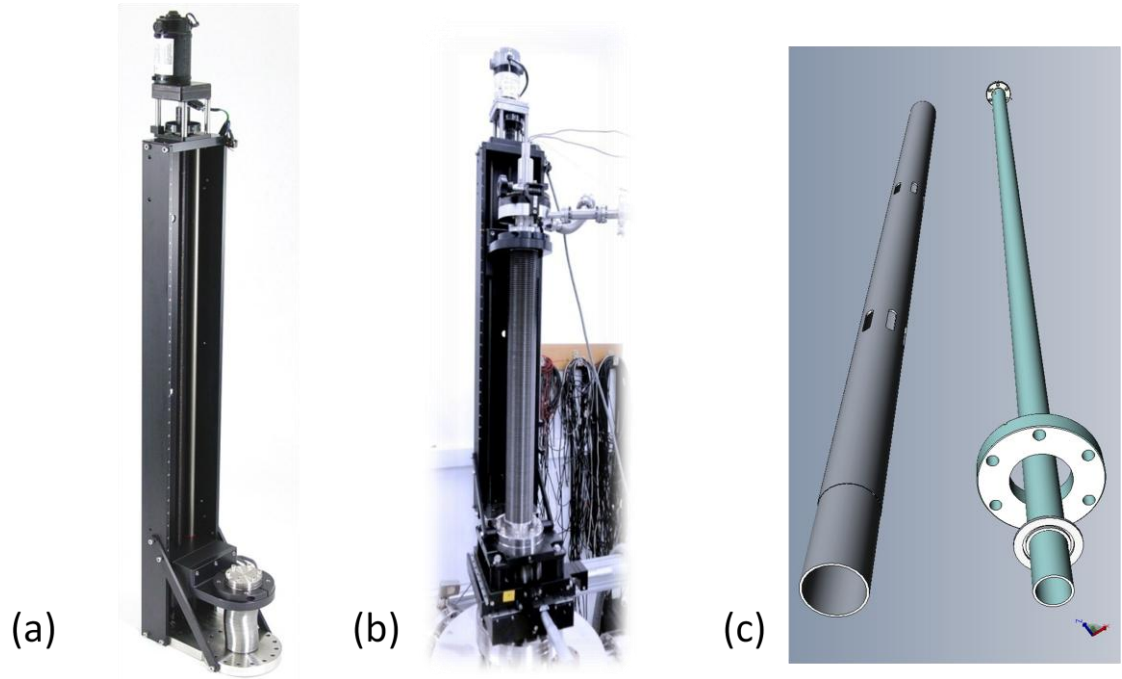


Figure 9.(a) The ZA-series Z-axis translator (b) currently used complete XYZ- θ manipulator including a DC motor used (c)the visual representation of the manipulator probe.

The lead screws are coated with molybdenum disulfide. These coatings degrade over time, due to moisture in the atmosphere. After bake out, the screws must be relubricated with the silicone-based molybdenum disulfide grease. The normal bake-out temperature is 150 °C but higher temperatures can be used, in this case, lubrication must be done more frequently. The ZA series of translators has been designed to allow motors, in our UHV Manipulator includes the DC motor with hand held forward/reverse switch by a variable speed control.

Differentially-Pumped Rotary Platform (DPRF) is used for 360⁰ continuous rotation at 1×10^{-11} Torr. It includes fine adjust drive and 0.1⁰ vernier scale.

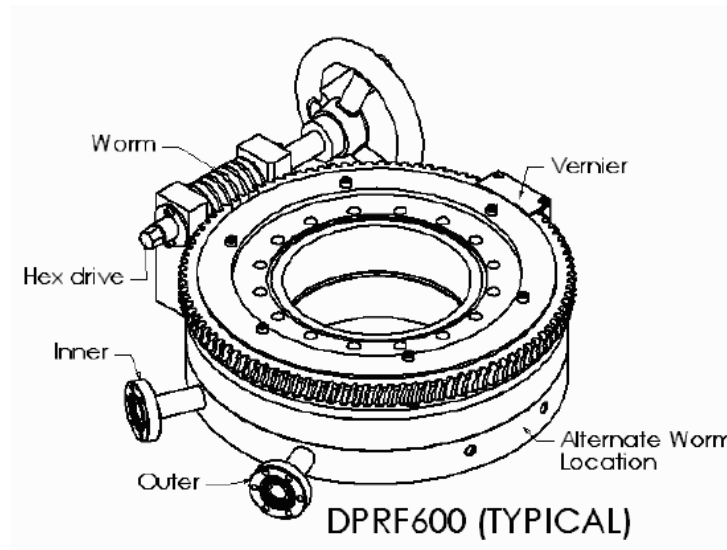


Figure 10. Differentially-pumped-rotary-platform (rotary seal) used in manipulator part.

After several bake outs, the worm-shaft must be relubricated with MoS₂ grease. The only metal components exposed to vacuum are type 304 stainless steel and 6061 aluminum. There are two differential pumping volumes, isolated by three fluorocarbon seals. These volumes are pumped through the 1, 33" OD mini-ports located at the perimeter of the seal.

2.2.3 Thin Film Doser Compartment

Thin films with different thicknesses can be prepared by chemical vapor deposition technique. Current UHV thin film doser compartment consists of home-made metal evaporators including Pt, Au, Ti and Ba. Two view ports are utilized in order to view the positioning of the sample at the optimum location in front of the dosers.

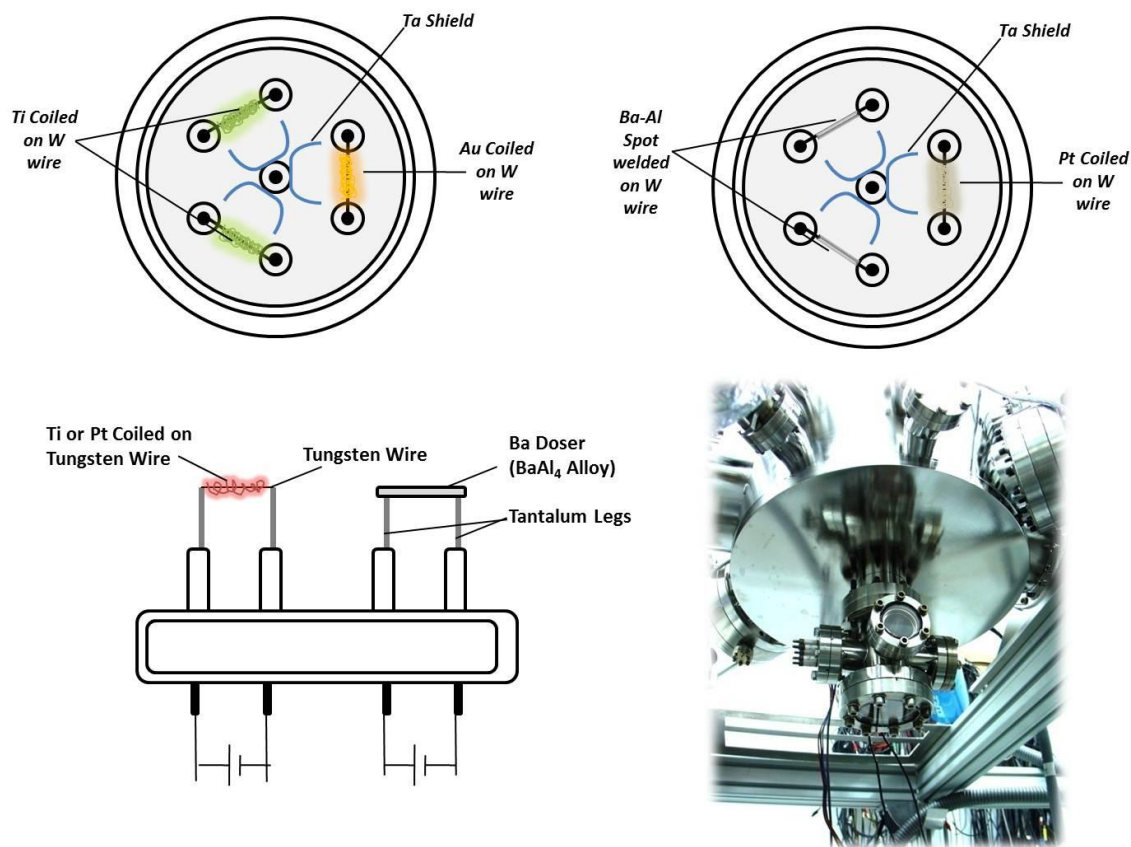


Figure 11. Thin film doser compartment and types/locations of particular dosers.

For the preparation of the Pt, Au, Ti dosers, high-purity wires of these metals with proper diameters (Pt=0.05mm, Au=0.05mm, Ti=0.125mm) were coiled up around a relatively thicker tungsten wire. By passing DC current through tungsten wire with an adjustable voltage/current supply, these metals can be heated up a certain temperature at which evaporation takes place. If the sample is located within the line of sight of the evaporator, metal particles in the gas phase accumulate on the surface of the sample. Oxide thin films of related metals are then prepared by heating the sample at high temperatures in an oxidative environment. In order to prevent metal deposition on the critical components of the UHV chamber and other analytic apparatus, tantalum screens were spot-welded around the dosers. These screens also prevent cross-contamination of adjacent metal dosers of different types.

For the production of the home-made Ba-doser, Bagetter material $BaAl_4$ alloy (ST2/FR wire, SAES Getters) was spot welded on Ta legs. These evaporable getters are typically provided in the form of a stable barium-aluminum alloy powder

compressed into a metal ring container. The ring-shaped metal container offers the advantage of electrical conductivity. Activation of the getter by resistive heating generates atomic Ba (g) which can readily be deposited on the surface of the substrate. When the getter temperature is raised to approximately 1250 °C, Ba (g) vapor pressure can reach above 2 mbar. Thus, during Ba deposition, gentle heating with a Ba-doser current of c.a. 10 A is used in order to achieve a controlled dosing condition.

2.2.4 Temperature Controller (Heat Wave Labs Model 101303-46A)

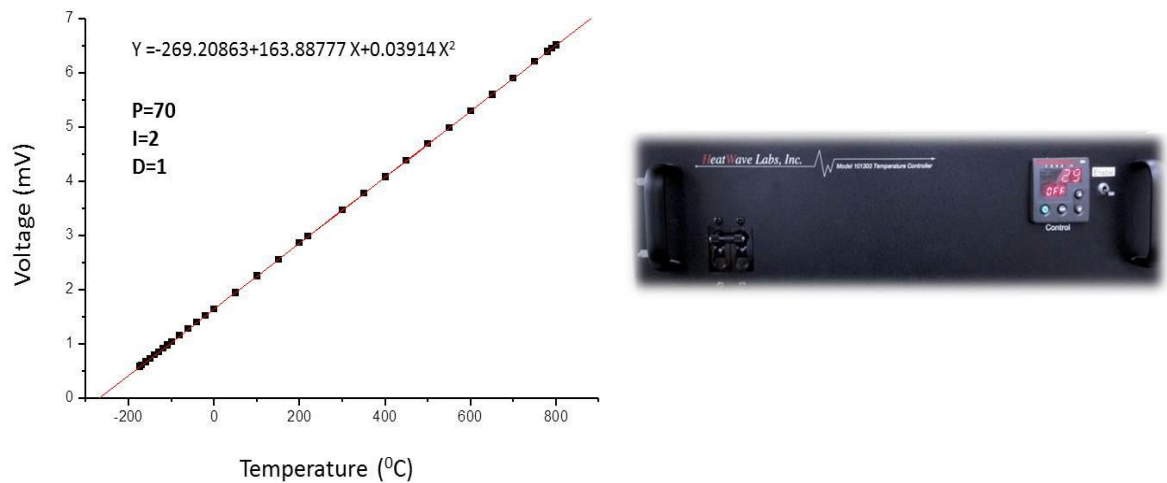


Figure 12. Sample temperature controller unit used in UHV chamber.

Sample temperature was manipulated with an electronic temperature controller (Heat Wave Labs Model 101303-46A). The sample temperature is measured with a K-type thermocouple. Type K thermocouple consists of chromel (90% nickel + 10% chromium with 0.05 mm thickness), alumel (95% nickel + 2% manganese + 2% aluminum + 1% silicon with 0.05 mm thickness) alloys. It can be used for the temperature interval of 20 K and 1600 K. Our working temperature interval was between 80 K to 1073 K. After several optimization tests, PID parameters for a linear heating protocol were determined. The following parameters were used in the PID algorithms during the linear sample heating ramps: P=70, I=2, D=1. The first parameter, proportional control, depends only on the difference between the set point and the process variable. This difference is referred to as the

“error term”. Therefore, proportional control determines the ratio of output response to the error signal. When the value is in the band, the controller adjusts the output based on how close the process value is to the set point. The second parameter, integral, determines the speed of correction. The integral component sums the error term over time. A low integral value causes a fast integration action. The last parameter, derivative, is used to minimize the overshoot in a PI-controlled system. It adjusts the output based on the rate of change in the temperature or process value. If derivative value is too much, then system becomes sluggish. In all of the current experiments, a resistive linear heating rate of 1 K/s was chosen and all the system parameters were optimized according to this linear ramp rate.

2.3 Surface Analytical Techniques

2.3.1 XPS (X-Ray Photoelectron Spectroscopy)

XPS provides information about the elemental composition, the oxidation state of the elements and, in some cases, the dispersion of one phase over another. XPS measures the kinetic energy of photoelectrons emitted from a material due to the photoelectric effect.

Peaks in the XP spectra are described using the quantum numbers of the photoelectrons that are involved in the photoemission process. A particular photoemission peak is labeled via “ nl_j ” formalism [67] in which the principal quantum number “ n ” takes the integer values within “1, 2, 3, ..., n ”, the orbital angular momentum “ l ” takes integer values within “0, 1, 2, 3, ..., $n-1$ ”. and Quantum number “ l ” is represented by historical spectroscopic notation in the form “s, p, d, f...”. The peaks in the XP spectra that are derived from orbitals with an angular momentum quantum number greater than 0 are usually split into two different signals. This is the result of the coupling interaction between the orbital angular momentum “ l ” of an electron in a given orbital and the magnetic field associated with its spin quantum number “ s ” originating from the intrinsic angular momentum of that particular electron. The spin angular momentum quantum number can assume values of $\pm\frac{1}{2}$. These two angular momentum vectors can couple either in a favorable (constructive) or

in an unfavorable (destructive) fashion yielding a resultant quantum number “j” with a magnitude $j = |l \pm s|$. For instance, the Pt 4f yields two photoemission peaks, 4f_{7/2} (with $l=3$ and $j=3+1/2$) and 4f_{5/2} ($l=3$ and $j=3-1/2$). The degeneracies “g” of the electronic states associated with a particular photoemission peak is given by “ $g = 2j+1$ ”. Relative degeneracies associated with different spin-orbit splitting peaks (i.e. doublets) dictate the relative intensities of each of the doublets. For example, for a photoemission process involving d-orbital electrons, the relative integrated XPS intensities of the 3/2 and 5/2 peaks are 2:3. Strength of spin orbit coupling defines the binding energy spacing between the doublets. For a given value of both n and l , the separation increases with the atomic number of the atom. For a given atom, it decreases both with increasing n and with increasing l . X-ray notation is also an alternative notation where letters K, L, M etc. are used instead of the principal quantum numbers, while subscript numbers refer to the j values.

Table 4. The relationship between quantum numbers, spectroscopists’ notation and X-ray notation.[67]

n	Quantum numbers			Spectroscopists’ notation	X-ray notation
	l	s	j		
1	0	+1/2, -1/2	1/2	1s _{1/2}	K
2	0	+1/2, -1/2	1/2	2s _{1/2}	L_1
2	1	+1/2	1/2	2p _{1/2}	L_2
2	1	-1/2	3/2	2p _{3/2}	L_3
3	0	+1/2, -1/2	1/2	3s _{1/2}	M_1
3	1	+1/2	1/2	3p _{1/2}	M_2
3	1	-1/2	3/2	3p _{3/2}	M_3
3	2	+1/2	3/2	3d _{3/2}	M_4
3	2	-1/2	5/2	3d _{5/2}	M_5
					etc.

XPS is based on the photoelectric effect, in which an atom absorbs photon energy, $h\gamma$, after which a core or valence electron with binding energy E_b is ejected with kinetic energy, E_k : [68]

$$E_k = h\gamma - E_b - W \quad (18)$$

where E_k is the kinetic energy of the photoelectron, h is the Planck’s constant, γ is the frequency of the exciting radiation, E_b is the binding energy of the photoelectron

with respect to the Fermi level of the sample and W , is the work function of the spectrometer. E_k is the experimental quantity measured by the spectrometer, this is dependent on the incoming X-Ray photon energy of the and therefore it is not an intrinsic material property. The process of photoemission is shown schematically in Figure13:

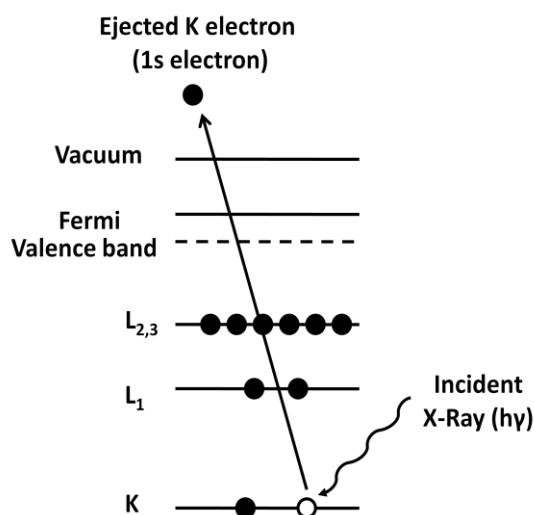


Figure 13. Schematic diagram of the XPS process that demonstrates the photoionization of an atom by ejection of a 1s electron. (adapted from ref. [67]).

The characteristic peaks in the spectrum are formed by the photoelectrons which are ejected without any loss in kinetic energy. However, photoelectrons which undergo inelastic scattering suffer various amounts of kinetic energy losses. These electrons contribute to the background of the spectrum. In XPS, the intensity of photoelectrons is measured as a function of their kinetic energies and the XPS spectrum is a plot of photoelectron intensity versus the binding energy. Mg K α (1253.6 eV) and Al K α (1486.3 eV) are commonly used X-ray sources.[68] There are two frequently used types of photoelectron energy analyzer exploited in the XPS analysis, the cylindrical mirror analyzer (CMA) and the hemispherical analyzer (HSA). In our XPS set up, a double-pass CMA (Riber Model EA 150 Analyser) is utilized. A typical CMA consists of two concentric cylinders as illustrated in Figure 14:

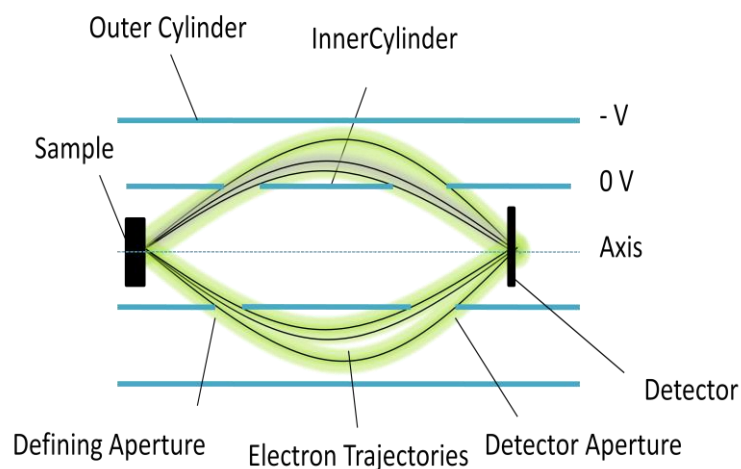


Figure 14. Schematic diagram of the cylindrical mirror analyzer (CMA). (adapted from ref. [67])

A certain proportion of the emitted electrons will pass through the defining aperture in the inner cylinder and, depending on the potential applied to the outer cylinder; electrons of the desired energy and take-off angle (i.e. 48° with respect to the sample surface) will pass through the detector aperture and be re-focused at the electron multiplier. Therefore, an energy spectrum can be built up by only scanning the potential on the outer cylinder to produce spectrum of intensity (in counts per second) versus electron kinetic energy.

Binding energies are not only element specific but also include chemical information, since the chemical state of the atom is dependent on the energy levels of the core electrons. Chemical shifts are typically in the range of 0 to 3 eV.[68] In general, the binding energy increases with increasing oxidation state, exceptional cases exist where a reverse trend is observed (e.g. Ba, Cu, Zn, Ag, Cd, Cs) or B.E values stay rather constant with changing oxidation states (e.g. Ca and Sr). In order to understand the meaning of a binding energy, final state effects must be considered. The photoemission data represent a state from which electron has just left. Therefore, the binding energy of a photoelectron contains both information on the state of the atom before photoionization (the initial state) and on the core-ionized atom left behind after the emission of an electron (the final state). For the identification of

chemical states, the accurate determination of line energies is essential. In order to determine line energies correctly, the voltage scale of the instrument must be precisely calibrated, a line with a narrow sweep range must be recorded with good statistics, and accurate correction must be made for static charge if the sample is insulating.[69] During analysis, insulating samples get a steady-state charge. The steady state charge is usually positive, and this can be minimized by adding slow electrons to the vacuum space with a neutralizer or flood gun. In the current work, such charging events are minimized by the use of a metallic substrate (i.e. Pt(111) and ultrathin metal-oxide films.

However, the exact determination of the extent of charging is a problematic issue. There are several methods for post-analysis charge correction. In our experiments we used two different post-analysis charging correction methods. In seldom cases, we used an internal standard, such as a hydrocarbon moiety on the sample. The value of 284.6 eV then can be taken as a reference for the C1s line. In most of the cases, on the investigated samples, C1s signal was below the detection limit due to the atomically clean surfaces prepared at c.a. 10^{-10} Torr. Thus, B.E. value of the Pt(111) support material was used as a reference by assuming that the inert Pt substrate stays mostly in its metallic (Pt^0) state corresponding to a $Pt4f_{7/2}$ B.E. value of 71.1 eV.

XPS can also be used for quantitative analysis. The atomic percentage of the elements on the sample surface can be determined by dividing the corresponding peak areas by the sensitivity factors and expressing them as a fraction of the summation of all normalized intensities as given below:[67]

$$[A] \text{ atomic \%} = \left\{ \frac{I_A}{F_A} / \sum(I/F) \right\} \times 100\% \quad (19)$$

The calculation of the surface composition by this method presumes that the sample is homogeneous within the analysis volume. Photoelectrons used in XPS have kinetic energies typically in the range of 0.2 to 1.5 keV. The probing depth of XPS (usually taken as 3λ) varies between 1.5 and 10 nm depending on the kinetic energy of the photoelectron. With XPS, it is also possible to calculate thickness of an overlayer. In our experiments, BaO over layers on Pt(111) substrate was calculated according to following equation:

$$d_{BaO} = \lambda \sin \theta \ln \left(\frac{I_{Pt}^{\infty} - I_{Pt}}{I_{Pt}} + 1 \right) \quad (20)$$

where λ is the inelastic mean free path of the electrons in BaO films (for 1415.6 eV energy of Pt4f_{7/2} electrons, λ was estimated from *QUASES-IMFP-TPP2Mver.2.2* [70] programming as 28.9 Å), θ is the angle between the surface plane and outgoing photoelectrons and it is 48° in our case, I_{Pt}^{∞} is the intensity of the Pt4f signal of the clean Pt substrate, and I_{Pt} is the intensity of Pt4f signal of the sample with BaO film.

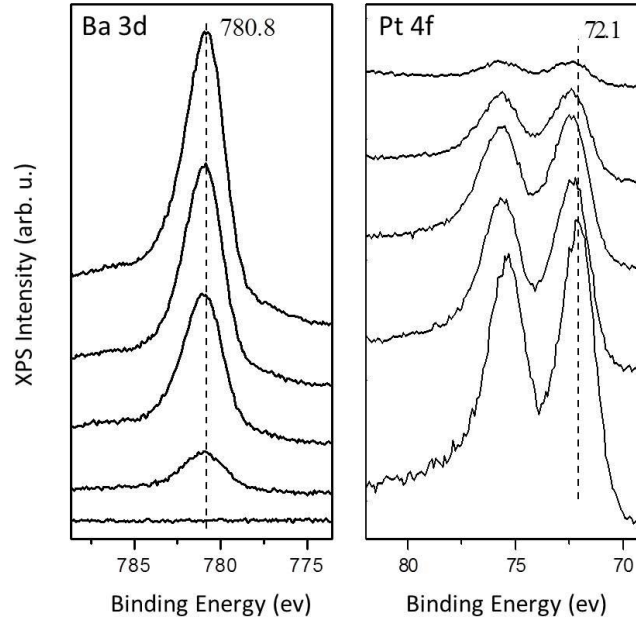


Figure 15. Ba3d and Pt4f XPS spectrum were taken during growth of 10 MLE BaO_x phases on Pt(111) substrate.

XPS spectrum according to Ba3d and Pt4f region was taken after the preparation of 10 MLE BaO_x film grown on Pt(111) substrate. One can see the monotonic increase of the Ba3d signal intensity and attenuation of Pt4f intensity. Here, the clean Pt substrate XPS intensity is 5543 c.p.s. (i.e. $I_{Pt}^{\infty} = 5943.3$) and attenuated Pt4f intensity is 937 c.p.s. (i.e. $I_{Pt} = 937$). According to the equation 20:

$$d_{BaO} = 28.9 \times \sin 48 \times \ln \left(\frac{5943.3 - 937}{937} + 1 \right)$$

$$d_{BaO} = 40 \text{ \AA}$$

BaO has a $3.9 \times 5.5 \text{ \AA}^2$ lattice parameter if it has a (110) termination which we observed for thicker coverages of BaO (discussed later) occurs. If we take 3.9 \AA lattice parameter (this is the spacing between two BaO(110) overlayers), we can calculate thicknesses of BaO_x phases in terms of monolayer which equals to $40 \text{ \AA} / 3.9 \text{ \AA} = \sim 10 \text{ MLE}$.

This approach assumes that the overlayer species attenuating the substrate signal is a well-dispersed homogenous film. However, it should be noted that the morphology of some of the overlayers synthesized in the current work did not show such a homogenous nature due to the presence of 3D clusters or the existence of polycrystalline or even amorphous domains. Thus, the film thickness calculations in such cases should be treated as rough estimations.

The XPS spectrum becomes complicated due to the presence of additional features, such as X-ray satellites and X-ray ghosts. X-ray satellites are present if the radiation source is not monochromatic. They occur because the characteristic transitions are excited by a minor component of the X-ray spectrum, e.g., $AlK_{\alpha 3,4}$, $AlK_{\alpha 5,6}$, AlK_{β} . [67] For each photoelectron peak that results from the K_{α} X-ray photons, there is a group of minor peaks at lower binding energies, with intensity and spacing characteristic of the X-ray anode material. The pattern of such satellites for Mg and Al is shown in Table 5: [69]

Table 5. X-ray satellite energies and intensities. [69]

X-ray line	Separation from $K\alpha_{1,2}$ (eV) and relative intensity ($K\alpha_{1,2} = 100$)	
	Mg	Al
$K\alpha'$	4.5(1.0)	5.6(1.0)
$K\alpha_3$	8.4(9.2)	9.6(7.8)
$K\alpha_4$	10.0(5.1)	11.5(3.3)
$K\alpha_5$	17.3(0.8)	19.8(0.4)
$K\alpha_6$	20.5(0.5)	23.4(0.3)
$K\beta$	48.0(2.0)	70.0(2.0)

X-ray ghosts may result from mixing in a twin anode gun (the generation of a small amount of characteristic X-ray radiation as a result of anode misalignment). These lines can be due to Mg impurity in the Al anode, or vice versa or Cu from the anode base structure or generation of X-ray photons in the aluminum foil X-ray window.

2.3.2 Low Energy Electron Diffraction (LEED) Technique

Low-energy electrons with energies varying from about 20 to 500 eV, are ideal probes for surface science studies because they are easily scattered by atoms both elastically and inelastically.[71] If they penetrate into a solid for more than four or five atomic layers they are absorbed and disappear into the electron sea, however, if they survive absorption in the first two or three atomic layers and back-scattered out of the crystal, they can provide information about the atomic arrangement in the surface layer.

Consider the reflection of two parallel electrons of the same wavelength by two adjacent planes of a lattice as shown in Figure 16:

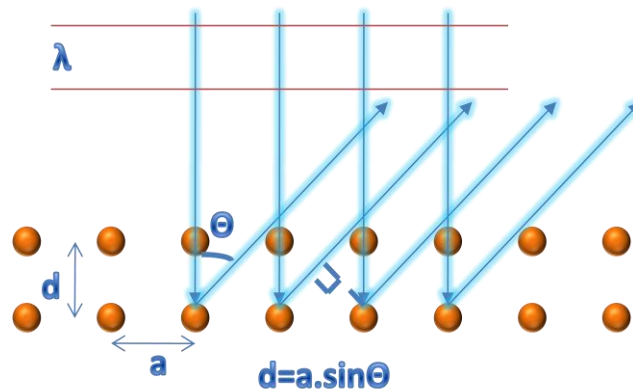


Figure 16. Bragg's diffraction condition (adapted from ref. [72]).

where θ is the **glancing angle**. For many glancing angles the path-length difference is not an integer number of wavelengths, and the beams interfere destructively. However, when the path-length difference is an integer number of wavelengths, the

reflected beams are in phase and interfere constructively. This is explained by **Bragg's law**:^[72]

$$n\lambda=2d\sin\theta \quad (21)$$

Reflections with $n=2, 3, \dots$ are called second order, third-order and they corresponds to path-length differences of 2, 3, ... wavelengths. Bragg's law is used in the determination of the spacing between the layers in the lattice, once the angle θ corresponding to a reflection has been known, d can be calculated.

LEED experiments are performed with a narrow beam of electrons with energy between 20 eV and 500 eV. They must be incident on a planar single crystal surface at a given angle. The sample surface must be well-oriented, electrically grounded, planar and either clean or contaminated in a controllable manner. Experiment for surface structure analysis consists of three main parts: the electron gun to generate the incident electron beam, a manipulator to hold and orient the sample and a detector to monitor the diffracted beams.

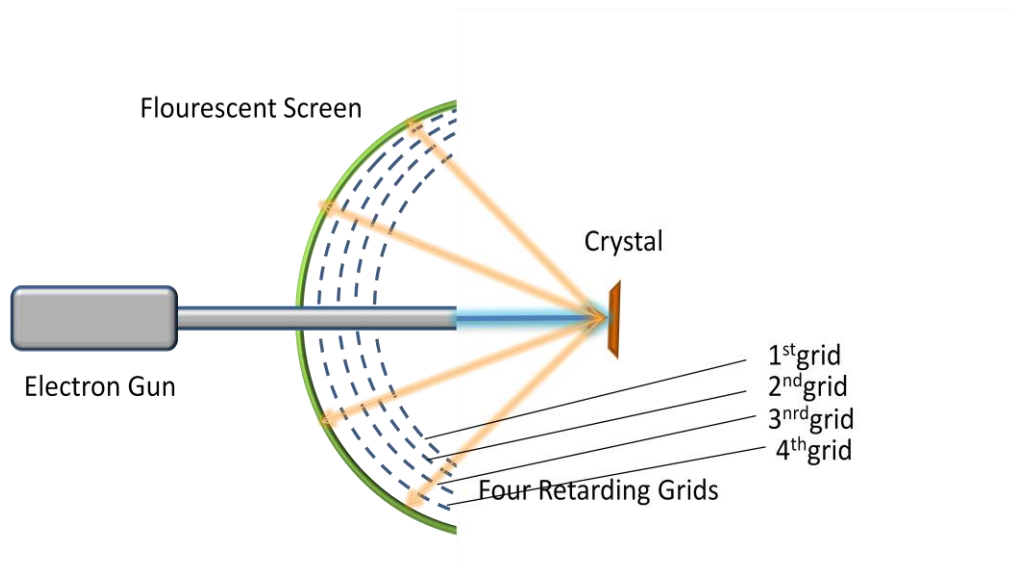


Figure 17. Schematic representation of Low Energy Electron Diffraction Technique.

Electrons are generated either by on-axis, indirectly heated, cathodes or by off-axis tungsten filaments, with energies that can be differ between 0 and 800 eV.

The effective diameter of the electron beam is about 1 mm.[71]for the display system; the retarding-field energy analyzer is used. It consists of four hemispherical concentric grids and a fluorescent screen as shown in Figure 17.[73]The first grid is connected to the earth ground to provide field-free region between the sample and the first grid. This reduces an undesirable electrostatic deflection of diffracted electrons. A negative potential is applied to the second and third grids (suppressor grids) to allow the transmission of the elastically scattered electron to the fluorescent screen in a narrow range. The fourth grid is usually grounded to reduce field penetration of the suppressor grids by the screen voltage when a potential of a few kilovolts is applied to the screen in order to make the diffraction beams visible.

In order to consider the symmetry of a perfectly ordered surface, there are two concepts fundamentally must be known, *lattice* and *basis*. The lattice consists of a two-dimensional array of points which possess translational symmetry.[73]The basis, on the other hand, represents the arrangement of the atoms with respect to the lattice points of the surface, for instance it specifies all atomic positions within one unit cell. The five different surface lattices and their diffractions in the LEED are shown in Figure 18:

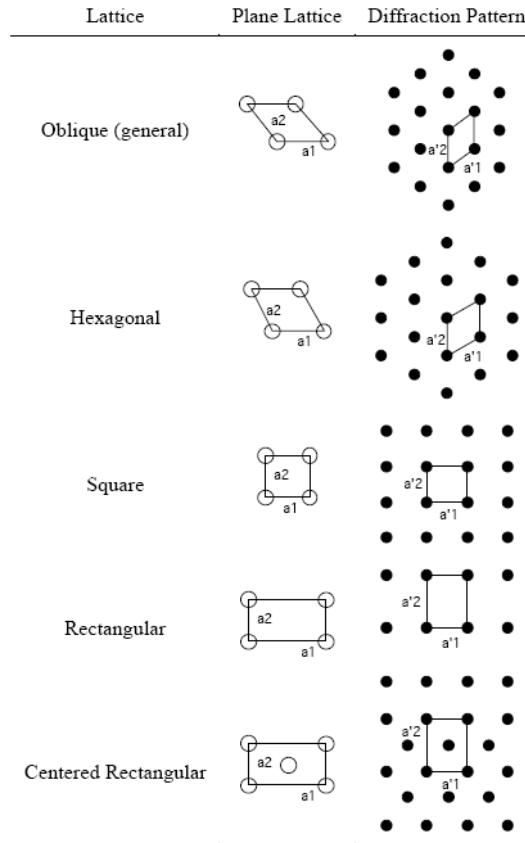


Figure 18. Diffraction patterns of five plane lattices. [73]

A two-dimensional solid surface contains a primitive unit cell which is defined by the translational vectors \vec{a}_1 and \vec{a}_2 . These vectors can be defined in Cartesian coordinates \hat{x} and \hat{y} , the unit cell of the surface can be described by the matrix \mathbf{A} , the elements A_{ij} of which are related to the translational vectors

$$\vec{a}_1 = A_{11}\hat{x} + A_{12}\hat{y} \quad (22)$$

$$\vec{a}_2 = A_{21}\hat{x} + A_{22}\hat{y} \quad (23)$$

Associated with the (real space) the two dimensional unit cell in reciprocal space can be described by a matrix \mathbf{A}^* .

The relationships between the primitive translation vectors of the surface, \vec{a}_1 and \vec{a}_2 and the primitive translation vectors of the reciprocal lattice, \vec{a}_1^* and \vec{a}_2^* can be written as

$$\vec{a}_1^* = 2\pi \left[\frac{\vec{a}_2 \times \vec{n}}{\vec{a}_1 \cdot (\vec{a}_2 \times \vec{n})} \right] \quad (24)$$

$$\vec{a}_2^* = 2\pi \left[\frac{\vec{n} \times \vec{a}_1}{\vec{a}_2 \cdot (\vec{n} \times \vec{a}_1)} \right] \quad (25)$$

when \vec{n} is taken to be a unit vector normal to the surface.

If a surface lattice is characterized by two base vectors \mathbf{a}_1 and \mathbf{a}_2 , the reciprocal lattice follows from the definition of the reciprocal lattice vectors \mathbf{a}_1^* and \mathbf{a}_2^* : [68]

$$\vec{a}_i \cdot \vec{a}_j^* = \delta_{ij} \quad (26)$$

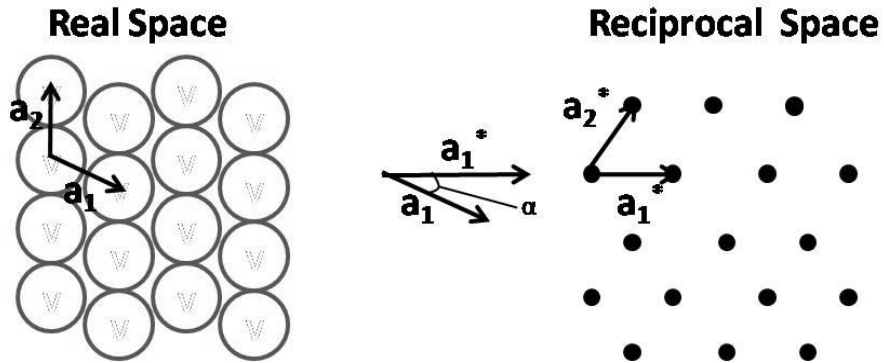
where δ_{ij} is the Kronecker delta, $\delta_{11} = \delta_{22} = 1$, $\delta_{12} = \delta_{21} = 0$. (The dot product is equal to $|\vec{a}_i \times \vec{a}_j| \cos\alpha$) Therefore, when \vec{a}_1 and \vec{a}_1^* parallel:

$$\vec{a}_1 \cdot \vec{a}_1^* = 1 \quad (27)$$

$$|\vec{a}_1 \times \vec{a}_1^*| \cos\alpha = 1 \quad (28)$$

$$|\vec{a}_1| = 1/|\vec{a}_1^*| \quad (29)$$

For instance, for an fcc (111) surface;



\mathbf{a}_1^* is not perpendicular to \mathbf{a}_1 and \mathbf{a}_2^* is not perpendicular to \mathbf{a}_2 , $\alpha = 30^\circ$, $\cos\alpha = \sqrt{3}/2$,

$$\mathbf{a}_1^* \cdot \mathbf{a}_1 = 1 \quad (30)$$

$$|\mathbf{a}_1^* \times \mathbf{a}_1| \cos\alpha = 1 \quad (31)$$

$$|\mathbf{a}_1^* \times \mathbf{a}_1| \sqrt{3}/2 = 1 \quad (32)$$

$$|a_1| = 2/\sqrt{3} \cdot (1/a_1^*) \quad (33)$$

Overlayer surface structures may have lattice vectors \mathbf{b}_1 and \mathbf{b}_2 which differ from the substrate lattice vectors \mathbf{a}_1 and \mathbf{a}_2 . However they can be described in terms of the substrate lattice vectors as follows: [74]

$$\mathbf{b}_1 = m_{11}\mathbf{a}_1 + m_{12}\mathbf{a}_2 \quad (34)$$

$$\mathbf{b}_2 = m_{21}\mathbf{a}_1 + m_{22}\mathbf{a}_2 \quad (35)$$

which can be expressed in matrix notation as:

$$\begin{pmatrix} b_1 \\ b_2 \end{pmatrix} = \begin{pmatrix} m_{11} & m_{12} \\ m_{21} & m_{22} \end{pmatrix} \begin{pmatrix} a_1 \\ a_2 \end{pmatrix} \quad (36)$$

or

$$\mathbf{b} = \mathbf{M} \cdot \mathbf{a} \quad (37)$$

A corresponding relationship between reciprocal lattice vectors may be similarly defined as:

$$\mathbf{b}^* = \mathbf{M}^* \cdot \mathbf{a}^* \quad (38)$$

where

$$\mathbf{M}^* = \begin{pmatrix} m_{11}^* & m_{12}^* \\ m_{21}^* & m_{22}^* \end{pmatrix} \quad (39)$$

with a standard matrix algebraic operation, one can relate these matrices as follows:

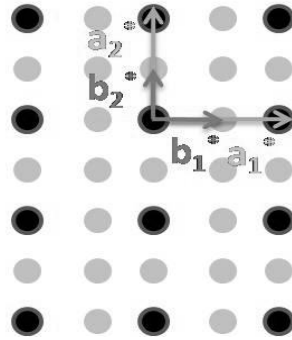
$$\begin{pmatrix} m_{11} & m_{12} \\ m_{21} & m_{22} \end{pmatrix} = 1/\det \mathbf{M}^* \begin{pmatrix} m_{22}^* & -m_{21}^* \\ -m_{12}^* & m_{11}^* \end{pmatrix} \quad (40)$$

where

$$\det M^* = m_{11}^* \cdot m_{22}^* - m_{21}^* \cdot m_{12}^* \quad (41)$$

This relationship is enough to present the real space structure to be derived from the observed diffraction pattern if the appropriate reciprocal lattice vectors are extracted from the pattern observed.

Observed Diffraction Pattern



$$b_1^* = 0.5 a_1^* \quad (42)$$

$$b_2^* = 0.5 a_2^* \quad (43)$$

in matrix notation,

$$\begin{pmatrix} b_1^* \\ b_2^* \end{pmatrix} = \begin{pmatrix} 0.5 & 0 \\ 0 & 0.5 \end{pmatrix} \begin{pmatrix} a_1^* \\ a_2^* \end{pmatrix} \quad (44)$$

from which

$$\det M^* = 0.25 - 0 = 0.25 \quad (45)$$

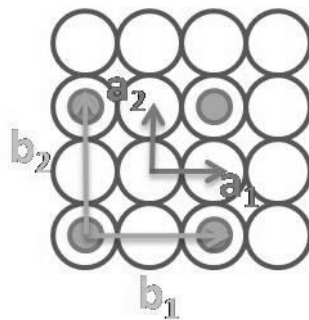
$$M = 1/0.25 \begin{pmatrix} 0.5 & 0 \\ 0 & 0.5 \end{pmatrix} = \begin{pmatrix} 2 & 0 \\ 0 & 2 \end{pmatrix} \quad (46)$$

$$b = M \cdot a \quad (47)$$

therefore, in real space, the over layer structures are described by the lattice vectors,

$$b_1 = 2a_1 \quad (48)$$

$$b_2 = 2a_2 \quad (49)$$



2.3.3 Temperature-Programmed Desorption (TPD)

TPD is a useful technique in surface science, where the desorption of gases from single crystals or polycrystalline materials into the vacuum is examined as a function of desorption temperature.[52]Figure 19 shows a typical schematic set-up for TPD.

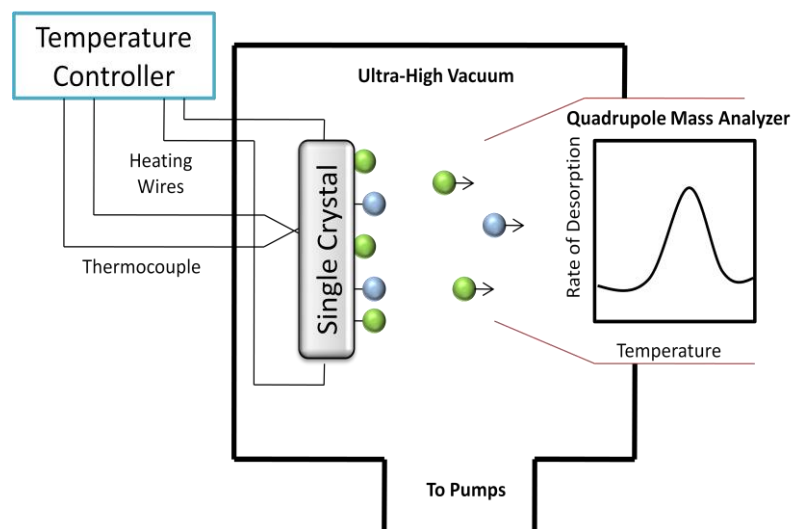


Figure 19. Experimental set-up for Temperature Programmed Desorption (TPD) technique in ultra-high vacuum. (adapted from ref.[68])

The single crystal mounted on a manipulator in a UHV chamber is heated resistively via copper wires. In order to monitor the temperature, a thermocouple which is spot-welded to the back of the crystal is used. Heating rates employed in

TPD can vary from 0.7 to 70 K.s⁻¹, but the usual range is between 1-5 Ks⁻¹. [75] The quadrupole mass spectrometer is utilized in order to measure the concentration of the desorbing species.

The dependence of the rate of evolution of adsorbed molecules from a surface, on the temperature, is given by the general Arrhenius equation, [75]

$$-\frac{dN}{dt} = k_m N^m \exp(-E_d/RT) \quad (50)$$

N is the surface concentration of adsorbed particles per unit area, k_m is frequency factor, m is order of the desorption reaction, E_d is the activation energy of the desorption process and T is the absolute temperature. For m=1 for a first order reaction in which the particles desorb independently of each other, and m=2 for a second order reaction in which the particles must combine before desorption and in which their recombination is rate-determining.

TPD can provide information about the adsorbate coverage, adsorption energy, which in general equals the activation energy of desorption, lateral interactions between the adsorbates, through the coverage dependence of the adsorption energy and the pre-exponential factor of desorption, which can affect the desorption mechanism.

The basic experiment involves adsorption of one or more species molecular species on the sample surfaces at related temperatures and heating of the sample in a controlled manner while the monitoring the evolution of species from the surface back into the gas phase. The data obtained from such an experiment consists of the intensity variation of each recorded mass fragment as a function of temperature. The area under a peak is proportional to the amount of adsorbed species. The kinetics of desorption give information about the aggregation of adsorbed species i.e. molecular vs. dissociative. The position of the peak is related to the enthalpy of adsorption i.e. to the strength of binding to the surface.

2.4 Sample Preparation

2.4.1 Sputtering of the Sample

In order to remove various types of surface contaminations and/or clean the previously grown oxide thin films on the Pt(111) substrate surface, highly energetic Ar^+ ions were emitted towards the surface. For ion bombardment with an oblique angle of incidence, the sputtering yield increases with increasing the angle of incidence up to 70° . In order to monitor the ion current between the sample and the sputter ion gun, Keithley 197 model digital multimeter in the μA reading mode was connected to the sample via one of the copper heating legs while the other multimeter connection was electrically grounded. Then, inert argon gas was sent into UHV chamber through a leak valve and the pressure of the UHV chamber was stabilized at 1×10^{-6} Torr. An important point is that the beam emission must be applied after adjusting the Ar^+ pressure otherwise a discharging might occur in the inner walls of the sputter ion gun. For the energy of the ion beam, the emission with a value of 17 mA and the beam voltage with a value of 1.7 kV have been used during the sputtering procedure. The beam voltage and the emission values must be increased slowly and consecutively. Higher emission and beam voltage values can decrease the sputtering yield since highly energetic Ar^+ ions which can penetrate into single crystal can damage the substrate surface by removing atoms from the top layers of the substrate. Using these sputtering parameters, a typical ion beam current of 10 – 18 μA can readily be achieved during the etching process. In order to remove the oxide thin films such as BaO from the Pt(111) surface, (with a sample placed normal to the sputtering gun), 60 min sputtering and successive flashing to 1073 K is sufficient for an effective cleaning. However, with thicker oxide films such as BaO on TiO_2 on Pt(111), multiple cycles of > 120 min etching followed by flashing to 1073 K is required. In addition to this, the substrate position should be occasionally changed (via rotations and changing the X-Y positioning of the sample) during the sputtering in order to sputter the entire surface as well as the edges of the single crystal. The cleanliness of the surface was confirmed by XPS and also via LEED by observing a clear (1x1) hexagonal diffraction pattern corresponding to the clean Pt(111) surface.

2.4.2 Preparation of BaO_x Overlayers on Pt (111) and also on TiO₂/Pt (111) Surfaces

Two different synthetic routes were used (referred as P1 and P2 in the text) in order to prepare BaO films with varying film surface coverages on the Pt(111) single crystal surface. In the first protocol (P1), Ba metal was resistively evaporated onto a N₂O₄ reactive multilayer on Pt(111) at 80 K. N₂O₄ is the dimer form of NO₂ that naturally exists in equilibrium with NO₂ at liquid nitrogen temperature. After the deposition of Ba, the sample was annealed in vacuum at 1073 K. Decomposition of N₂O₄ on Pt(111) surface at high temperatures evolves gas phase NO₂, and possibly NO, and also produces O adatoms that recombine and thermally desorb as O₂ (g) during which metallic Ba is simultaneously oxidized to BaO_x. In order to obtain BaO_x overlayers with a larger surface coverage, successive dosing and annealing procedures were repeated (with various Ba deposition durations, where necessary) the resulting films were characterized by XPS. The BaO_x coverages were estimated by the attenuation of Pt4f_{7/2} XPS signal by assuming that BaO_x distribution was uniform on the Pt(111) substrate. Typically for the thick BaO_x overlayers (10 MLE), Ba doser was heated by using a 10 A(DC) on the Ba-doser for a duration of 12 min. However, for lower coverages, < 1MLE, 60 sec deposition was sufficient (with a Ba dosing current of 10 A (DC)).

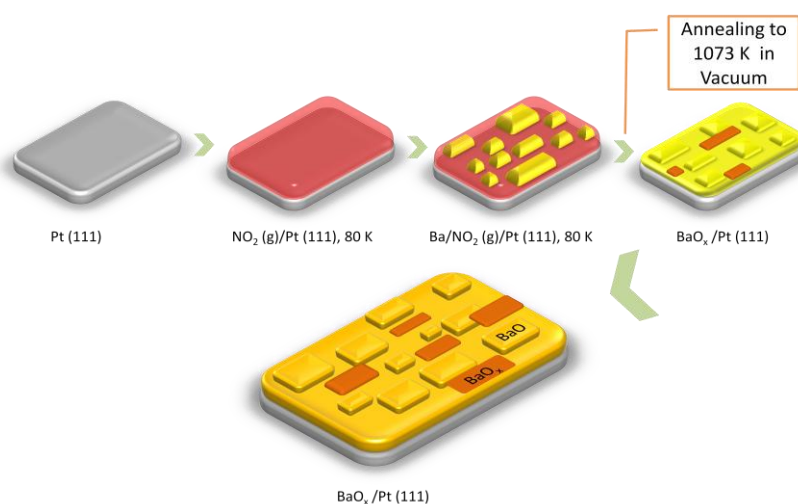


Figure 20. Sample preparation method P1 for the BaO_x films grown on Pt (111) substrate (Protocol 1).

In the second protocol (P2), Ba was evaporated onto a N_2O_4 multilayer at 80 K as described in the previous protocol. Next, the sample temperature was increased to 873 K while introducing O_2 (g) ($P_{\text{O}_2} = 1 \times 10^{-7}$ Torr) to the chamber and the sample was kept 3 min at 873 K in the presence of O_2 (g) in order to establish a complete oxidation. These Ba dosing and annealing sequences were repeated for each Ba deposition step and resulting BaO_x films were characterized by XPS.

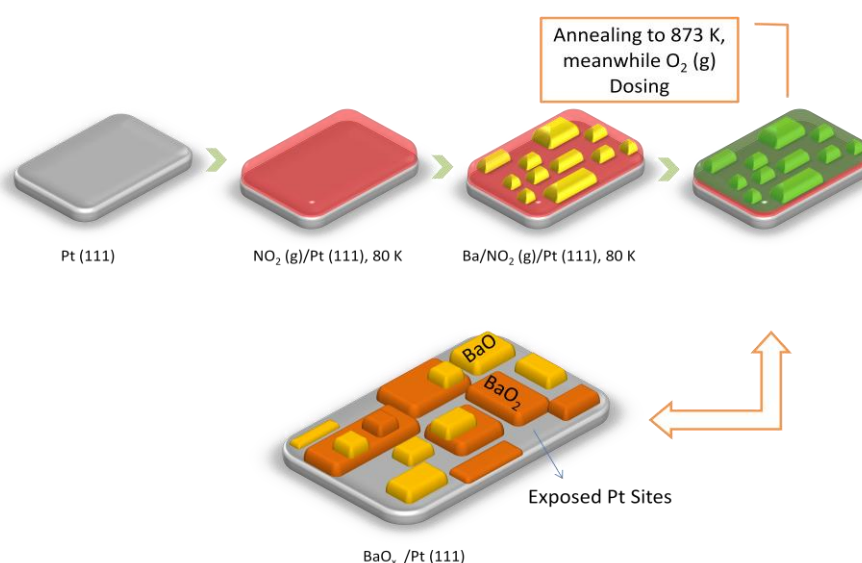


Figure 21. Sample preparation method P2 for the BaO_x films grown on Pt (111) substrate (Protocol 2).

For the preparation of BaO_x overlayers on TiO_2 / Pt(111) model system, TiO_2 phases were prepared by evaporation of Ti (at RT) on a clean, freshly sputtered and annealed Pt(111) single crystal and subsequent oxidation in O_2 (g). Thick TiO_2 films (>26ML) were prepared by dosing metallic Ti (by keeping the Ti-doser current at 8 A) for 15 min in two steps with a total dosage time of 30 min. The samples are then heated at 973 K in O_2 ($P_{\text{O}_2} = 5 \times 10^{-7}$ Torr) for 30 min. After every dosing and oxidation step, XPS and LEED analysis were performed. BaO layers were then grown on the TiO_2 /Pt (111) model system by evaporating Ba (with a Ba-doser

current of 10 A) by keeping the sample temperature at 300 K. BaO_x overlayers were achieved by heating this surface at 523 K for 30 min in O₂(P_{O₂}= 5x10⁻⁷ Torr).



Figure 22. Sample preparation method for the BaO_x films grown on TiO₂/Pt (111) model system.

3 RESULTS and DISCUSSION

3.1 BaO Films Grown on Pt (111) Substrate

3.1.1 Structure of BaO Layers on Pt (111)

The structure of the BaO_x layers as a function of the BaO coverage and the oxidation conditions were analyzed by LEED. Figure 23 presents LEED images obtained during various stages of the ordered BaO_x overlayer formation on Pt(111).

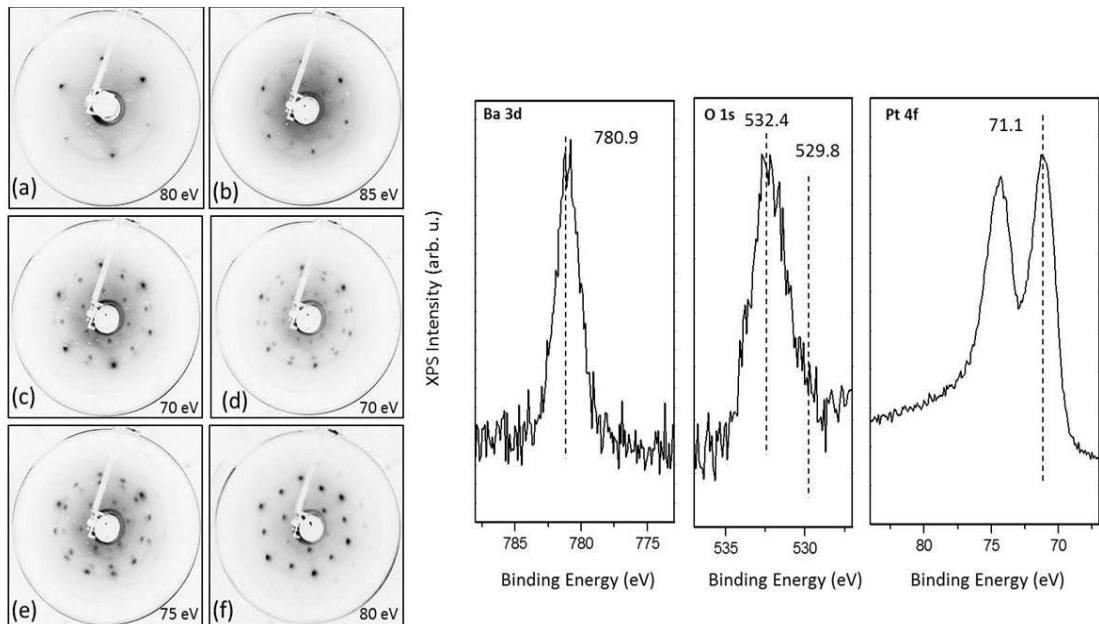


Figure 23. LEED pictures obtained during various stages of the ordered BaO_x overlayer formation on Pt(111) (see text for details). Electron beam voltage for the LEED patterns given in (a-f) is 70-85 eV, respectively. XPS spectrum corresponds to the LEED pattern given in Figure 23b.

In Figure 23a, one can see the typical hexagonal LEED pattern corresponding to a clean Pt(111) surface. Vaporization of Ba (0.3 MLE) onto the N₂O₄ multilayer overlayer on Pt(111) at liquid nitrogen temperature and heating of this surface to 300

K results in a largely disordered layer on the surface, although various additional diffuse diffraction spots start to appear, indicating a limited extent of long range order in the overlayer (Figure 23b). The $Ba_xN_xO_y$ layer formation is expected after this dosing and annealing procedure. Moreover, XPS analysis of this surface reveals the presence of nitrite/nitrate species on this surface. After annealing this surface at 1073 K in vacuum (Figure 23c), nitrate/nitrite species decompose to yield BaO_x species. The estimated BaO_x layer coverage of the surface given in Figure 23c was about 0.3 MLE. Following this annealing procedure, Figure 23c reveals an ordered structure with an intense set of diffraction spots ((2x2) and/or (1x2) unit cells) in addition to less intense spots ((2x2)R30° and/or (1x2)R30° unit cells). Subsequent annealing of the structure in Figure 23c at 1073 K and holding at that temperature for 20 min, the less intense spots ((2x2)R30° and/or (1x2)R30° unit cells) become more apparent, meanwhile the intensity of the (2x2) and/or (1x2) spots remain constant (Figure 23d). Moreover, additional annealing at 1073 K and holding for 40 min at this temperature results in an increment in the intensity of (2x2)R30° and/or (1x2)R30° unit cell spots (Figure 23e). If the annealing procedure of the sample at 1073 K is proceeded multiple times and furthermore, the sample was held at 1073 K for 1 hr, the distinguished (2x2) and/or (1x2) unit cell spots are observed, however, the spots corresponding to ((2x2)R30° and/or (1x2)R30° unit cells are completely perished.

In order to elucidate the observed LEED patterns, a schematic representation of these structures is presented in Figure 24a-f.

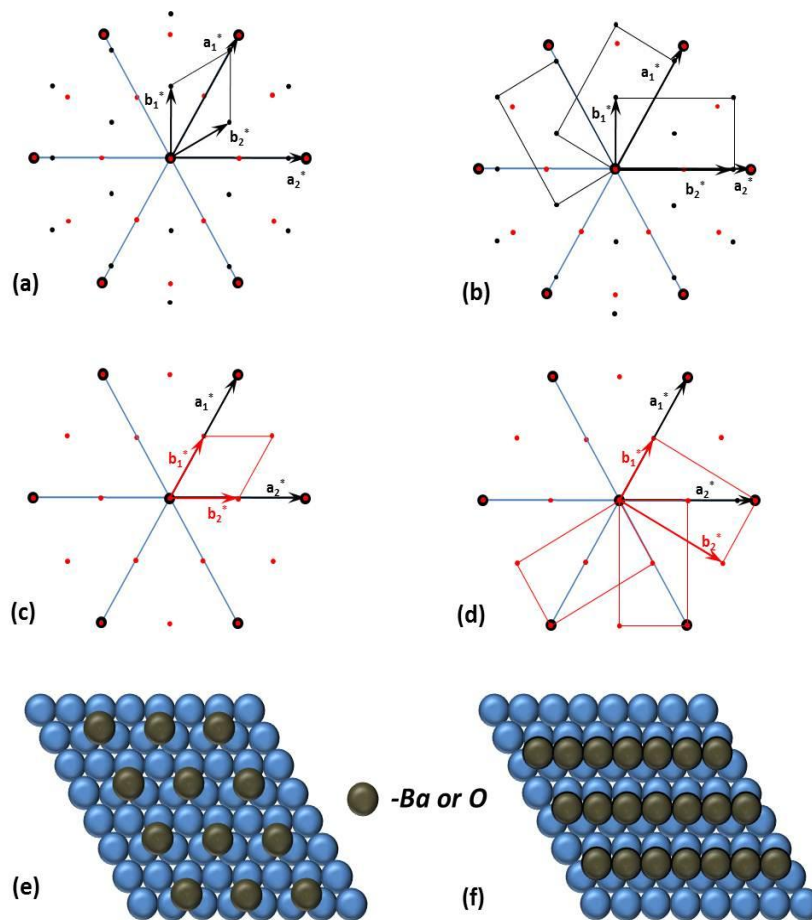


Figure 24. Schematic representations of the LEED patterns given in Figure 23. Large (black) diffraction spots correspond to the Pt(111) substrate while small (red and black) diffraction spots originate from the overlayer (a) $(2 \times 2)R30^\circ$ superstructure (b) $(1 \times 2)R30^\circ$ superstructure (c) (2×2) superstructure (d) (1×2) superstructure. Tentative real space representations of the (e) (2×2) and (f) (1×2) superstructures.

The models presented in Figure 24a,b are the visual representations of the structures observed in Figure 23c-e. The small black spots in Figure 24a correspond to $(2 \times 2)R30^\circ$ structure. However, a commonly encountered problem in LEED is the ambiguity in the interpretation of the observed diffraction spots. For instance, the small black spots in Figure 24a can also be interpreted as the existing of rectangular unit cells with $(1 \times 2)R30^\circ$ structure (Figure 24b). In addition to this, these $(2 \times 2)R30^\circ$ and $(1 \times 2)R30^\circ$ can also coexist together. As mentioned previously, as a result of the multiple successive applications of annealing procedure, the ordered

patterns observed in Figure 23b-e reconstruct as (2x2) and/or (1x2) structures (Figure 23f) and the schematic representation of these patterns are presented in Figure 24c-d. The red spots in the Figure 24c correspond to (2x2) reconstruction of BaO_x overlayers on Pt(111) substrate. Though, these red spots can also be rendered as coexisting (1x2) domains. The k-space unit cells of these 60° rotated domains are presented in Figure 24d. The possible arrangements of the structures (Ba or O terminated) in real space are depicted in Figure 24e, f. Here, (2x2)R30° and (2x2) reconstructions of BaO_x on Pt(111) are represented in Figure 24e, while other possible explanations of the same structures, (1x2)R30° and (1x2) reconstructions are represented in Figure 24f. By examining the Figure 24e,f, it can be interpreted that the (1x2) structure displays a denser or higher coverage than the (2x2) structure, (0.5 vs 2.5 MLE). However, both of these coverage values are different than the coverage value estimated by XPS (0.8 vs 3 MLE). This contradiction between the two techniques can be explained by the presence of additional disordered BaO_x clusters/-agglomerates which do not give coherent scattering in the LEED but, are readily detected by XPS. In the course of annealing in vacuum this BaO_x agglomerates are gradually spreaded on the surface finally forming (2x2) and/or (1x2) structures. Most likely, these structures are formed nearby to BaO_x agglomerates as second (or higher) layers of BaO.

The structures of the ordered BaO_x layers significantly depended on the oxide coverage and additional ordered overlayers were observed at higher coverages (e.g, 1.5 MLE). The LEED pattern obtained for a BaO_x(1.5 MLE)/Pt(111) surface is given in Figure 25a.

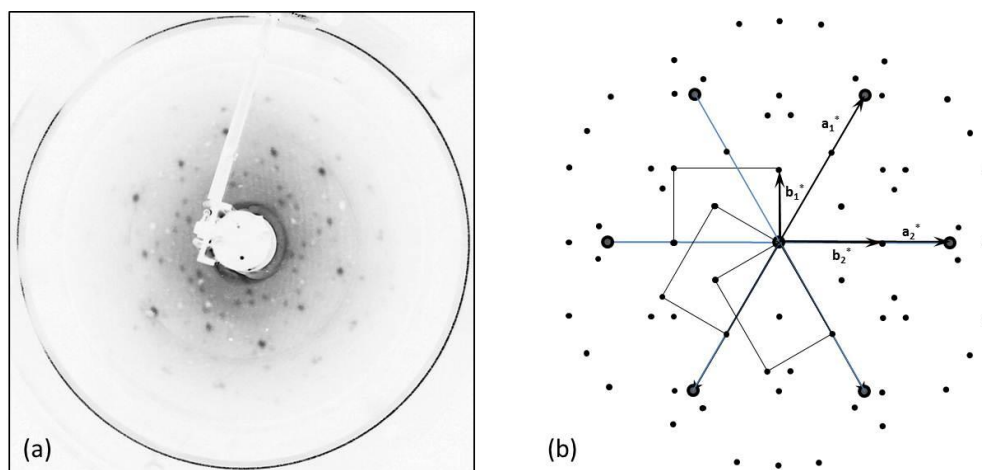


Figure 25. (a) LEED patterns for a $\text{BaO}_x(1.5 \text{ MLE})/\text{Pt}(111)$ surface and (b) the schematic representation of the corresponding diffraction spots. Big black spots correspond to the $\text{Pt}(111)$ substrate while the small black spots correspond to three different rotated domains with real-space unit cell dimensions of $3.9 \times 5.5 \text{ \AA}$.

In order to explain these more complicated LEED patterns, the superposition of three domains of a rectangular lattice should be taken into account. The schematic representation of the image is illustrated in Figure 25b which demonstrates these domains with rectangular unit cells. Each of these unit cells originates from $3.9 \times 5.5 \text{ \AA}^2$ domains in the real space. BaO has a NaCl (rock salt) structure with a space group $Fm\bar{3}m$ and a lattice parameter of $a = 5.53 \text{ \AA}$ where barium and oxygen ions have a coordination number of six. The lattice parameters of the observed $3.9 \times 5.5 \text{ \AA}^2$ rectangle structures perfectly match with the (110) surface termination of the BaO crystal. Therefore, increasing the coverage of the BaO overlayers on $\text{Pt}(111)$ substrate can result in the formation of $\text{BaO}(110)$ surfaces.

Further increasing the BaO_x coverages ($>5 \text{ MLE}$) didn't result in any diffraction spots in LEED, suggesting the formation of an amorphous BaO_x overlayer. In the literature, there are some previous efforts to investigate the structure of barium oxide layers over various single crystal substrates. Bowker et al. studied the growth of barium oxide on a $\text{Cu}(111)$ substrate and their LEED results showed that both the symmetry and unit cell size indicate the formation of BaO crystallites, or islands, oriented with the $\text{BaO}(100)$ surface parallel to the $\text{Cu}(111)$ surface.[18] The (100) surface of BaO has the lowest surface free energy [76] and therefore, it is the

thermodynamically most stable surface orientation. The formation of this surface is not surprising when the hexagonal substrate structure, in this case Cu(111) surface, has no significant influence on the BaO film formation due to a weak substrate-overlayer interaction. The structure of BaO layer on the Pt(111) substrate has also been imaged previously by STM [40,41] for a BaO overlayer coverage of approximately 3 MLE, where no clear structure was seen in LEED. In this former STM study, well-ordered regions with a spacing of 8.1 Å was observed and this value was compared with the structures of BaO(111) ($a/\sqrt{2} = 3.9$ Å) and Pt(111) ($a/\sqrt{2} = 2.8$ Å). BaO(111) is a polar surface with an expected oxygen and barium spacing in each layer of 3.9 Å for an unconstructed surface [41] and they measure the surface of the BaO layer as twice the lattice spacing of BaO(111) bulk termination. As a conclusion, the author elucidates this double times lattice mismatch between their calculated lattice parameter for BaO 8.1 Å and BaO(111) surface lattice parameter 3.9 Å by a (2x2) reconstruction of BaO(111) surface where interatomic surface distances are double of that expected for BaO(111). However, none of these studies revealed the existence of BaO(110) surface orientation and (2x2)/(1x2) BaO surface domains on Pt(111) substrate as in our studies.

3.1.2 NO₂ Adsorption and Storage on Thick (10 MLE)

BaO_x Overlayers

In order to understand the NO_x trapping ability of BaO in a BaO/Pt(111) model catalyst, NO₂ adsorption experiments were performed on BaO_x(10 MLE)/Pt(111). In order to eliminate the effect of the interaction between BaO_x and underlying Pt(111) substrate on the NO_x chemistry of the BaO_x film, a thick BaO_x film was prepared by protocol 1, where the thick BaO_x film has a good dispersion on the Pt(111) substrate, preventing the exposure of Pt(111) sites. The thickness of the prepared BaO_x layer estimated from the attenuation of Pt4f_{7/2} signal was 10 MLE. Without any oxidation procedure, metallic Ba layer grown on the Pt(111) surface has a core level Ba3d_{5/2} binding energy (BE) of 780.9 eV. When the oxidation of metallic Ba phase took place, the Ba3d_{5/2} signal shifted to 779.3-779.8 eV, depending on the

BaO_x coverage. The negative BE shift for the oxidation of the Ba metal is a well known phenomenon and was observed previously in the literature.[46,47] Figure 26 presents N1s and O1s XP spectra recorded for the freshly prepared sample, after 3600 L (P_{NO₂}=10⁻⁶ Torr x 1hr) NO₂ exposure, and subsequent stepwise heating in vacuum at the given temperatures.

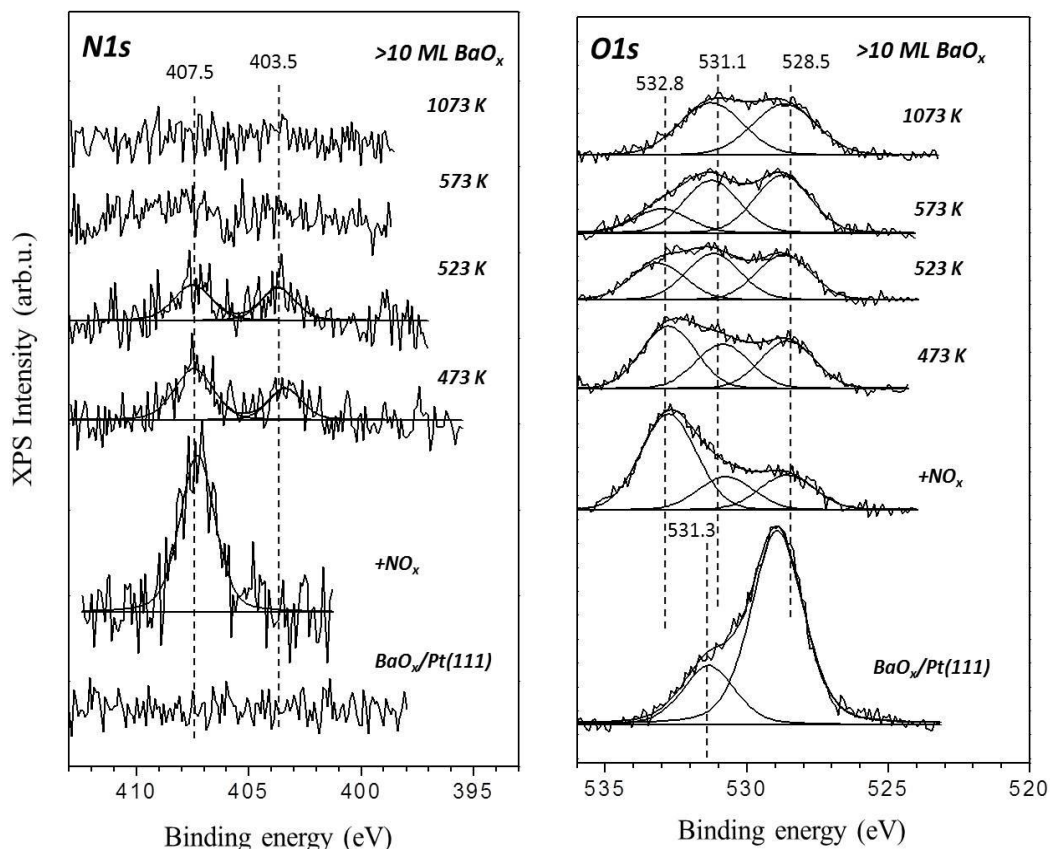
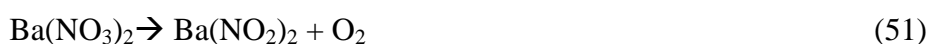


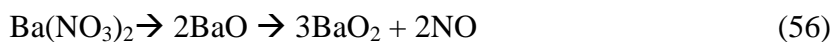
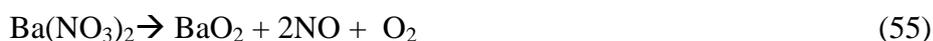
Figure 26. XPS core level spectra, N1s and O1s for a thick BaO_x(10 MLE) /Pt(111) exposed to 3600 L NO₂ at 323 K and subsequently annealed to the indicated temperatures in vacuum.

Figure 26 reveals the peak at 407.5 eV which is consistent with nitrate-like adsorbed species.[43] Under these conditions, nitrite species (NO₂⁻) which have a characteristic peak at 403.5 eV is not observed. In the previous investigations of BaO_x films on Pt(111) [43, 45] it has been shown that during the initial stages of NO₂ uptake, nitrate and nitrite species form simultaneously. However, after the saturation of the surface with an extensive exposure of NO₂(g), all of the nitrite species

are converted to nitrates. Thus the spectrum labeled as “+NO_x” in Figure 26 corresponds to a surface that is saturated with NO_x. After heating the saturated surface at 473 K, the intensity of the nitrate N1s peak in Figure 26 decreases and the nitrite peak starts to appear. The minor decreasing of the intensities are observed after subsequent heating at 523 K. The appearance of nitrite in the spectra points out that thermal decomposition of nitrate proceeds through the formation of nitrite. Below is a suggested mechanism for the “nitrite assisted” nitrate decomposition process:



However, the route for the direct nitrate decomposition cannot also be excluded.



After annealing at 623 K, N1s signal related with the nitrate and nitrite species disappear. Although the N1s signals vanish after annealing at 623 K, not all of the NO_x species desorb from the surface as verified by the TPD experiments discussed below. Thus at this temperature NO_x concentration on the surface is simply below the detection limit of the XPS energy analyzer.

For the same series of NO₂ adsorption experiments, O1s region was also monitored in XPS together with the N1s region (Figure 26). O1s region of the freshly prepared BaO_x layer, presents two major features at 528.5 eV and a shoulder at 531.3 eV. The 528.5 eV feature is associated with BaO [42, 43, 45] species while the shoulder at 531.3 eV can be attributed to BaO₂ species.[77] After the saturation of the surface with NO₂ at RT, a new intense peak appears at 532.8 eV, which can be associated with Ba(NO₃)₂ and Ba(NO₂)₂ species, and moreover, the peak corresponding to BaO₂ species shift to lower BE, 531.1 eV. By considering the corresponding N1s spectra, it can be argued that the 532.8 eV signal is due to mostly

nitrate-like species. After annealing at 473 K, the intensity of the nitrate-related O1s peak is decreased. The heating at 523 K demonstrates no significant changes while the annealing at 573 K leads to a significant decrease in the nitrate-related O1s peak intensity indicating the decomposition and desorption of the adsorbed NO_x species. In addition, the relative intensity of the BaO₂ feature (c.a. 531.1 eV) in the O1s spectrum also increases during the annealing process suggesting that the nitrate decomposition is accompanied by the formation of peroxide species which can exist on the surface even after annealing at 1073 K. It is worth mentioning that analogous experiments were performed for thinner BaO_x overlayers ($\theta_{\text{BaO}_x} = 5$ MLE) and it was found that the NO₂ behavior of the BaO_x(5 MLE)/Pt(111) surface is rather similar to that of the thicker films (i.e. $\theta_{\text{BaO}_x} = 10$ MLE). This suggests that above a certain BaO_x film thickness, the NO₂ adsorption properties of the BaO_x converge to the bulk-like behavior.

It is crucial to elucidate the interaction between NO₂ and BaO_x overlayers in more detail. In order to achieve this, TPD experiments were performed after NO₂ adsorption on the selected model catalysts which provide additional insight regarding the adsorbed NO_x species. Figure 27 demonstrates TPD spectra obtained after 900 L ($P_{\text{NO}_2} = 5 \times 10^{-7}$ Torr x 30 min) NO₂ exposure (i.e. near saturation coverage) on the BaO_x(10 MLE)/Pt(111) surface with a thick BaO_x overlayer prepared by using protocol 1.

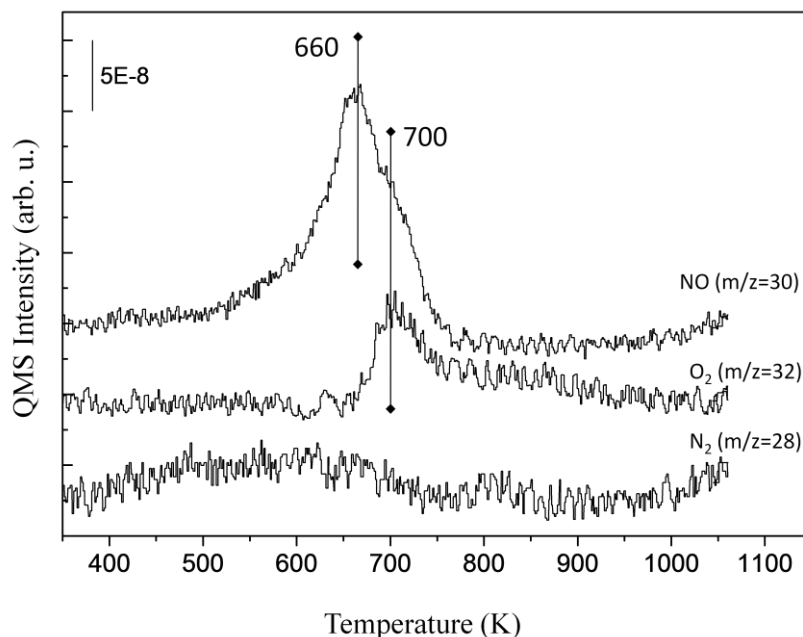


Figure 27. TPD spectra for NO ($m/z = 30$), O_2 ($m/z = 32$), and N_2/CO ($m/z = 28$) channels obtained after exposure of $BaO_x(10 \text{ MLE})/Pt(111)$ surface to 900 L NO_2 at 323 K.

In the NO ($m/z = 30$) TPD profile in Figure 27, one can see two distinguishable desorption features at 660 K and 700 K with a low temperature broad shoulder at ~ 570 K. The N_2 desorption can be considered to be rather minor in Figure 27 except a very weak and a broad desorption band within 400-700 K. The low temperature NO desorption shoulder at ~ 570 K might be associated with the decomposition of nitrates from small $Ba(NO_3)_2$ clusters which are well-dispersed on the $Pt(111)$ surface, as suggested in previous studies.[78] The main NO desorption peaks appearing within 600-700 K demonstrate two pathways of $Ba(NO_3)_2$ decomposition: nitrate, decomposition at 660 K proceeds with the evolution of NO without O_2 , as outlined in the reactions (52), (53), and (56) given above. In this decomposition pathway, oxygen originating from nitrate decomposition diffuses into the subsurface and/or oxidizes the BaO domains into BaO_2 . When the BaO_2 surface coverage reaches a limiting value, nitrate decomposition goes through a different pathway involving $NO + O_2$ evolution with a desorption maximum at 700 K. The

second nitrate decomposition pathway can be envisaged using the reactions evolution (51), (54), and (55) given above. The broad O₂ desorption signal appearing at 800-900 K can be associated with the decomposition of BaO₂ species forming BaO.

In our TPD experiments, NO₂ (m/z= 46) desorption was not detected, unlike former studies in the literature where a minor NO₂ desorption was observed. Detection of NO₂ with a QMS using electron impact ionization is known to be problematic due to the facile fragmentation of the NO₂(g) radical under electron bombardment yielding NO(g) + O(g). Thus, pure NO₂ gas reveals to major signals at m/z=30 and m/z= 46 in a typical mass spectrum where the intensity of the m/z=30 signal is about three or four times more intense than that of the m/z=46 (i.e. the molecular ion) Thus the lack of the m/z=46 signal in the current data is most likely associated with the experimental design of the current TPD setup and the QMS shield covering the ionization compartment which provides a rather large dead volume for incoming NO₂ molecules where they can react with the walls and decompose, before they reach the ionization compartment

Figure 27 also shows a weak and a broad N₂O/ CO₂ (m/z= 44) signal (data not shown) located at 800 K. This peak is most likely due to background CO or CO₂ adsorption on the BaO_x/Pt(111) and the formation of Ba(CO₃)₂ species which decompose at c.a. 800 K. Atomically clean (and hence reactive) alkaline earth oxide surfaces are known to have a very large affinity towards carbonate formation which can even occur at pressures as low as 5 x 10⁻¹⁰ Torr. In order to confirm this assignment, we have performed a control experiment in which a “blank” TPD run was executed on a clean surface without introducing any additional adsorbates. This control experiment revealed an identical m/z=44 desorption feature located at 800 K, supporting the argument that this peak originates from background CO/CO₂ adsorption and not from N₂O.

3.1.3 Effect of the BaO_x Preparation Protocol on the Surface Morphology and Chemistry

We also employed different oxidation protocols in order to investigate the influence of the preparation protocol on the structure and the reactivity of the

BaO_x/Pt(111) surfaces. Therefore, we focused on the synthesis of the BaO_x(10 MLE)/Pt(111) model catalysts by using a different oxidation protocol which is described as protocol 2 above. BaO_x(10 MLE)/Pt(111) was then saturated with 900 L of NO₂ (P_{NO₂} = 5 × 10⁻⁷ Torr × 30 min at 300 K). XPS analysis revealed that nitrates are predominantly formed on the surface with a minor contribution from nitrite species (NO₂⁻/NO₃⁻ N1s integrated intensity ratio < 0.15). TPD experiments were also carried out after the saturation of this surface with NO₂. Selected desorption channels such as NO (m/z = 30), N₂ or CO (m/z = 28), and O₂ (m/z = 32) are represented in Figure 28a. Ba3d, Pt4f, O1s regions were also calculated with XPS for BaO_x films grown via protocol 2. These XPS data had the identical characteristic features to that of films prepared by protocol 1.

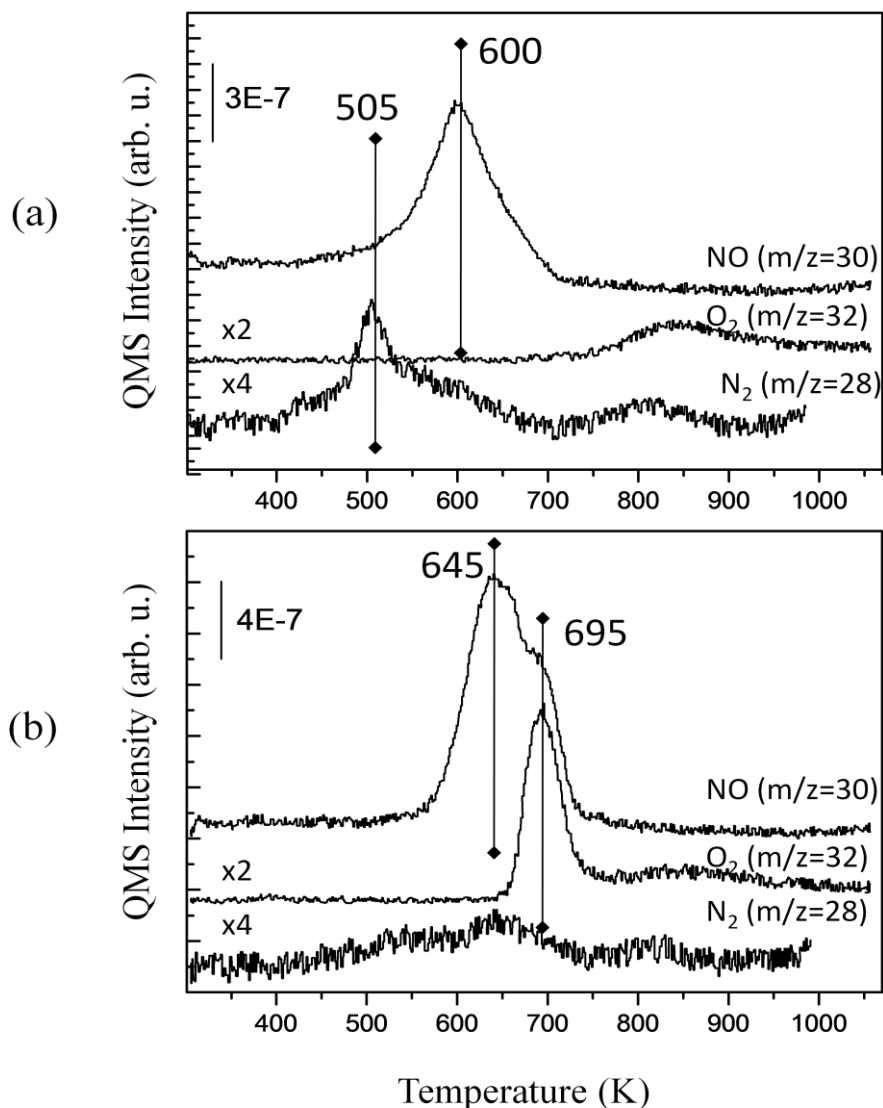


Figure 28.(a) TPD spectra for the NO ($m/z=30$), O₂ ($m/z=32$), and N₂/CO ($m/z=28$) desorption channels obtained after the exposure of a BaO_x(10 MLE)/Pt(111) surface to 900 L NO₂ at 323 K; where the BaO_x film was prepared using protocol 2(b) A similar TPD experiment performed on a BaO_x(10 MLE)/Pt(111) surface which was initially exposed to subsequent multiple cycles of NO₂ adsorption/saturation and annealing at 1073 K.

In Figure 28a, the major NO desorption signal appears as an asymmetric peak at 600 K with a tail extending towards higher temperatures. This main NO desorption peak is not accompanied by O₂ evolution, suggesting that the generated oxygen

during nitrate decomposition is used in the BaO_2 formation. It is worth mentioning that the major NO desorption maximum (600 K) appears at a temperature much lower than that of the surface prepared by protocol 1 (660-700 K). The most striking aspect of Figure 28a is the presence of a well-defined N_2 desorption signal appearing at 505 K with a high-temperature shoulder at 600 K. It is well known that [43-50] metal oxide surfaces (particularly BaO or BaO_2) can readily decompose to NO_2 , NO_2^- , NO_3^- and form $\text{NO}(\text{ad}) + \text{O}(\text{ad})$ species. However these alkaline earth oxide surfaces are incapable of activating NO to form $\text{N}(\text{ad})$ and $\text{O}(\text{ad})$. Thus, the activation of the N-O linkages are typically achieved via Pt-group precious metal sites such as Pt, Pd or Rh in NO_x reduction processes. Along these lines, observation of a N_2 evolution signal in the TPD experiment implies the existence of exposed (open) Pt(111) sites on the BaO_x (10 MLE)/Pt(111) surface prepared by protocol 2, catalytically activate adsorbed NO_x species, generating atomic $\text{N}(\text{ad})$ species that recombinatively desorb as N_2 . Desorption and dissociation of NO on supported Pt particles [79] and on Pt single crystal surfaces [80] were extensively studied in the literature. The generation of a N_2 desorption signal upon NO adsorption on Pt(111) was ascribed to the presence of defect sites on the Pt(111) surface which activate the N-O bond rupture and yield a N_2 desorption signal at 475 K [80] with a broad tail at 500-750 K. It should be noted that NO does not dissociate on a perfect (i.e. defect-free) Pt(111) single crystal [81] and the dissociation products can only be observed in the presence of point or extended defects (e.g. line defects, steps, edges etc.) on the Pt(111) single crystal. The presence of exposed Pt sites can also clarify the shifting of the major NO desorption maximum in Figure 28a compared to the one in Figure 27 towards lower temperatures (i.e. 600 K vs. 660-700 K). It is apparent that the exposed Pt sites that are located at the periphery of the BaO_x sites assist the NO_x decomposition possibly by facilitating the oxygen surface diffusion away from the $\text{Ba}(\text{NO}_3)_2$ sites towards BaO sites catalyzing the formation of BaO_2 . These exposed Pt(111) sites, are formed during the heating in oxygen in protocol 2, most probably originated as a result of BaO_2 formation. BaO_2 has a different oxide density and a different crystal structure than BaO as well as different lattice mismatch between Pt(111) substrate which result in alterations in the strength of the interactions between the substrate and the overlayer leading to different dispersion behavior for the overlayer. Furthermore, the high-temperature $m/z=28$ desorption

feature appearing at 800 K most likely originates from background CO adsorption since such desorption feature exists for controlled “blank” TPD experiments performed on a fresh and clean surface without introducing any additional adsorbates prior to the control TPD runs.

It is also worth mentioning that this thick BaO_x overlayer revealing exposed Pt(111) sites can be “cured” after multiple NO₂ adsorption-desorption cycles. Figure 28b demonstrates of such a curing where a BaO_x(10 MLE)/Pt(111) surface prepared by protocol 2 was treated with 7 subsequent cycles of nitration-annealing and then used in a regular NO₂ TPD experiment. Figure 28b indicates that the nitrate decomposition occurs on this surface in the same manner as for the first protocol. It can be observed that there is no significant N₂ desorption and the nitrate decomposition occurs in two pathways as in Figure 27. If this “cured” surface is annealed at 873 K in 10⁻⁷ Torr of oxygen, the N₂ desorption in the TPD spectra can be observed again at ~480 K. In conclusion, it turns out that this surface morphology change involving “cracking/curing” of the BaO_x overlayer is a reversible process which is closely related to the stoichiometry of the BaO_x overlayer and the interaction between the overlayer and the Pt(111) substrate

3.1.4 NO₂ Adsorption on Thin BaO_x Layers

The interaction between NO₂ and a thinner BaO_x(~2.5 MLE) /Pt(111) surface prepared via protocol 1 was also investigated upon room temperature adsorption of 360 L NO₂(P_{NO₂}= 1x10⁻⁷ Torr x 1 hr) onto this surface. The results showed the presence of only nitrate species after saturation with NO₂ in XPS (i.e. without nitrate formation analogous to thick (10 MLE) of BaO_x overlayers. According to N1s spectra, the thermal decomposition of nitrates also occurred together with the nitrite formation with a total disappearance of N1s spectra of nitrate and nitrite species after heating to 623 K. The O1s spectra monitored after nitration and subsequent thermal decomposition are presented in Figure 29.

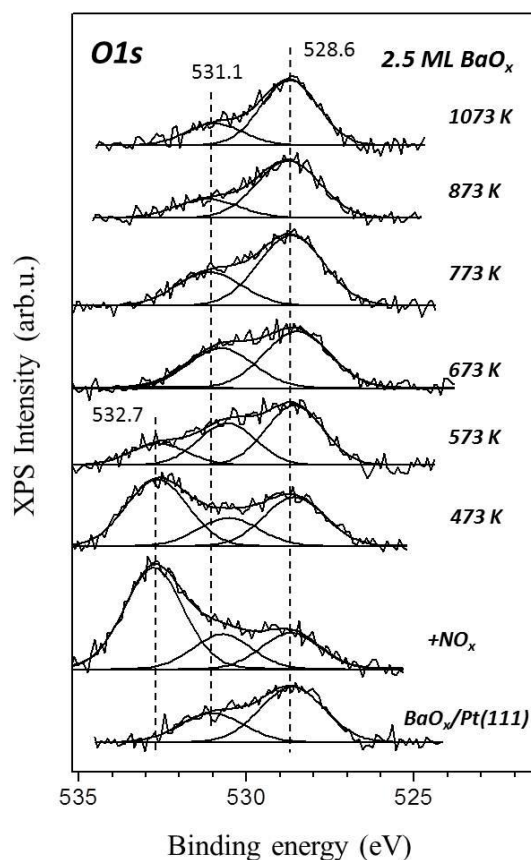


Figure 29. O1s XPS core level spectra for BaO_x(~2.5 MLE) /Pt(111) surface exposed to 360 L NO₂ at 323 K and subsequent annealing to the indicated temperatures.

As in the case of thick BaO_x overlayers, clean BaO_x(~2.5 MLE)/Pt(111) surface reveals, two major O1s peaks at 528.6 and 531.1 eV associated with the BaO and BaO₂ species, respectively. After the NO₂ adsorption procedure, the O1s peak attributed to the nitrate species at 532.7 eV appears. The intensity of the nitrate peak decreases after the subsequent heating at 473 K and 623 K in vacuum environment and eventually disappears after heating at 673 K. These results are in consistent with the results that are observed for the thick (10 MLE) BaO_x overlayers. However, the behavior of the O1s signal corresponding to BaO₂ species at 530.6- 531.1 eV shows an important dissimilarity with respect to 1073 K spectrum in Figure 26. It is apparent that the BaO₂ intensity is much less in Figure 29 after 1073 K treatment suggesting a relatively less stable BaO₂ structure for the thinner films. The variation

of the BaO₂ signal in O1s spectra as a function of the thermal treatment temperature for thin (2.5 MLE) and thick (10 MLE) BaO_x films are given in Figure 30.

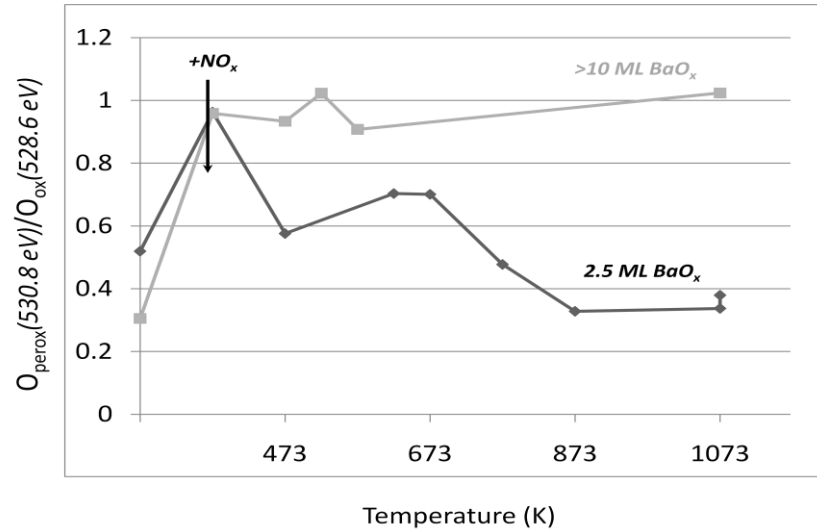


Figure 30. The graphs of O1s peaks intensity ratios O_{perox} (530.8 eV) to O_{ox} (528.6 eV) for 10 ML (grey squares) and 2.5 ML (black circles) BaO_x films measured after nitration and subsequent heating.

In the case of thick BaO_x overlayers (10 MLE), after NO₂ adsorption peroxide signal increases the O_{perox}/O_{ox} atomic ratio to c.a. 1. This value stays rather unchanged throughout the whole thermal window for the thick films. The nitration of the thin overlayers also increases the O_{perox}/O_{ox} ratio to 1, but during the nitrate decomposition process within 473-873 K, this ratio falls to 0.3. The peroxide phase is not decomposed completely even after annealing at 1073 K which indicates the presence of some stable BaO₂ domains (possibly in the form of big agglomerates). The lack of BaO₂ decomposition on thick BaO_x overlayers can be attributed to the deficiency of exposed Pt sites for the thick films prepared via protocol 1. Apparently, Pt sites can catalyze the peroxide decomposition when it is in physical contact with the small BaO_x domains.

It is also worth mentioning that the observed BE variation of the O1s peroxide peak in Figure 26 and 29 might be associated with the formation/decomposition of some BaCO₃ and/or Ba(OH)₂ species which could be formed as a result of BaO_x interaction with CO₂ or H₂O from the residual

contamination in vacuum at 5×10^{-10} Torr. We checked the existence of carbonate type species with XPS, since C1s has a very low sensitivity and is hard to be detected, we couldn't observe via XPS. The O1s peak of BaCO_3 and Ba(OH)_2 are expected to be found at 531.5 eV [82] and 531.0-531.4 eV, respectively [83], which can overlap and shift the observed peroxide peak higher BE. Another explanation of the peroxide BE variation is the differential charging differences between the oxide and peroxide domains as a result of morphology changes.

The TPD experiments performed after the saturation of BaO_x (~2.5 MLE) /Pt(111) surface at RT are given in Figure 31. General characteristics of the NO desorption channel is rather similar to that of the thicker films. On the other hand, two important differences exist in the TPD data for BaO_x (~2.5 MLE) /Pt(111).

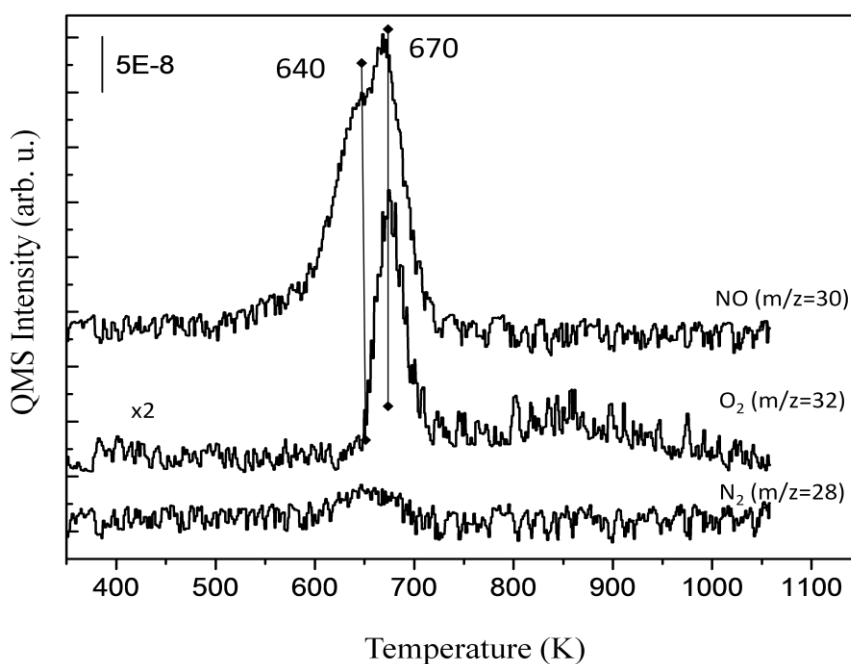


Figure 31. TPD spectra for NO (30 amu), O_2 (32 amu), and N_2/CO (28 amu) obtained after exposure of BaO_x (~2.5 MLE) /Pt(111) to 900 L NO_2 at 323 K.

Firstly the prominent NO desorption maxima are shifted to lower temperatures in Figure 31 compared to that of Figure 27 (thick films prepared via protocol 1). Secondly, although some N_2 desorption signal exists with a

desorption maximum at 650 K; its intensity is much smaller than that of Figure 28 (thick films prepared via protocol 2).

TPD experiment of the nitrated BaO_x (~2.5 MLE)/Pt(111) surface after preheating in vacuum at 623 K was also performed as shown in Figure 32.

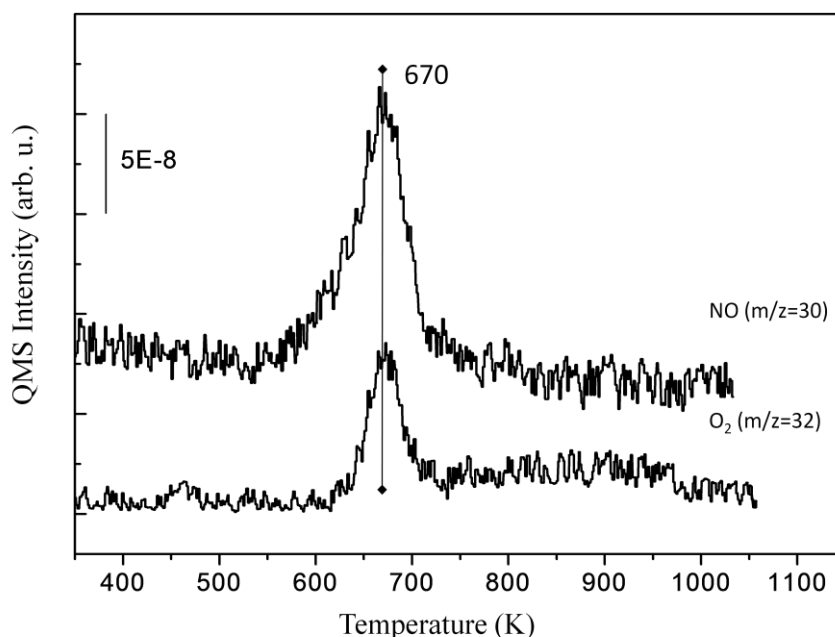


Figure 32. TPD spectra for NO (30 amu), O₂ (32 amu), obtained after exposure of BaO_x (~2.5 MLE) /Pt(111) to 900 L NO₂ ($P_{\text{NO}_2} = 5 \times 10^{-7}$ Torr x 30 min) at 323 K then preheated to 623 K before TPD.

As it was verified by XPS, after preheating at 623 K, nitrate is partially decomposed and coexisting nitrate and nitrite species are formed. After this preheating procedure, only the second stage of the nitrate/nitrite decomposition was observed at 670 K (Figure 32). As discussed above, the second stage of the nitrate decomposition occurs after almost all of the BaO is converted into BaO₂. Experimentally, the second stage of the nitrate decomposition process was isolated from the first stage by annealing at 623 K of pre-nitrated surface in order to demonstrate the stability of the nitrate/nitrite decomposition during the second stage. This later process can be considered as nitrate/nitrite decomposition on the BaO₂ surface since at this temperature, BaO₂ formation is favored. Therefore, it can be

concluded that nitrate or nitrite species on the BaO₂ surface exhibits a higher stability than on BaO surface.

There is little known about the relative thermal stability of the nitrate species formed on the top surface of small BaO nanoclusters and nitrate species that are formed in the subsurface (bulk) of larger BaO nanoparticles. Therefore, the NO₂TPD experiments were performed for a large variety of BaO_x surface coverages where at low coverages BaO species possibly exist mostly as 2D islands and/or small clusters while at larger coverages they form multilayer films and/or 3D large nanoparticles. These BaO_x-coverage dependent m/z=30 desorption data is given in Figure 33. Note that all of the surfaces were prepared via protocol 1.

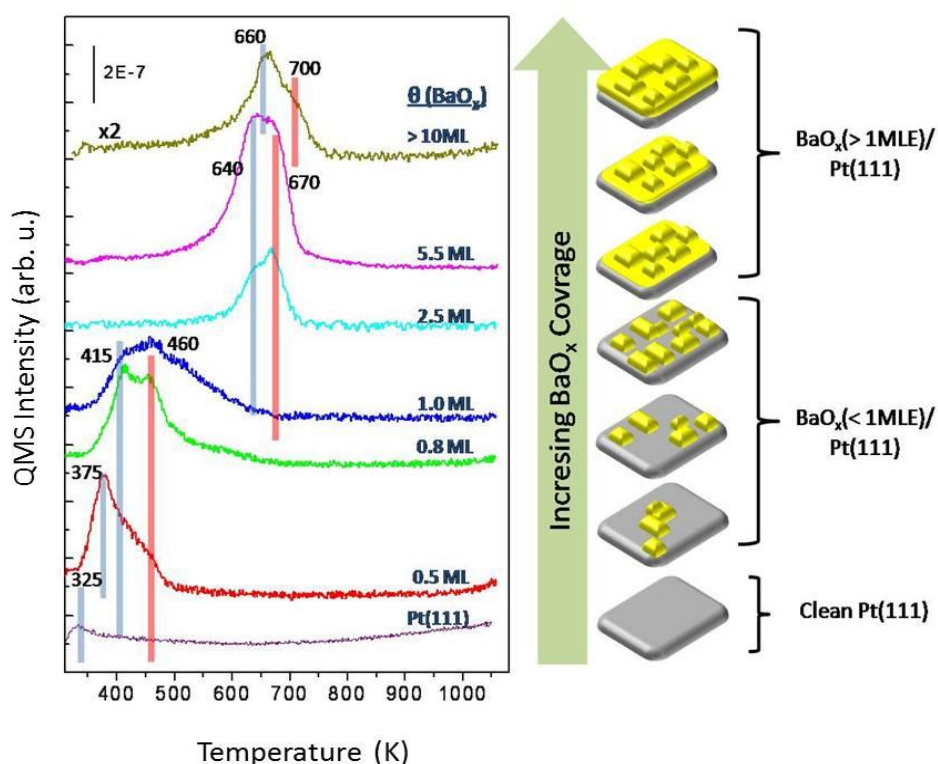


Figure 33. TPD spectra for NO (30 amu) desorption obtained after exposure of BaO_x/Pt(111) surfaces with varying BaO_x coverages (0.5 MLE < θ_{BaO_x} < 10 MLE) to 900 L NO₂ ($P_{\text{NO}_2} = 5 \times 10^{-7}$ Torr x 30 min) at 323 K.

For the coverages 2.5 MLE and higher, two stages of NO desorption was observed as discussed previously. For the lower coverages of 1 MLE and 0.8 MLE,

the NO desorption (TPD curves presented in Figure 33) proceeds via two main peaks at significantly lower temperatures (at 415 and 460 K, respectively). In the case of 1.0 MLE, the tail of NO desorption at 500-650 K is observed as well, and this tail is less pronounced in the case of 0.8 MLE. For these coverages, the open Pt regions are expected to be present on the surface, and this open Pt regions have a strong influence on the mechanism of the nitrate/nitrite decomposition by decreasing the decomposition temperature. The NO TPD profile monitored after nitration of 0.5 MLE BaO_x layer (the lowest spectrum in Figure33) demonstrates the intense peak at 375 K as well as less pronounced overlapping peaks at 415 and 460 K. In previous studies of NO adsorption on the clean Pt(111) surface [84], TPD experiments demonstrate the NO desorption as a convoluted peak at 350-380 K. In our case, for a very low coverage of BaO_x (0.5 MLE), the desorbing NO species at 375 K are mostly related to NO accumulated on Pt surface during NO₂adsorption.

3.2 TiO_x Films Grown on Pt (111)

Atomically ordered TiO_x/Pt(111) surfaces were prepared with various TiO₂ surface coverages. Such systems werethoroughlystudied by Granozzi and Sedona et al.[54] Thus, the well-known TiO₂ film growth recipe developed by Granozzi et al. was adopted in the current work to grow titania films on Pt(111). TiO₂ film growth procedure involves reactive evaporation of Ti onto clean, freshly sputtered and annealed Pt(111) at room temperature. The samples are then heated at 973 K in oxygen ($P_{O_2}=5 \times 10^{-7}$ Torr) in order to completely oxidize the overlayer. Finally, the samples are cooled to RT and then characterized by XPS and LEED. Figure 34 shows the Ti 2p photoemission spectra and O 1s spectra of the prepared TiO_x overlayers on Pt(111) substrate.

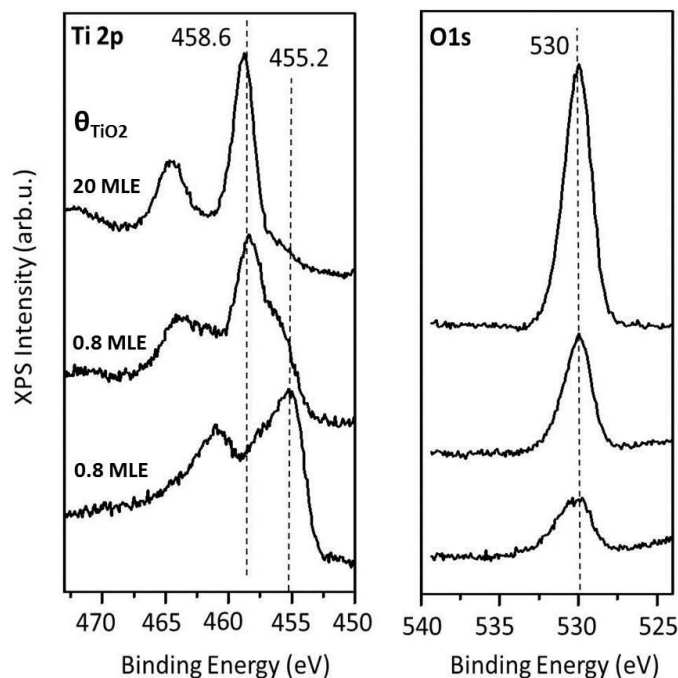


Figure 34. XPS spectra of TiO_x phases depending on the oxidation conditions in the Ti2p and O1s core level region (see text for details).

The TiO_x surface phases show two chemically shifted $\text{Ti}2p_{3/2}$ components with well-resolved BEs. In the Ti2p spectra given in Figure 34, the lower BE component, centered at 455.2 eV can be assigned to Ti^{+3} oxidation state, while, the higher binding energy component 458.6 eV can be attributed to the Ti^{+4} oxidation state. The bottommost spectra given in the Ti2p and O1s series of Figure 34 were obtained after Ti dosing as metallic (without additional exposure to oxygen) at RT ($\text{TiO}_x(0.8 \text{ MLE})/\text{Pt}(111)$). These films mostly consist of Ti^{+3} species which are due to the partial oxidation of the reactive Ti overlayer by background oxidants such as H_2O , O_2 , CO_2 etc. The middle spectra are obtained after the oxidation of the same $\text{TiO}_x(0.8 \text{ MLE})/\text{Pt}(111)$ sample at 823 K in $\text{O}_2(\text{g})$. It can be seen that even this relatively high temperature is not enough for the complete oxidation of TiO_x phases. However, further dosing of Ti ($\text{TiO}_x(20 \text{ MLE})/\text{Pt}(111)$) and oxidation at 973 K in $\text{O}_2(\text{g})$, the topmost spectra were obtained which show that almost all of the Ti^{+3} species were oxidized and converted into Ti^{+4} species which is evident from the

sharp and intense 458.6 eV feature . The large BE change observed for the Ti2p core level is not observed for the O1s BE values. However, as the TiO_x phase gets oxidized, the intensity of the O1s signal centered at 530 eV, increases. It should be noted that it was previously reported in the literature that the O1s BE for TiO₂ is 530.3 eV [85] which is consistent with the results given in Figure 34.

For the oxidized TiO_x structures, the different TiO_x surface coverage values yield a diverse set of LEED patterns as previously discussed by Sedona and Granozzi et al, [54], [86], [87] By careful optimization of the preparative parameters, some of these ordered TiO_x films on Pt(111) were reproduced in the current work and verified by LEED. Figure 35 shows some of the LEED patterns corresponding to different ordered TiO_x/Pt(111) surfaces (all LEED patterns were obtained with an electron energy of 85 eV).

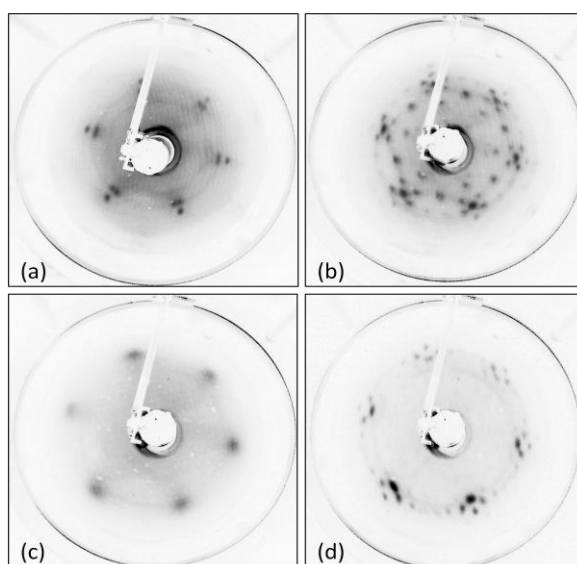


Figure 35. LEED patterns for ordered TiO_x/Pt(111) surfaces with varying θ_{TiO_x} (see text for details) .

The first picture, in the Figure 35a, was obtained after Ti dosing (~0.8 ML) onto Pt (111) at room temperature and oxidation at 823 K in 5×10^{-7} Torr O₂(g). In this case, the diffraction spots in the LEED pattern are still fuzzy indicating that the TiO_x structure is not fully crystalline. However, after heating to 1073 K in UHV, a different phase (labeled as Zigzag-Like TiO_x phases, *z-TiO_x* [54]) was obtained as

shown in Figure 35b. The z-phase can be assigned to an incommensurate superstructure with respect to the Pt (111) substrate with a rectangular unit cell of about $(6.8 \pm 0.1) \times (8.6 \pm 0.1) \text{ \AA}^2$. [86] With the help of former STM studies in the literature, this z-TiO_x was found out to be the combination of an O-Ti bilayer, exposing an oxygen termination. [54]

Pt(111) single crystal was then sputtered and a freshly prepared TiO_x film was obtained with an increased coverage. At $\theta_{\text{TiO}_x} = \sim 1.2$ MLE and after oxidizing the sample at 823 K in an oxygen pressure of 5×10^{-7} Torr, the LEED pattern in Figure 35c was obtained. This figure also represents a fuzzy diffraction pattern with a hexagonal structure which is very similar to the Pt(111) substrate. Heating at 1073 K in UHV resulted in a more ordered TiO_x phase as shown in Figure 35d, which is called the Wagon-Wheel-Like, w-TiO_x, structure in the literature. [54] A detailed analysis of this phase demonstrated that this complex diffraction pattern corresponded to a $(\sqrt{43} \times \sqrt{43})R 7.6^\circ$ structure with a unit vector of 18.2 \AA . [54]

3.3 BaO Films on TiO₂/Pt (111) Model System

In order to study the effect of TiO₂ addition on the catalytic activity of the BaO/ Pt(111) type of model catalyst systems, BaO films were grown on the thick TiO₂ layers (26 MLE) and the chemical reactivity of the prepared BaO/TiO_x/Pt (111) model system towards NO₂ and CO₂ has been demonstrated. The reason for the preparation of thick TiO₂ films was to eliminate the effect of the interaction between TiO₂ and the underlying Pt(111) substrate on the NO_x chemistry of the BaO films grown on TiO₂ overlayers. The XPS technique was employed to examine the surface states of resultant samples and the surface crystallinity was studied by LEED. Finally, TPD experiments were conducted in order to analyze the reactivity of this model system towards NO₂ and CO₂.

3.3.1 XPS Analysis of BaO/ TiO₂/ Pt (111) Model Catalysts

The main peaks in the XPS scan of the BaO/ TiO₂/ Pt (111) sample are shown in Figure 36.

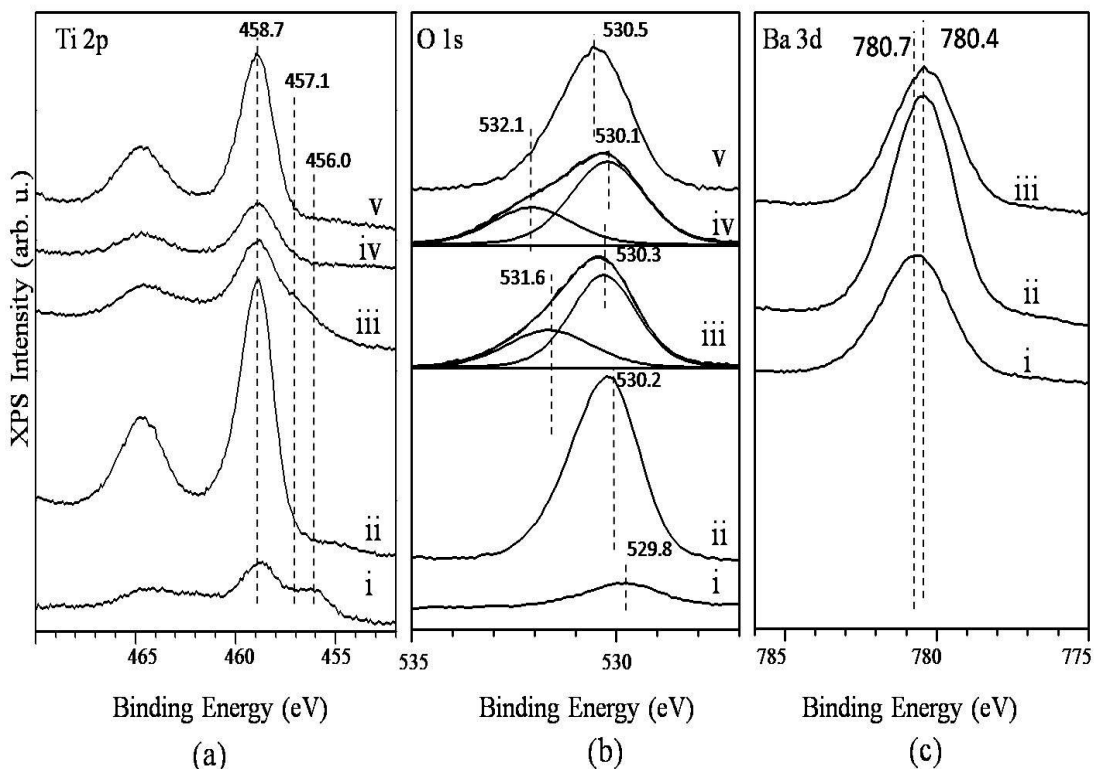


Figure 36. XPS data corresponding to the (a) Ti 2p, (b) O 1s and (c) Ba 3d_{5/2} regions obtained for (i) TiO_x(1.4 MLE)/Pt(111), (ii) TiO₂(26MLE)/Pt(111), (iii) as deposited Ba(3MLE)/TiO₂(26 MLE)/Pt(111) surface prior to oxidation, (iv) BaO_x(6 MLE)/TiO₂(26 MLE)/Pt(111) surface obtained after oxidizing sample (iii) in O₂ (P_{O₂}= 5x10⁻⁷ Torr) at 523 K followed by a second Ba deposition at RT and oxidation at 523 K, (v) a surface prepared by the oxidation of sample (iv) in O₂ (P_{O₂}= 5x10⁻⁷ Torr) at 973 K. (for Pt4f region see Appendix)

The first spectrum in Figure 36 was obtained after the first dosage of Ti and successive oxidation at 823 K, for 20 min in 5 x 10⁻⁷ Torr oxygen. As it can be seen from Figure 36a-i that, under these oxidative conditions, TiO_x phase is not fully oxidized and the presence of Ti³⁺ species still remains. However, additional dosage of Ti and oxidation at 973 K for 30 min under identical oxygen pressure results in a fully oxidized TiO₂ overlayer as shown in Figure 36a-ii. Moreover, an increased O 1s

intensity in Figure 36b-ii is also consistent with the growth of the oxidized TiO₂ overlayer.

Metallic Ba vapor was then introduced on the fully oxidized TiO₂/ Pt (111) system and the corresponding XPS data were presented in Figures 36(a,b,c-iii). Corresponding Ti 2p spectrum reveals that, a shoulder in the 457.1 eV region starts to form which indicates that Ti⁴⁺ phases are partially reduced to Ti³⁺ right after the Ba dosing onto the TiO₂ films. This observation indicates that Ba species partially reduce Ti⁴⁺ species into Ti³⁺ species. When the corresponding spectrum in the O 1s region is investigated, it can be seen that a new feature at the 531.6 eV BE is formed after the initial Ba dosing. It is clear that Ba and TiO₂ start to interact strongly even after the initial Ba dosing at room temperature, in order to form Ba_xTi_yO_z perovskite type species yielding an O 1s signal located at 531.6 eV.[59]

The fourth set of spectra in Figure 36 were acquired after the second dosage of Ba and oxidation at 523 K for 30 min in 5 x 10⁻⁷ Torr O₂(g). It can be seen that the additional oxidation treatment results in a re-oxidation of the remaining Ti³⁺ species to Ti⁴⁺ and yielding a single Ti 2p BE value located at 458.9 eV. In addition to this, due to the additional Ba dosage, the intensity of Ti 2p signal decreases while the intensity of the Ba 3d signal increases with a 0.3 eV shift to lower binding energies, indicating the oxidation of the BaO_x domains. Comparing the third spectrum and fourth spectrum in the O 1s core level series in Figure 36 reveals that the shoulder at the 531.6 eV becomes more visible and shifts to 532.1 eV with increasing Ba surface coverage and oxidation. This result is consistent with our previous assignment which correlates the 532.1 eV O 1s core level to Ba_xTi_yO_z species. These results are also in accord with the previous report by Widdra et al. who studied the growth of ultrathin BaTiO₃ films upon radio frequency (RF) magnetron sputter deposition on a Pt(111) substrate.[59] In this study, XPS characterization of the BaTiO₃ thin films revealed that O 1s component of the related films was observed at 532.5 eV.

For the investigation of the effect of elevated temperatures on the surface properties of BaO/ TiO₂/ Pt(111) of model catalysts, these surfaces were oxidized at 973 K in 5 x 10⁻⁷ Torr oxygen. Corresponding XPS spectra of Ti 2p, O 1s and Ba 3d core levels are represented in the topmost spectra in Figure 36. It can be seen that the intensity of the Ti 2p increases however the intensity of the Ba 3d spectrum dramatically decreases while the O 1s intensity approximately remains constant.

However, when the O1s spectrum is carefully observed, it can be realized that the feature at the 532.1 eV BE is not visible anymore and in this case there is only one XPS signal. This set of data suggests that increasing the oxidation temperature enables the interdiffusion of the BaO_x and $Ba_xTi_yO_z$ domains into the underlying TiO_2 framework. Similarly, it can be argued that the TiO_2 species segregate on the surface to obtain a Ti-rich topmost surface. The effect of the oxidation temperature on the surface properties of the $BaO/TiO_2/Pt(111)$ model catalyst was also studied with lower coverages of BaO (0.7 MLE). The dosage of Ba on thick layer of TiO_2 (26 MLE) was performed at room temperature and with the same oxidation conditions, that is waiting at 523 K for 30 min in 5×10^{-7} Torr oxygen. Moreover, in order to study the thermal deactivation, the model catalyst sample was heated at different annealing temperatures in oxygen environment. As summarized in Figure 37, Ba/Ti surface atomic ratio represents a steady decrease with increasing of the oxidation temperature.

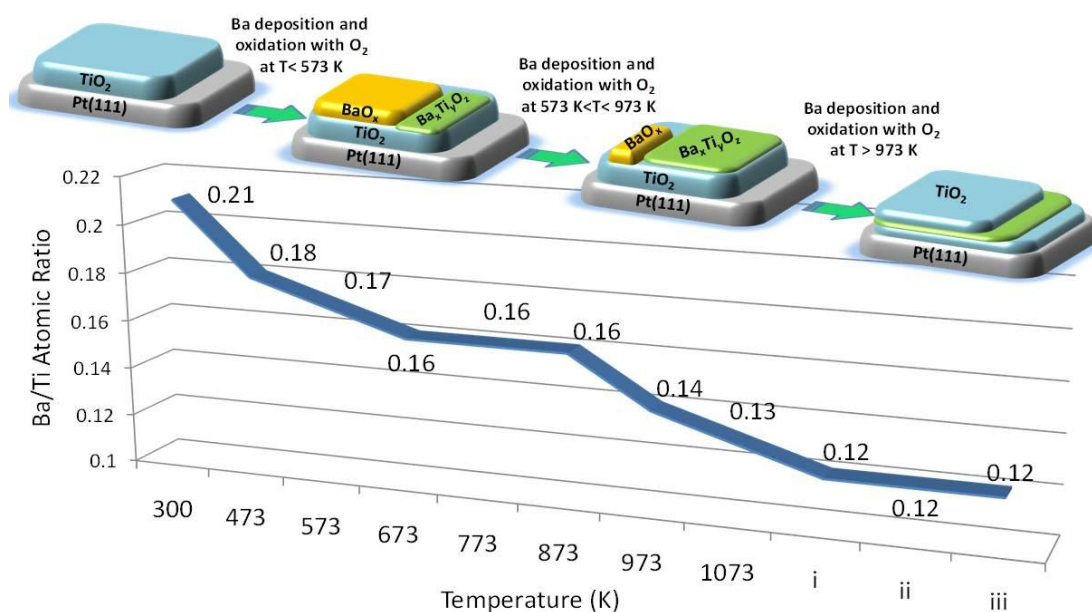


Figure 37. Ba/Ti surface atomic ratio values obtained from the XPS data for a $BaO_x(0.7 \text{ MLE})/TiO_2(26 \text{ MLE})/Pt(111)$ surface after oxidation and thermal aging steps at various temperatures (see text for details).

In these experiments, all of the oxidation steps at different temperatures were performed at the same O_2 pressure, 5×10^{-7} Torr and for an identical period of time,

i.e. 20 min. Sample i, in Figure 37, was treated with O₂ at 1073 K for 30 min. Sample ii was obtained by annealing sample i in vacuum at 1073 K, while sample iii was obtained by dosing 1 x 10⁻⁷ Torr NO₂ on sample ii at a temperature of 300 K for 30 min. As it can be seen from the Figure 37 that even the oxidation steps at relatively low temperatures (T < 573 K), cause a rather sharp decrease in the Ba/Ti surface atomic ratio, indicating that the Ba diffusion into the TiO₂ matrix has a rather small activation barrier and is likely to occur even at relatively low temperatures. Under these low-temperature oxidation conditions, the surface is probably dominated by BaO_x species with a smaller contribution from Ba_xTi_yO_z domains. Figure 37 also reveals that Ba/Ti surface atomic ratio is observed to stay rather invariant within a broad band of intermediate temperatures (i.e. 573 K-873 K). Within this temperature window, current XPS results indicate that the surface contains a larger contribution from “perovskite-type species” (Ba_xTi_yO_z). At oxidation temperatures above 873 K, a steep decline in the Ba/Ti surface atomic ratio is visible suggesting a fast and an efficient diffusion of Ba sites into the underlying TiO₂ framework. It is also apparent in Figure 43 that after extended oxidation and/or annealing step performed at 1073 K, Ba/Ti surface atomic ratio reaches a steady value which is characterized by the XPS spectra in Figure 36.

3.3.2 LEED Analysis of the Structural Changes of the BaO_x/TiO₂/Pt(111) Model Catalyst

The temperature-dependent structural changes of the BaO_x/TiO₂/Pt(111) surface were also further investigated via LEED technique represented in Figure 38.

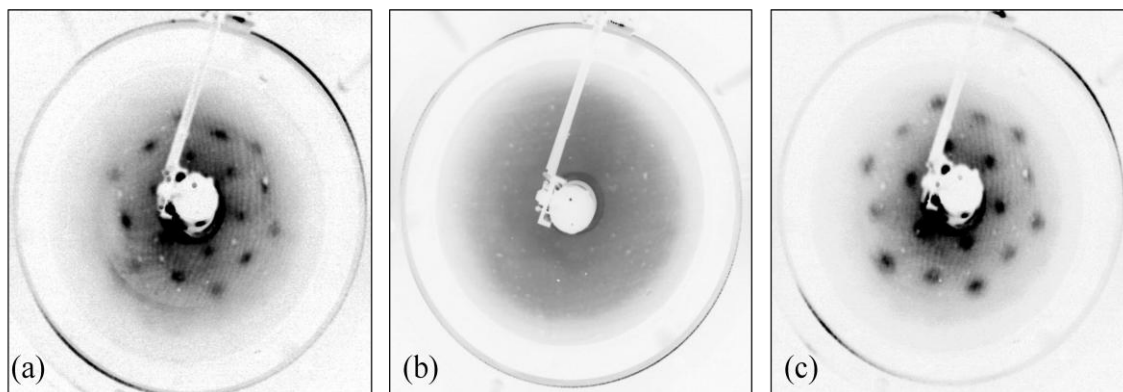


Figure 38.(a) LEED image corresponding to the (2x2) reconstruction of TiO₂ (26MLE) overlayers on Pt(111), (b) BaO_x(0.7 MLE)/TiO₂(26 MLE)/Pt(111), (c) a surface obtained by the oxidation of the sample given in (b) in O₂ (P_{O₂}= 5x10⁻⁷ Torr) at 1073 K. Electron energy values used for the acquisition of the LEED patterns in (a-c) were 85 eV, 85 eV and 105 eV, respectively.

Figure 38a shows the LEED image corresponding to a thick TiO₂, (26MLE) film grown on a clean Pt(111) substrate as described above. In spite of the large thickness of the TiO₂ overlayer, broad but clearly detectable LEED spots are visible in Figure 38a, indicating the presence of a long range order in the TiO₂ film revealing a (2x2) structure with respect to the underlying Pt(111) substrate. Previously, Marks et al. studied the rutile TiO₂(100) surface in an oxidizing environment by using transmission electron microscopy and reported that by changing annealing conditions, a centered (2x2) surface reconstruction can be obtained on this surface.[88,89] This ordered overlayer is lost when Ba (0.7 MLE) is deposited on TiO₂/Pt(111) and oxidized at 523 K in O₂ as shown in Figure 38b suggesting that BaO_x-Ba_xTi_yO_z overlayer on TiO₂/Pt(111) has an amorphous structure. Interestingly oxidation of the BaO_x-Ba_xTi_yO_z overlayer on TiO₂/Pt(111) for 20 min at 1073 K in 5 x 10⁻⁷ Torr oxygen, regenerates the exact (2x2) LEED pattern that is obtained for the clean TiO₂/Pt(111) surface as can be seen in Figure 38c. These LEED results are in very good agreement with the fact that oxidation of the BaO_x/Ba_xTi_yO_z overlayers on TiO₂/Pt(111) gives rise to the diffusion of the BaO_x/Ba_xTi_yO_z domains into the TiO₂ matrix leading to the segregation of Ti sites on the surface and the formation of a TiO₂-terminated overlayer. Segregation of Ti sites into the top surface layer of a perovskite structure was also observed for SrTiO₃(111)

[90] where a TiO(111)-(2x2) was obtained upon extended UHV annealing of the SrTiO₃(111) single crystal.

3.3.3 Chemical Reactivity of BaO_x/Ba_xTi_yO_z Overlayers to NO₂ and CO₂ on TiO₂/Pt(111) Model Catalyst

Chemical reactivity of the BaO_x/Ba_xTi_yO_z overlayers on TiO₂/Pt(111) pretreated with oxidation protocols at various BaO coverages were studied in relevance to NSR catalysis. In order to achieve this, adsorption experiments were performed by saturating the surfaces having dissimilar coverages of BaO with 180 L of NO₂ at RT ($P_{\text{NO}_2} = 1 \times 10^{-7}$ Torr for 30 min) and then monitoring the desorption profiles at elevated temperatures via TPD.

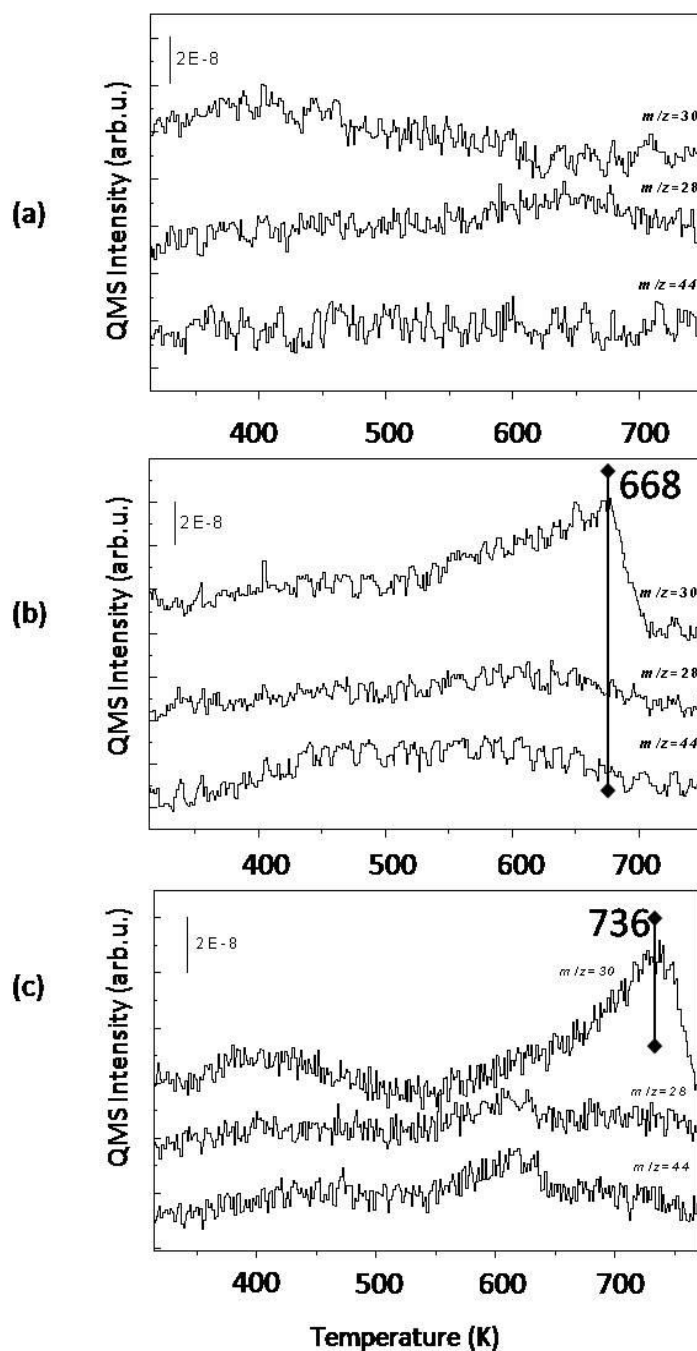


Figure 39. TPD spectra for NO ($m/z=30$), N_2/CO ($m/z=28$) and N_2O/CO_2 ($m/z=44$) desorption channels obtained (a) after exposure of $BaO(<1 \text{ MLE})/TiO_2 (26 \text{ MLE})/Pt(111)$ to 180 L NO_2 at RT (b) exposure of $BaO(1 \text{ MLE} < x < 2 \text{ MLE})/TiO_2 (26 \text{ MLE})/Pt(111)$ to 180 L NO_2 at RT (c) exposure of $BaO(>2 \text{ MLE})/TiO_2 (26 \text{ MLE})/Pt(111)$ to 180 L NO_2 at RT

Figure 39a shows the TPD profile corresponding to the 180 L of NO₂ adsorption ($P_{\text{NO}_2}=1 \times 10^{-7}$ Torr at RT for 30 min) on BaO(<1 MLE)/TiO₂(26 MLE)/Pt(111) model catalyst. Note that, as described above, the oxidation of metallic Ba took place at 523 K in oxygen environment ($P_{\text{O}_2}=5 \times 10^{-7}$ Torr). It can be seen that, at this BaO coverage, there is no significant desorption of NO species which indicates that the surface cannot efficiently store NO₂ due to the limited number of NO_x storage sites (i.e. BaO) which also partly originates from the interdiffusion between BaO and TiO₂ domains where BaO can easily penetrate into TiO₂ framework. N1s is below the detection limit of the current instrumental setup. Thus, no further insights can be gained via XPS analysis of relatively thin Ba overlayers. This is not surprising since it is well-known that instrumental detection limit of TPD technique is typically higher than XPS for many adsorbates. On the other hand, increasing the BaO (1 MLE < x < 2 MLE) coverage (Figure 39b) leads to considerable increase in NO (m/z=30) desorption signal revealing a desorption maximum at 668 K. At this higher loading of BaO, although some fraction of the BaO domains diffuse into the TiO₂ film there still remain BaO domains on the surface which can effectively store NO_x. For this particular TPD profile, broad m/z=28 desorption signal is most likely related to CO since this m/z=28 signal has a similar lineshape to the m/z=44 signal which is related to CO₂ desorption. In order to illustrate the effect of BaO coverage on the NO_x storage capacities of the BaO/TiO₂/Pt(111) model catalyst, BaO loading was further increased. Figure 39c demonstrates the NO₂ TPD profile for the BaO (>2 MLE)/TiO₂(26 MLE)/Pt(111) surface. Comparing the TPD results with previous BaO coverages (1 MLE < x < 2 MLE), it can be seen that the intensity of NO desorption increases significantly with increasing BaO_x coverage. Furthermore, the NO desorption maxima is shifted from 668 K to 736 K with higher loading of BaO indicating that the surface nitrate/nitrite stabilities are greatly enhanced which is in perfect agreement with our previous BaO_x-coverage dependent studies on the BaO_x/Pt(111) system.

In order to understand the effect of the temperature on the chemical reactivity of BaO_x (6 MLE)/ TiO₂ (26 MLE)/ Pt(111) model catalyst, TPD experiments on the same sample were performed in two different conditions. First, the BaO_x (6 MLE)/ TiO₂ (26 MLE)/ Pt(111) model catalyst surface was exposed by NO₂ at room temperature and related TPD spectra was obtained, then the BaO_x (6 MLE)/ TiO₂(26

MLE)/ Pt(111) model catalyst surface was heated at 973 K and the TPD experiments were carried out after successive NO₂ adsorption.

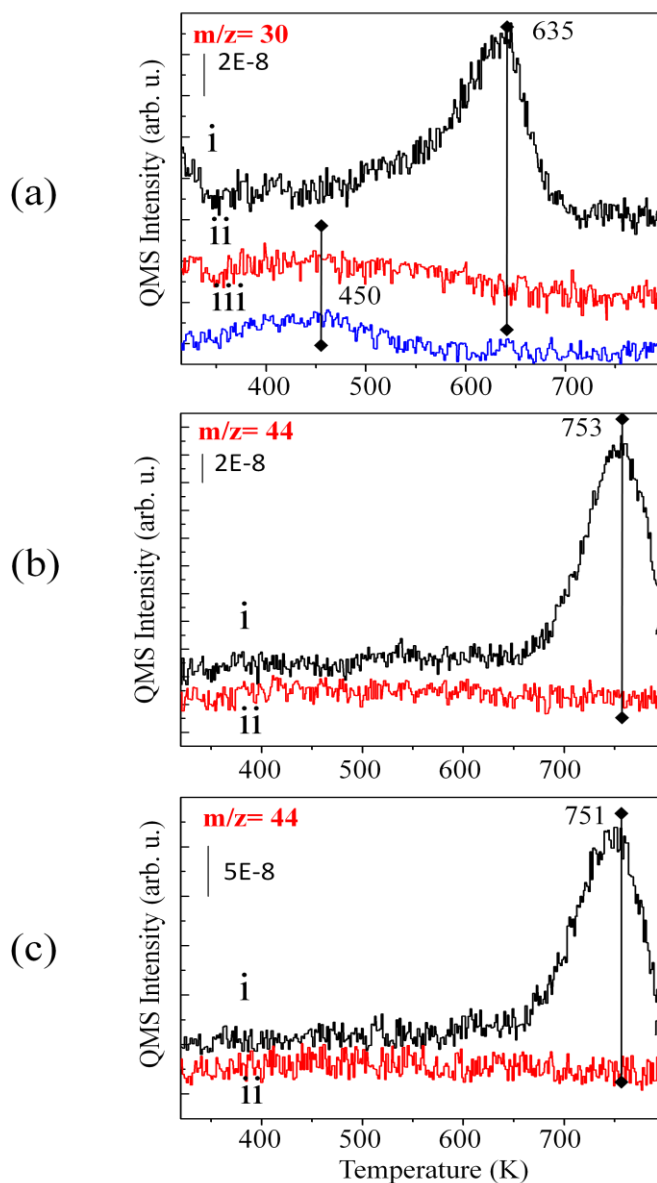


Figure 40.(a) $m/z=30$ desorption channels in the TPD profiles for NO₂ adsorption ($P_{\text{NO}_2}=1 \times 10^{-7}$, 30 min at RT) on: fresh BaO_x(6 MLE)/TiO₂(26MLE)/Pt(111) surface (spectrum *i*), BaO_x(6 MLE)/TiO₂(26MLE)/Pt(111) surface pretreated at 973 K (spectrum *ii*), fresh TiO₂(26MLE)/Pt(111) surface (spectrum *iii*). (b) $m/z=44$ desorption channels for the same TPD experiments given in part (a). (c) $m/z=44$ desorption channels in the TPD profiles for CO₂ adsorption ($P_{\text{CO}_2}=5 \times 10^{-7}$ for 5 min at RT) on: fresh BaO_x(6MLE)/TiO₂(26MLE)/Pt(111) surface (spectrum *i*), BaO_x(6MLE)/TiO₂(26MLE)/Pt(111) surface pretreated at 973 K (spectrum *ii*).

TPD spectrum given in Figure 40a-i, corresponding to $m/z=30$, clearly indicates that this surface can efficiently store NO_2 most likely in the form of nitrates resulting in a desorption maximum at 635 K that is consistent with the strongly bound ionic NO_x species [91] adsorbed on BaO_x [91-93] and $\text{Ba}_x\text{Ti}_y\text{O}_z$ domains.[94] It should be mentioned that although NO_x storage capacity of supported BaO surfaces are typically higher than that of BaTiO_3 , BaTiO_3 surfaces can also store appreciable amount of NO_2 or CO_2 in the form of nitrates/nitrites or carbonates, respectively.[95] This might be partly ascribed to the BaO termination of the $\text{BaTiO}_3(100)$ surface.[96] It is also worth mentioning that no oxygen ($m/z = 32$) evolution was detected in this TPD experiment suggesting that the oxygen atoms produced during the decomposition of nitrates/nitrites are either dissolved in the subsurface or take part in the oxidation of BaO to BaO_2 as commonly observed in the case of NO_2 desorption from BaO overlayers on $\text{Pt}(111)$ [97] or $\theta\text{-Al}_2\text{O}_3/\text{NiAl}(100)$. [46,47] TPD profile given in Figure 40a-ii, ($m/z = 30$) was obtained by saturating the surface given in Figure 40a-i, with NO_2 after the first TPD run, during which surface was heated to 973 K (in other words, spectrum *ii* corresponds to the second successive NO_2 TPD on this surface). It is evident from Figure 40a, spectrum *ii* that the NO_x uptake capacity of the surface is almost completely lost after the first TPD run which involves annealing of the sample at a higher temperature (i.e. 973 K) and the formation of a TiO_2 -terminated surface where Ba sites almost completely diffuse into the subsurface. In order to demonstrate the relatively small NO_2 adsorption energy/adsorption capacity of TiO_2 -terminated surfaces compared to that of BaO terminated surfaces, we have performed NO_2 adsorption and TPD experiments (Figure 40a, spectrum *iii*) on a TiO_2 (26 MLE)/ $\text{Pt}(111)$ surface prepared as described above. In these control experiments, a characteristically weak $m/z=30$ desorption signal was detected with a significantly lower desorption maximum at 400-450 K pointing to the fact that the saturation coverage and the adsorption strengths of adsorbed NO_x species on TiO_2 -terminated $\text{TiO}_2/\text{Pt}(111)$ surfaces at RT (Figure 40a, spectrum *ii*) are much less compared to that of $\text{BaO}_x/\text{TiO}_2/\text{Pt}(111)$ (Figure 40a, spectrum *i*) and $\text{BaO}_x/\text{Pt}(111)$ [97] surfaces.

Figure 40b presents the $m/z=44$ channel for the TPD experiments given in Figure 40a. An obvious desorption signal is visible in Figure 40b, spectrum *i* at 753 K while such a signal is absent in Figure 40b, spectrum *ii*. Note that no appreciable

amount of $m/z=14$ desorption signal was observed at c.a. 753 K, suggesting that the desorbing species does not contain N atoms and thus do not originate from N_2O . We have also performed a control experiment (data not shown) where we have carried out a “blank” TPD experiment (i.e. without any additional adsorbate introduction prior to TPD) on a freshly prepared clean $BaO_x/TiO_2/Pt(111)$ sample whose preparation was identical to that of Figure 40a, spectrum *i*. In this blank TPD experiment, we have observed an identical $m/z=44$ desorption signal at c.a. 750 K, pointing to the fact that the source of 751 K desorption feature is the CO_2 adsorption from the background of the UHV chamber. It is also seen in Figure 40b, spectrum *ii* that, the surface annealed at 973 K does not reveal any significant CO_2 desorption signal (associated with background CO_2 adsorption), consistent with the presence of a TiO_2 -terminated surface. This observation is also supported by the additional TPD experiments performed after saturating the surfaces given in Figure 40a, spectra *i* and *ii* with CO_2 at RT (Figure 40c). Figure 40c, spectrum *i* reveals a strong $m/z =44$ desorption signal at 753 K which can be readily assigned to CO_2 desorption with a desorption maximum which is in excellent agreement with Figure 40b, spectrum *i*, although the desorption signal is much stronger in the case of Figure 40c, spectrum *i*, due to the intentional saturation of this surface with excess CO_2 prior to the TPD run. It is also crucial to emphasize that the CO_2 uptake of the surface given in Figure 40c, spectrum *i* seems to be completely suppressed after annealing at 973 K (Figure 40c, spectrum *ii*). This observation is in line with the argument that just like the NO_x uptake, CO_2 uptake of a thermally-aged $BaO_x/TiO_2/Pt(111)$ surface is also seriously suppressed as a result of the formation of a Ti-enriched surface revealing a TiO_2 termination.

The schematic representation which summarize the instability and deactivation mechanism of the $BaO_x / TiO_2/ Pt(111)$ model catalyst by surface segregation and sub-surface diffusion of the mixed-oxides is given in the Figure 41.

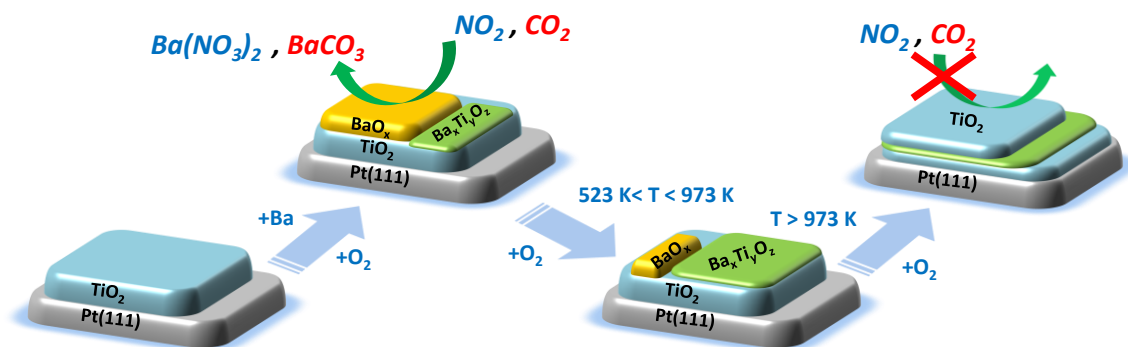


Figure 41. Schematic representation elucidating the surface segregation and sub-surface diffusion in BaO_x/TiO₂/Pt(111) model catalyst systems.

It is worth mentioning that the suggested deactivation pathway may be observed for a large number of different model catalysts prepared via different BaO_x coverages, indicating the reproducibility of the deactivation phenomena on BaO_x/TiO₂/Pt(111) model catalyst systems.

4 CONCLUSIONS

Fundamental studies of the interactions between the catalytic components of complex NSR catalysts materials are crucial for designing new materials with improved catalytic properties. Along these lines, the BaO_x layers with different coverage have been prepared on a Pt(111) substrate. Depending on the BaO_x coverage, the interaction of the BaO_x overlayers with NO₂ has been explored. The structure of the BaO_x layers was characterized by LEED. For the low BaO_x coverage (< 1 MLE) (2×2) and/or (1×2) structures were found together with metastable (2×2)R30° and/or (1×2)R30° structures which disappear after extended annealing in vacuum. BaO_x film with a coverage of 1.5 MLE grown on Pt(111) surface exhibits (110) orientation of the BaO rock salt unit cell structure. When the BaO_x layer exceeds 5 MLE, no LEED pattern was observed.

Upon 3600 L NO₂ adsorption on a thick (>10 MLE) BaO_x overlayer on Pt(111), nitrate formation was detected via XPS. These nitrate species decompose via two different stages: in the first stage only NO desorption was observed at ~650 K while in the second stage of NO + O₂ evolution was detected at ~700 K. This stepwise decomposition is explained via Ba peroxide formation during the first stage.

The influence of the BaO_x preparation method on the morphology was also elucidated. If the BaO_x thick layer is prepared by employing a post oxidation step using O₂(g), a significant amount of N₂ desorption is observed in NO₂ TPD, indicating the presence of exposed Pt(111) sites which decompose N-O linkages forming atomic N(ads) species that recombinatively desorb as N₂. If the BaO_x layer is prepared using NO₂ for Ba oxidation (i.e. without a post-oxidation step with O₂), the amount of N₂ in NO₂ TPD is negligible. Exposed Pt(111) sites can be “cured” by successive nitration and annealing cycles suggesting a reversible morphology change of the BaO_x/Pt(111) system. The BaO₂ species formed on a thick (10 MLE) BaO_x overlayer demonstrate a high thermal stability. For a relatively thin BaO_x overlayer of 2.5 MLE, BaO₂ stability decreases due to the influence of the Pt sites catalyzing the BaO₂ decomposition. With the decreasing of BaO_x overlayer coverage the nitrate/nitrite decomposition temperature is significantly decreased.

In order to investigate the thermal deactivation mechanism of TiO₂-promoted NSR systems, BaO_x films were grown on the TiO₂/Pt(111) type of model catalyst and the effect of the temperature on the surface morphology and also the surface chemistry of the BaO_x/TiO₂/Pt(111) were investigated by XPS, LEED and TPD techniques. The adsorption of metallic Ba overlayers onto TiO₂/Pt(111) caused a partial reduction of the TiO₂ domains even at room temperature. The studied model system exhibited different surface reactivity towards NO₂ and CO₂ after annealing treatments at various temperatures. Our results revealed that BaO films grown on TiO₂/Pt(111) and oxidized in O₂ at 523 K can effectively adsorb both NO₂ and CO₂. However, BaO_x phases can penetrate into the thick TiO₂ layers (26 MLE) by increasing the temperature and moreover this can further cause the formation of perovskite type structures. These thermal treatment procedures can cause a decrease in the reactivity of the surface towards NO₂ due to the domination of the Ti-species on the surface. These results are crucial findings which can give fundamental information about the properties of perovskite species that are commonly used in applied sciences (ie. BaTiO₃ as, ferroelectric wide band gap semiconductors, non-volatile ferroelectric memory and varistors, large capacity memory devices).

5 APPENDIX

5.1 Pumping Units

5.1.1 Rotary Pumps

Our UHV system has three “*Varian DS 302*” (with a pumping speed of 11.6 m³/h). These RVPs are utilized for the roughing of the main chamber turbo molecular pump, the rough pumping of the gas manifold and the differential pumping of the rotary seal on the sample manipulator stage. RVPs are oil-sealed pumps commercially available for pumping gas in the pressure range of 10⁻³-760Torr [63] Rotary vane pumps typically have 10-200 m³/h displacement and these pumps are used for rough pumping and for backing turbo molecular pumps.

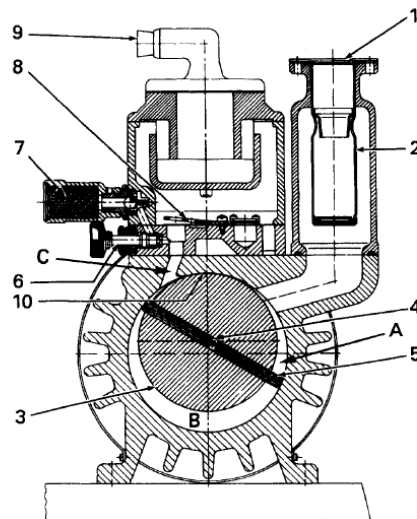


Figure 42.Sectional view of the Pfeiffer DUO-35, 35 m³/h double stage, rotary vane pump: (1) intake (2) filter (3) rotor (4) spring (5) vane (6) gas ballast valve (7) filter (8) discharge valve (9) exhaust (10) sealing surface.[63]

In RVPs, incoming gas first enters the suction chamber (A) and is compressed by the rotor (3) and a vane (5) in region (B) and excluded to the atmosphere with a discharge valve (8) and the fluid above the valve. The vanes and the surfaces between the rotor and housing are isolated with a low vapor pressure liquid, that also lubricates the pump and fill the volume above the discharge valve.

Single-stage pumps consist of one rotor and a stator block. With dual-stage RVPs, it is possible to maintain lower operating pressures compared to the single-stage pumps. This is mostly because, in single-stage pumps, oil is in contact with the outside atmosphere, from where gas is removed which partially go into the vacuum side thus restricting the pressure decrease. In the oil sealed two-stage pumps, degassed oil is supplied to the stage on the vacuum side.

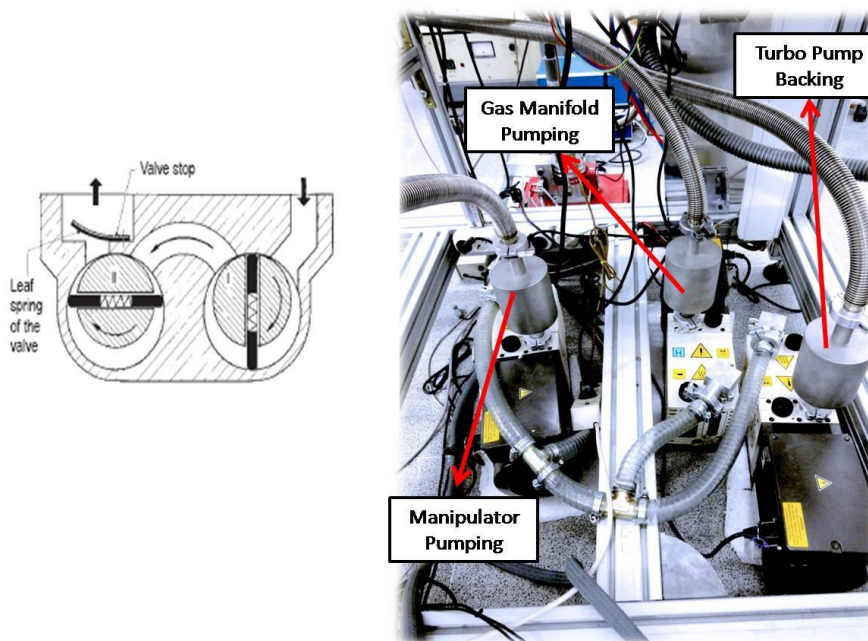


Figure 43. Schematic representation of the cross section of a dual-stage RVP (left)[63] RVP units in the UHV set-up (right).

The ultimate pressure in the second stage is lower than the first stage since the fluid circulating in the first stage is rather isolated from the second stage. The fluid in the second stage contains less gas than the fluid in the reservoir. Rotary vane pumps have an ultimate pressure of 10^{-5} - 10^{-3} Torr range. If the pump is stopped for a period of time under vacuum, oil suck back (back streaming) occurs.[64] Back streaming can be prevented by mounting a non-return valve at the pump inlet. Moreover, contamination of the system also occurs at low gas pressures (generally when the inlet pressure is below 1.0mTorr). This is a result of the condensation of both the oil vapor from the pump and its breakdown products in the system which is

at lower temperature than the pump. Therefore, it is not suggested to leave a rotary pump on a system at or near its ultimate vacuum pressure for a prolonged period without an oil trap.[64]

5.1.2 Turbo molecular Pump

Our UHV system includes two turbo molecular pumps “Varian TV 551 Navigator- Model 9698923” with a pumping speed of 550 L/s and “Pfeiffer HiCube” with a pumping speed of 70 L/s. TMPs consist of a high frequency motor driving a turbine fitted with 8 bladed stages and 4 Macerator stages. The turbine rotates in an anti-clockwise direction when viewed from the flange end. The turbine rotor is supported by a permanently lubricated high precision ceramic ball bearings installed on the fore vacuum side of the pump. The bladed molecular turbine compresses gases by momentum transfer from the rapidly rotating blades of the rotor wheels to the gas molecules. TMP requires a backing pump that can produce exhaust pressures within 10^{-3} - 10^{-2} Torr. Oil-sealed RVPs are used for this purpose. The maximum rotational speed of a turbo molecular pump is ~80 000 rpm (i.e. 1500 Hz), or blade tip velocity of 500 m/s. An ultimate pressure less than 1×10^{-10} Torr can be achieved for a baked system with a TMP .

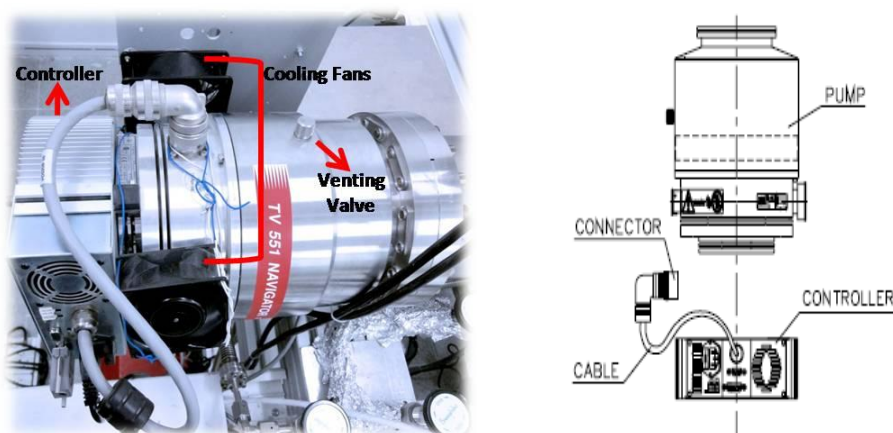


Figure 44.Varian TV 551 Navigator-Model 9698923 TMP.

There are some considerations about the applications of turbo molecular pump. For instance, if the pump is shutdown, it must be vented; otherwise it will be contaminated by oil vapors (i.e. back streaming) as a result of pressure equalization between exhaust and inlet.[64]The contamination of the vacuum system is avoided by venting the turbo pump with a dry gas to atmospheric pressure. Moreover, in order to reduce the frictional heat from the bearing areas and the motor, the bearing areas of turbo molecular pumps have to be cooled either by air cooling or water cooling. In the current UHV system, TMPs are cooled with ventilation fans.

5.1.3 Titanium Sublimation Getter Pumps

In the UHV system, TSP is mounted between TMP and the UHV chamber. In the TSP, Ti is sublimed onto a surface and this causes a highly active film functioning as chemical “getter”. On the surface of these active films, gas molecules readily form stable compounds which have extremely low vapor pressures. In order to reach a vapor pressure of about 10^{-6} Torr, Ti must be heated to 1500°C which requires a high power consumption by the TSP.[62] Ti is evaporated from a wire that is made of special alloy with a high Ti-content and heated with DC electric current. This pump has high pumping speed for the active gases. For instance, TSP is highly effective for the sorption of O_2 from the environment, in addition to H_2 , H_2O , CO and CO_2 .

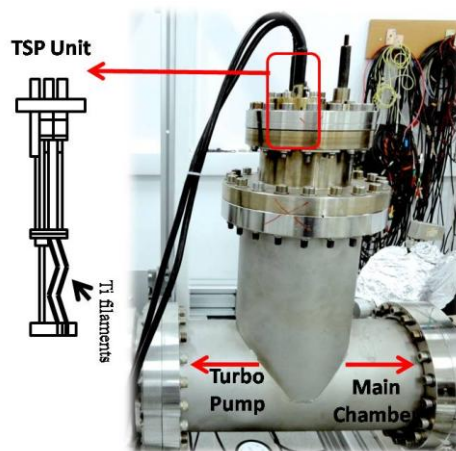


Figure 45. Titanium sublimation pump unit.

The sorption capacity is not directly proportional with the Ti film thickness, since the film tends to be more compact and its internal layers become less attainable to the gas. This means that to better usage of the Ti active films, one should evaporate less Ti, but more frequently.

5.2 UHV Pressure Gauges

5.2.1 Ionization Gauge

Ionization gauges are used to for the measurement of the lowest attainable pressures around 2×10^{-11} Torr.[64] Ion gauge operation is based on electron impact ionization. The pressure is proportional to the ionized molecular current while temperatures and all other parameters are held constant. Such gauges refer to measuring systems consisting of three electrodes (cathode, anode and ion collector) where the cathode is a hot cathode. Tungsten is frequently used for the material of cathode however, now, ThO₂-coated iridium is usually used in order to reduce the electron output work and make them more resistant to oxygen.[65] Electrons are generated in the hot cathode and accelerated in the electric field. If a sufficient energy is received, these electrons ionize the gas molecules in which the electrode system is located. The positive gas ions formed are then transferred to the ion collector, which is negative with respect to the cathode, and lose their charge there. For this reason, ion current is related with the gas density, not the pressure itself, as a result the ion gauge is not a true pressure measuring instrument, but it is a particle-density gauge. Bayard-Alpert type of ion gauge, which is used in our UHV system, is the most popular design for the measurement of the high vacuum pressures.[63] In this design, the large area collector was replaced with a fine wire in the center of the grid.

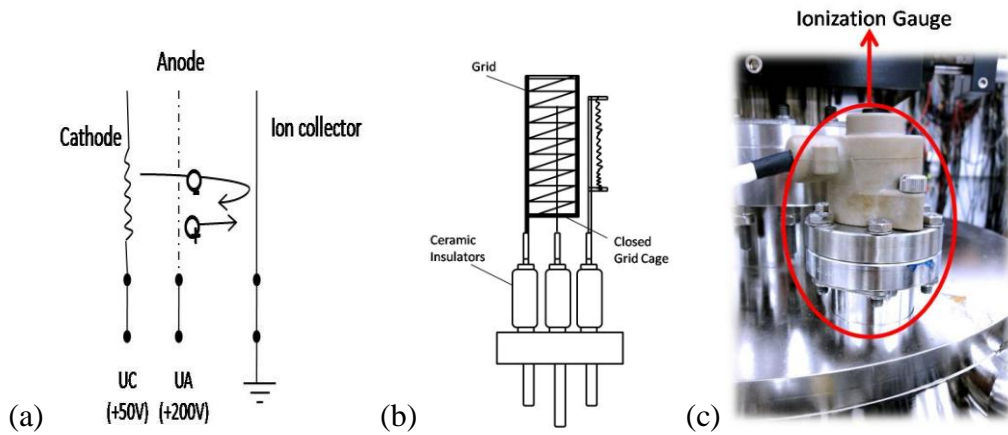


Figure 46. (a) Ionization gauge mechanism (adapted from ref. [49]) (b) Schematic representation of an Bayard-Alpert type ionization gauge (adapted from ref. [63]) (c) Ionization gauge utilized in the UHV set-up.

The pressure measurement can be affected by two factors at low pressures: the X-ray effect and ion desorption effect. These effects can result in the loss of proportionality between the pressure and the ion current. The X-ray effect is caused due to the release of X-ray photons from the cathode (filament) surface impinging on the anode (collector) and result in photoelectron emission resulting in an effect that is identical to positive gas ions do. This photocurrent generates a baseline virtual pressure value which determines lowest detection limit of the ion gauge. This is called the X-ray limit.[65] In the Bayard-Alpert type of design, this X-ray effect is suppressed and this is achieved by the hot cathode is placed outside the anode and the ion collector is a thin wire in the axis of the electrode system. The X-ray effect is reduced by two to three orders of magnitude, since the surface area of the ion collector is greatly reduced. Ion gauge grids can be out gassed by either resistive heating or electron beam bombardment at high grid voltage (500 V). However, the pressure must be on a suitably low value ($\sim 10^{-9}$ Torr), before out gassing. The time for the out gassing is typically 15-20 min.[63]

5.2.3 Thermal Conductivity Gauge (Thermocouple Gauge)

The TC gauge measures pressure as a function of heat flow. A constant electric current is sent to a heated wire, and a tiny Chromel-Alumel (K-type) thermocouple is spot welded to its midpoint. When the pressure increases, heat flows to the walls and the temperature of the wire decreases. A low-resistance dc microammeter is connected to the TC and its scale is calibrated in pressure units.

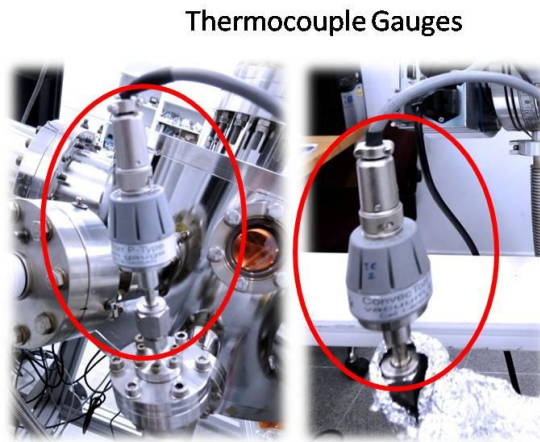


Figure 47. Thermocouple gauges in the UHV experimental set-up.

TC gauges with constant resistance have a pressure measuring range from 10^{-4} to 1013 Torr; however, the most sensitive range is between 10^{-3} and 1 Torr. Their usages are suitable for protective functions, as in the determination time when hot-cathode ionization gauge is turned on. Their range makes them the usual choice for measuring backing and roughing pressures as in the case of our UHV system. Their usage in contaminating environment is not suitable because of their sensitivity to various gases.

5.2.4 Capacitance Manometer

Capacitance manometer is a diaphragm gauge where the deflection of the diaphragm is electrically measured as “strain” or as a change in capacitance. It uses the

fact that the electrical capacitance of a parallel plate capacitor is a function of the separation of the electrodes.

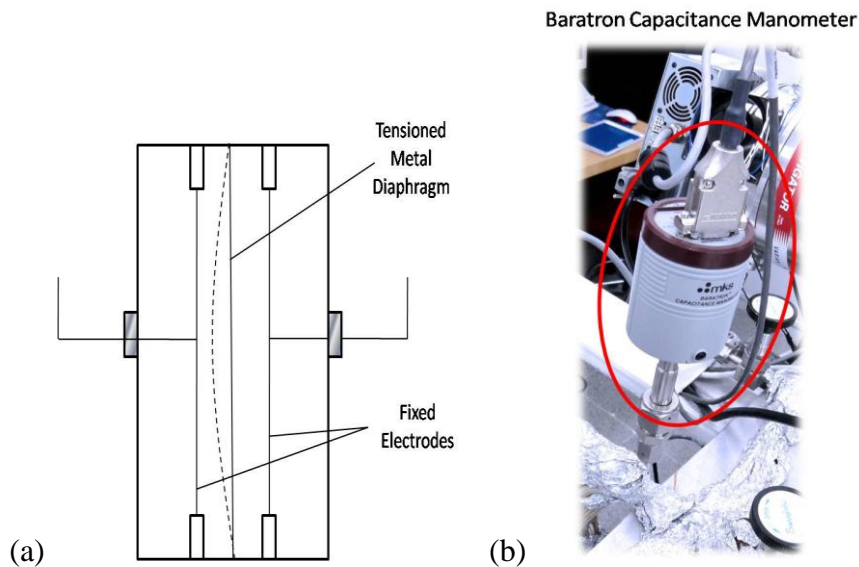


Figure 48.(a) Basic diagram of capacitance diaphragm gauges (adapted from ref. [63]) (b) Baratron capacitance manometer in the UHV chamber.

Capacitance manometers consist of two components, a transducer and an electronic sensor unit that converts the membrane position to a signal linearly proportional to the pressure.[63]Capacitance manometers can operate over a large dynamic range, however, after 1000 Torr, the overall system accuracy collapses. Baratron® capacitance manometers measures true pressure (defined as force/unit area) which means that the measurement is insensitive of gas being measured. Other gauges, such as TC, Pirani and ion gauges do not measure the true total pressure since their readings are gas-type sensitive(i.e. calibrated only for a particular gas).

5.3 XPS Figures

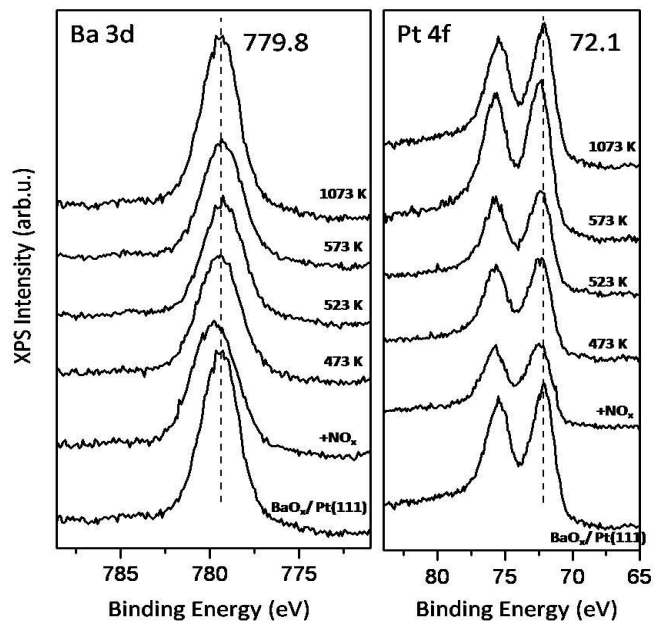


Figure 49. XPS core level spectra, Ba3d and Pt4f for a thick BaO_x(10 MLE) /Pt(111) exposed to 3600 L NO₂ at 323 K and subsequently annealed to the indicated temperatures in vacuum.

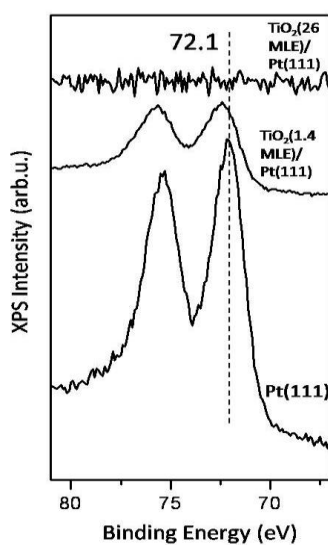


Figure 50. XPS core level spectra corresponding to Pt4f during the growth of TiO₂ (26 MLE) overlayers on Pt(111) substrate

6 REFERENCES

- [1] Bera, P.; Hegde, M.S. *Journal of the Indian of Science* **2010**, *90*, 2.
- [2] Epling, W.S.; Campbell, L.E.; Yezerets, A.; Currier, N.W.; Parks, J.E. *Catal. Rev.* **2004**, *46*, 163.
- [3] Seinfeld, J.H.; *Atmospheric Chemistry and Physics of Air Pollution*, Wiley, New York, **1986**, 738.
- [4] <http://www.dieselnet.com/standards/eu/ld.php>
- [5] Roy, S.; Baiker, A. *Chem. Rev.* **2009**, *109*, 4054.
- [6] Skalska, K.; Miller, J.S.; Ledakowicz, S. *Sci. Total. Environ.* **2010**, *408*, 3976.
- [7] Matsumoto, S. *Catal. Today* **1996**, *29*, 43.
- [8] Alkemade, U.G.; Schumann, B. *Solid State Ionics* **2006**, *177*, 2291.
- [9] Forzatti, P.; Castoldi, L.; Nova, I.; Lietti, L.; Tronconi, E. *Catal. Today* **2006**, *117*, 316.
- [10] Al-Harbi, M.; Epling, W.S. *Catal. Lett.* **2009**, *130*, 121.
- [11] Olsson, L.; Persson, H.; Fridell, E.; Skoglundh, M.; Andersson, B. *J. Phys. Chem. B* **2001**, *105*, 6895.
- [12] Crocol, M.; Kureti, S.; Weisweiler, W. *J. Catal.* **2005**, *229*, 480.
- [13] Nova, I.; Castoldi, L.; Lietti, L.; Tronconi, E.; Forzatti, P.; Prinetto, F.; Ghiotti, G. *J. Catal.* **2004**, *222*, 377.
- [14] Olsson, L.; Westerberg, B.; Persson, H.; Fridell, E.; Skoglundh, M.; Andersson, B. *J. Phys. Chem. B* **1999**, *103*, 10433
- [15] Epling, W.S.; Parks, J.E.; Campbell, G.C.; Yezerets, A.; Currier, N.W.; Campbell, L.E. *Catal. Today* **2004**, *96*, 21
- [16] Broqvist, P.; Grönbeck, H.; Fridell, E.; Panas, I. *Catal. Today* **2004**, *96*, 71.
- [17] Cant, N.W.; Patterson, M.J. *Catal. Today* **2002**, *73*, 271.
- [18] Lietti, L.; Forzatti, P.; Nova, I.; Tronconi, E. *J. Catal.* **2001**, *204*, 175.
- [19] Roy, S.; Hegde, M.S.; Madras, G. *Appl. Energy* **2009**, *86*, 2283.
- [20] Gunter, P.L.J.; Niemantsverdriet, J.W.; Ribeiro, F.H.; Somorjai, G.A. *Catal. Rev.* **1997**, *39*, 77.
- [21] Libuda, J.; Freund, H.-J. *Surf. Sci. Rep.* **2005**, *57*, 157.
- [22] Clair, T.P.S.; Goodman, D.W. *Top. Catal.* **2000**, *13*, 5

- [23] Freund, H.-J.; Kuhlenbeck, H.; Libuda, J.; Rupprechter, G.; Baumer, M.; Hamann, H. *Top. Catal.* **2000**, *15*, 201.
- [24] Bowker, M. *Surf. Sci.* **2009**, *603*, 2359.
- [25] Freund, H.-J. *Surf. Sci.* **2007**, *601*, 1438.
- [26] Ertl, G. *Angew. Chem. Int. Ed.* **1990**, *29*, 1219.
- [27] Libuda, J.; Schauermaun, S.; Laurin, M.; Schalow, T.; Freund, H.-J. *Monatshefte für Chemie* **2005**, *136*, 59.
- [28] Henry, C.R. *Surf. Sci. Rep.* **1998**, *31*, 231.
- [29] Conner, W.C.; Falconer, J.L. *Chem. Rev.* **1995**, *95*, 759.
- [30] Meyer, R.; Baumer, M.; Shaikhutdinov, S.K.; Freund, H.-J. *Surf. Sci. Lett.* **2003**, *546*, L813.
- [31] Freund, H.-J.; Pacchioni, G. *Chem. Soc. Rev.* **2008**, *37*, 2224.
- [32] Vurens, G.H.; Salmeron, M.; Somorjai, G.A. *Surf. Sci.* **1988**, *201*, 129.
- [33] Xu, X.; Goodman, D.W. *Appl. Phys. Lett.* **1992**, *61*, 774.
- [34] Wu, M.C.; Corneille, J.S.; Estrada, C.A.; He, J.-W.; Goodman, D.W. *Chem. Phys. Lett.* **1991**, *182*, 472.
- [35] Kuhlenbeck, H.; Odörfer, G.; Jaeger, R.; Illing, G.; Menges, M.; Mull, T.; Freund, H.-J.; Pöhlchen, M.; Staemmler, V.; Witzel, S.; Scharfschwerdt, C.; Wenneman, K.; Liedtke, T.; Neumann, M. *Phys. Rev. B* **1991**, *43*, 1969.
- [36] Wichtendahl, R.; Rodriguez-Rodrigo, M.; Hartel, U.; Kuhlenbeck, H.; Freund, H.-J. *Surf. Sci.* **1999**, *423*, 90.
- [37] Al-Abadleh, H.A.; Grassian, V.H. *Surf. Sci. Rep.* **2003**, *52*, 63.
- [38] Garin, F. *Appl. Catal. A* **2001**, *222*, 183.
- [39] Hess, C.; Lundsford, J.H. *J. Phys. Chem. B* **2003**, *107*, 1982.
- [40] Stone, P.; Ishii, M.; Bowker, M. *Surf. Sci.* **2003**, *537*, 179.
- [41] Bowker, M.; Stone, P.; Smith, R.; Fourre, E.; Ishii, M.; de Leeuw, N.H. *Surf. Sci.* **2006**, *600*, 1973.
- [42] Tsami, A.; Grillo, F.; Bowker, M.; Nix, R.M. *Surf. Sci.* **2006**, *600*, 3403.
- [43] Schmitz, P.J.; Baird, R.J. *J. Phys. Chem. B* **2002**, *106*, 4172.
- [44] Staudt, T.; Desikusumastuti, A.; Happel, M.; Vesselli, E.; Baraldi, A.; Gardonio, S.; Lizzit, S.; Rohr, F.; Libuda, J. *J. Phys. Chem. C* **2008**, *112*, 9835.
- [45] Desikusumastuti, A.; Happel, M.; dumbuya, K.; Staudt, T.; Laurin, M.; Gottfried, J.M.; Steinrück, H.P.; Libuda, J. *J. Phys. Chem. C* **2008**, *112*, 6477.

- [46] Ozensoy, E.; Peden, C.H.F.; Szanyi, J. *J. Phys. Chem. B* **2006**, *110*, 17009.
- [47] Ozensoy, E.; Peden, C.H.F.; Szanyi, J. *J. Phys. Chem. B* **2006**, *110*, 17001.
- [48] Yi, C.W.; Kwak, J.H.; Szanyi, J. *J. Phys. Chem. C* **2007**, *111*, 15299.
- [49] Yi, C.W.; Szanyi, J. *J. Phys. Chem. C* **2009**, *113*, 716.
- [50] Yi, C.W.; Szanyi, J. *J. Phys. Chem. C* **2009**, *113*, 2134.
- [51] Hirata, H.; Hachisuka, I.; Ikeda, Y.; Tsuji, S.; Matsumoto, S. *Top. Catal.* **2001**, *16-17*, 145.
- [52] Rodriguez, J.A.; Jirsak, T.; Liu, G.; Hrbek, J.; Dvorak, J.; Maiti, A. *J. Amer. Chem. Soc.* **2001**, *123*, 9597.
- [53] Henderson, M.A.; Szanyi, J.; Peden, C.H.F. *Catal. Today* **2003**, *85*, 251.
- [54] Sedona, F.; Rizzi, G.A.; Agnoli, S.; Llabres i Xamena, F.X.; Papageorgiou, A.; Ostermann, D.; Sambri, M.; Finetti, P.; Schierbaum, K.; Granozzi, G. *J. Phys. Chem. B* **2005**, *109*, 24411.
- [55] Andonova, S.M.; Şentürk, G.S.; Kayhan, E.; Ozensoy, E. *J. Phys. Chem. C* **2009**, *113*, 11014.
- [56] Hagendorf, C.; Schindler, K.M.; Doege, T.; Neddermayer, H. *Appl. Surf. Sci.* **1999**, *142*, 106.
- [57] Hagendorf, C.; Schindler, K.M.; Doege, T.; Neddermayer, H. *Surf. Sci.* **1998**, *436*, 121.
- [58] Hagendorf, C.; Schindler, K.M.; Doege, T.; Neddermayer, H. *Surf. Sci.* **1998**, *402*, 581.
- [59] Förster, S.; Widdra, W. *Surf. Sci.* **2010**, *604*, 2163.
- [60] Broqvist, P.; Grönbeck, H. *Surf. Sci.* **2006**, *600*, L214.
- [61] Reichel, W.; Hayek, K. *Studies in Surf. Sci. Catal.* **2000**, *130*, 719.
- [62] Woodruff, D.P.; Delchar, T.A. *Modern Techniques of Surface Science*, 2nd Edition, Cambridge University Press, Cambridge, **1994**.
- [63] O'Hanlon, J.F. *A User's Guide to Vacuum Technology*, 3rd Edition, Wiley, New Jersey, **2003**.
- [64] Lafferty, J.M. *Foundations of Vacuum Science and Technology*, Wiley, New York, **1998**.
- [65] Umrath, Dr.W. *Fundamentals of Vacuum Technology*, **1998**.
- [66] Behrisch, R.; Eckstein, W. *Top. Appl. Phys.* **2007**, *110*, 1.

- [67] Watts, J.F.; Wolstenholme, J. *An Introduction to Surface Analysis by XPS and AES*, Wiley, West Sussex, **2003**.
- [68] Niemantsverdriet, J.W. *Spectroscopy in Catalysis*, 3rd Edition, Wiley, Mörlenbach, **2007**.
- [69] Wagner, C.D.; Riggs, W.M.; Davis, L.E.; Moulder, J.F.; Muilenberg, G.E. *Handbook of X-Ray Photoelectron Spectroscopy*, Perkin-Elmer Corp., Minnesota, **1978**.
- [70] Tanuma, S.; Powell, C.J.; Penn, D.R. *Surf. Interface. Anal.* **1994**, *21*, 165.
- [71] Jona, F.; Strozier, J.A.; Yang, W.S. *Rep. Prog. Phys.* **1982**, *45*, 527.
- [72] Atkins, P.; de Paula, J. *Physical Chemistry*, 8th Edition, Oxford University Press, Oxford, **2006**.
- [73] Van Hove, M.A.; Weinberg, W.H.; Chan, C.M. *Low Energy Electron Diffraction*, Springer Verlag, Berlin, **1986**.
- [74] Clarke, L.J. *Surface Crystallography*, Wiley, New York, **1985**.
- [75] Riviere, J.C. *Surface Analytical Techniques*, Oxford Science Publications, Oxfordshire, **1990**.
- [76] Broqvist, P.; Gronbeck, H.; Panas, I. *Surf. Sci.* **2004**, *554*, 262.
- [77] Bowker, M.; Cristofolini, M.; Hall, M.; Fourre, E.; Grillo, F.; McCormack, E.; Stone, P. Ishii, M. *Top. Cat.* **2007**, *42–43*, 341
- [78] Szanyi, J.; Kwak, J. H.; Kim, D. H.; Burton, S. D.; Peden, C. H. F. *J. Phys. Chem. B* **2005**, *109*, 27.
- [79] Altman, E.I; Gorte, R.J. *J. Phys. Chem.* **1989**, *93*, 1993.
- [80] Gland, J.L; Sexton, B.A *Surf. Sci.* **1980**, *94*, 355.
- [81] Gorte, R.J.; Schmidt, L.D.; Gland, J.L. *Surf. Sci.* **1981**, *109*, 367.
- [82] Mudiyansele, K.; Yi, C.-W.; Szanyi, J. *Langmuir* **2009**, *25*, 10820
- [83] Verhoeven, J.A.Th.; Doveren, H. *Surf. Sci.* **1982**, *123*, 369.
- [84] Gland, J.L. *Surf. Sci.* **1978**, *71*, 327
- [85] Oku, M.; Wagatsuma, K.; Kohiki, S. *Phys. Chem. Chem. Phys.* **1999**, *1*, 5327.
- [86] Barcaro, G.; Sedona, F.; Fortunelli, A.; Granozzi, G. *J. Phys. Chem. C* **2007**, *111*, 6095.
- [87] Finetti, P.; Sedona, F.; Rizzi, G.A.; Mick, U.; Sutara, F.; Svec, M.; Matolin, V.; Schierbaum, K.; Granozzi, G. *J. Phys. Chem. C* **2007**, *111*, 869.

- [88] Warschkow, O.; Wang, Y.; Subramanian, A.; Asta, M.; Marks, L. D. *Phys. Rev. Lett.* **2008**, *100*, 086102.
- [89] Wang, Y.; Warschkow, O.; Marks, L. D. *Surf. Sci.* **2007**, *601*, 63.
- [90] Russell, B.C.; Castell, M.R. *J. Phys. Chem. C* **2008**, *112*, 6538.
- [91] Ozensoy, E.; Szanyi, J.; Peden, C. H. F. *J. Phys. Chem. B* **2005**, *109*, 15977.
- [92] Ozensoy, E.; Peden, C. H. F.; Szanyi, J. *J. Catal.* **2006**, *243*, 149.
- [93] Ozensoy, E.; Szanyi, J.; Peden, C. H. F. *J. Phys. Chem. B* **2005**, *109*, 3431.
- [94] Hodjati, S.; Vaezzadeh, K.; Petit, C.; Pitchon, V.; Kiennemann, A. *Appl. Catal., B*, **2000**, *26*, 5.
- [95] Hodjati, S.; Vaezzadeh, K.; Petit, C.; Pitchon, V.; Kiennemann, A. *Appl. Catal., B*, **2000**, *26*, 5.
- [96] Berlich, A.; Strauss, H.; Langheinrich, C.; Chassé, A.; Morgner, H. *Surf. Sci.* **2011**, *605*, 158.
- [97] Vovk, E.; Emmez, E.; Bukhtiyarov, V.I.; Ozensoy, E. manuscript in preparation.